Spring 2016

Variable stress orientations in the offshore Nile Delta: The role of salt as a mechanical detachment horizon

Weicheng Zhang

Department:

VARIABLE STRESS ORIENTATIONS IN THE OFFSHORE NILE DELTA: THE ROLE OF SALT AS A MECHANICAL DETACHMENT HORIZON

by

WEICHENG ZHANG

A THESIS

Presented to the Faculty of the Graduate School of the

MISSOURI UNVERSITY OF SCIENCE AND TECHNOLOGY

In Partial Fulfillment of the Requirements for the Degree

MASTER OF SCIENCE IN PETROLEUM ENGINEERING

2016

Approved by:

Andreas Eckert, Advisor

Runar Nygaard

John P. Hogan

ABSTRACT

The offshore Nile Delta is characterized by variations of the maximum horizontal stress orientation in subsalt and supra-salt sequences. Margin-parallel S_H, typical for tertiary deltas, is observed for regions that are below or do not contain evaporites. In sequences underlain by evaporates pre-dominantly margin-normal S_H is observed. This observation yielded the first conclusive in situ evidence that salt acts as a mechanical detachment layer. In this study, 3D finite element analysis (FEA) is used to simulate the total stress distribution in the offshore Nile Delta featuring evaporate sequences. Several parameters such as different salt sequence geometries, friction coefficient on faults, and salt viscosity are considered. The numerical modeling results are used to evaluate if possible basal drag forces or mechanical property contrast effect induced by gravitational gliding result in varying stress orientations and if the observed stress orientations in the Nile Delta can be explained and correlated by the numerical modeling results. Implication of the modeling results for hydrocarbon production will be analyzed and discussed.

ACKNOWLEDGEMENTS

I would like to express my gratitude to my advisor, Dr. Andreas Eckert, for accepting me into the Geomechanical Modeling Group. During the past few years, he has always been both a supportive mentor for my research and an encouraging friend for my daily life. Without his advice and help, I would have never been able to overcome cultural and language barriers so easily. “Think critically” is the first advice he gave to me, and it has since then become the motto I set for my life.

I would like to thank my graduate committee members Dr. Hogan and Dr. Nygaard for their instruction and guidance. Their valuable and enlightening comments are of vital importance for the completion of my research.

I would also like to thank my friend, Xiaolong Liu, who has been like an older brother to me during my life here. My thanks also go to my friends in the Geomechanical Modeling Group: Deepak Gokaraju, Nevan Himmelberg, Eli Steinbeck, and Davi Damasceno. Their constructive advice and friendly work environment made me productive.

My girlfriend, Huining Zhang deserves a special thank you for her love, encouragement, support, and understanding.

Last but not least, I would also like to thank my father, Xinhua Zhang. His hard work in Africa and the Middle East for the past 15 years has provided me with both enough financial support and strong willingness to study aboard. I would also like to thank my mother, Gaiyu Zheng. Her career as a geologist gave me the initial cognition of geology and the abundant enthusiasm for my research.

TABLE OF CONTENTS

Page

LIST OF ILLUSTRATIONS

Figure Page

LIST OF TABLES

NOMENCLATURE

Symbol	Description
σ_1	Maximum Principal Stress
σ_2	Intermediate Principal Stress
σ_3	Minimum Principal Stress
S_H	Maximum Horizontal Stress
S_h	Minimum Horizontal Stress
S_V	Vertical Stress
σ	Stress
ε	Strain
C_{ijkl}	Stiffness Tensor
E	Young's Modulus
ν	Possion's Ratio
$\dot{\varepsilon}$	Strain Rate
υ	Viscosity
ρ	Density
μ	Friction Coefficient
$\vec{F}$	Force Vector
$\vec{T}$	Traction Vector
σ_{ij}	Stress Tensior
σ_n	Normal Stress
σ_v	von Mises Stress

1. INTRODUCTION

1.1. OVERVIEW

Salt evaporites grow pervasively in deltaic regions where hydrocarbon reserves are discovered or have the potential to be discovered. Both evaporites and structures associated with evaporites have been identified in a number of deltaic regions such as offshore Brazil, the Gulf of Mexico, the North Sea and the Nile Delta (Figure 1.1.). The presence of salt evaporites drastically increases the difficulty of offshore hydrocarbon exploration and exploitation that require drilling through salt layers (Perez et al., 2005). The Nile Delta is a typical tertiary delta featuring the largest clastic accumulation in the Mediterranean Sea. Abundant organic substances brought by the Nile River, combined with relatively weak tectonic movement, make the Nile Delta a potential hydrocarbon accumulating region. The offshore Nile delta is characterized by the Messinian evaporite sequence, which mainly underlies the Pliocene sedimentary cover (Warren, 2004). The Messinian evaporite sequence has recently been interpreted as a mechanical detachment layer (Tingay et al., 2011; 2012) decoupling the stress regimes in the overlaying (termed supra-salt) and underlying (termed subsalt) sequences. Stress orientation data from 44 wells in three different hydrocarbon fields in the offshore Nile Delta presented by Tingay et al. (2011) show sharply contrasting stress orientations (~90° variations) in supra- vs. subsalt layers. These data sets provide the first major evidence that evaporite sequences can act as mechanical detachment horizons (Tingay et al., 2011). Tingay et al. (2011; 2012) postulate two hypotheses in order to explain the origin of the observed stress variations. In the first hypothesis the observed margin normal stress orientations in the supra-salt layers could be the result of down slope gravity gliding of salt bodies inducing basal drag forces in the sediments. As stated by Tingay et al. (2011; 2012) it remains unclear whether such a mechanism is plausible and whether it can explain the observed stress orientations. In the second hypothesis the scattered stress orientations could be explained by mechanical property contrasts imposed by the Messinian evaporites. While both hypotheses present plausible explanations and both favorable and opposing arguments are discussed by Tingay et al. (2011, 2012), quantitative evidence to support either possibility is not presented.

The Finite-element method has unique advantages in simulating and analyzing large scale geological structures (Schultz-Ela and Jackson, 1993; Buchmann and Connolly, 2007; Nikolinakou et al., 2011; Tingay et al., 2014). This study utilizes the commercial finite-element software package Abaqus^{TM} (Hibbitt et al., 2001) to simulate the gravitational gliding of supra-salt faults, in order to evaluate the influence of salt bodies on fault movement and stress distribution. In the finite element models, different salt body geometries and parameters are tested and general mechanisms are summarized to explain the abnormal stress field above the salt-bearing regions.

Figure1.1. Global distribution of salt formations in deep water (Figure. from Perez .et al, 2008)

1.2. LITERATURE REVIEW

1.2.1 Geological Summary of the Nile Delta. The Nile Delta system is the largest clastic wedge in the Mediterranean Sea region. It was created by an influx of clastic sediments from the Nile River since the late Miocene period (Badawy et al., 2004). Due to the active tectonic activity since the Cenozoic period, the Nile Delta is composed of two separate clastic delta systems: an inert Jurassic-Miocene delta system located in the lower part and an active Pliocene-Holocene delta system, which is still growing nowadays, deposited in the upper part. An unconformity comprised of Messinian evaporites isolates the two systems (Warren, 2004; Loncke et al., 2006; Tingay et al., 2011). Clauzon et al. (1996) notes that the evaporite-depositing episode was produced by

a weak global sea level fall during the Messinian period (5.75-5.60 Ma). Numerous tectonically induced marginal basins around the Mediterranean Sea have been isolated, and evaporites have been formed in these basins, including Spain, Libya, Morocco, Sicily, Cyprus and the Northeast Nile Delta (Bosworth, 2006).

A structural analysis based on 3D seismic data indicates large, continuous evaporite layers acting as detachment zones affect the structural evolution of sequences above it significantly (Marten et al., 2004). Sequences above Messinian evaporites feature both typical deltaic structures (e.g. listric-growth faults and rotational block faults), and salt-associated structures, such as normal and strike-slip faults, collapsed depocenters, and polygonal minibasins (Loncke et al., 2006). A series of listric, NNE-SSW trending normal faults divide the overburden sequences above evaporites into blocks ranging from 10-50 km in length (Figure 1.2.). Channel systems formed within these blocks were either disrupted or guided by the faulting movement, suggesting recent faulting activity (Loncke et al., 2002). The NW-SE bounding listric faults are, in general, gradually losing rotational tendencies in the northwest edge of the delta province and are replaced progressively by en echelon grabens (Marten et al., 2004) (Figure 1.2.).

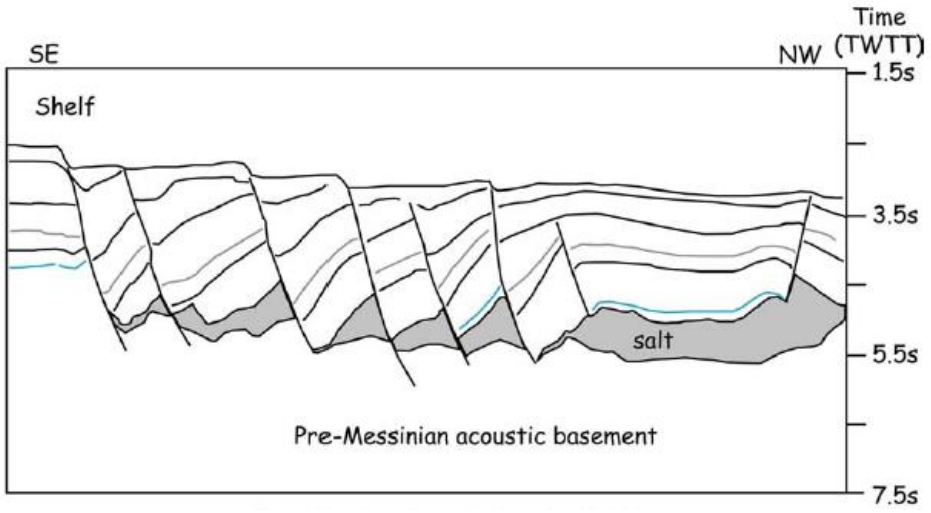

Figure 1.2. The listric faulting pattern interrupted by en echelon grabens (Figure from Aal et al., 2000)

In contrast, structures discovered in the Jurassic-Miocene delta system, below the evaporites, are much simpler, exerting little influence over supra-evaporites sequences. Few listric normal faults in the delta shelf and few thrust faults in the toe exist (Loncke et al., 2009). The strongly compacted environment of the lower delta system restricts the moving potential of faults, creating a relatively stable basement. Although it is unclear how basement deformation is transmitted through the salt layer, it is believed that the detachment horizon, mainly the Messinian evaporites, may weaken the influence of the basement on the stress field in the upper part (Marten et al., 2004).

The northeast portion of the Mediterranean Sea is located at a passive margin characterized by many tectonic features. These features include the following (Figure 1.3.):

- the Suez Rift in the southeast, which recently became inert (Mascle et al., 2003),
- the Levant/Dead Sea and the East Anatolian Fault zones in the east, which are formed by the motion of the Arabian plate with respect to Africa,
- along the Cyprus and eastern Hellenic arcs, the collision/subduction of Africa beneath Europe, and the active Aegean-Anatolian microplate in the north and northwest (Huguen, 2001)
- the Egyptian margin, a passive margin formed during the Mesozoic age, that was partially reactivated by the Suez-Red Sea Rift System during the Miocene (Mascle et al., 2003).

Aal et al. (2000), Martin, et al. (2004), and Bosworth et al. (2008) suggest that the Nile Delta region is located within the rigid North African Plate, which tends to move northwards. As a result, the influence of adjacent tectonic plates on the Nile Delta region is small (Tingay et al., 2012). Badaway et al. (2014), based on the GPS velocity field map of north Egypt, suggested that the African plate, including the Nile Delta region, is moving northward with respect to Eurasian plate at an average rate of 5.15±1.1 mm/year. In summary, multiple tectonic activities, although occurring very close, only have a minor influence on the stress regime in the northeast part of the Nile Delta.

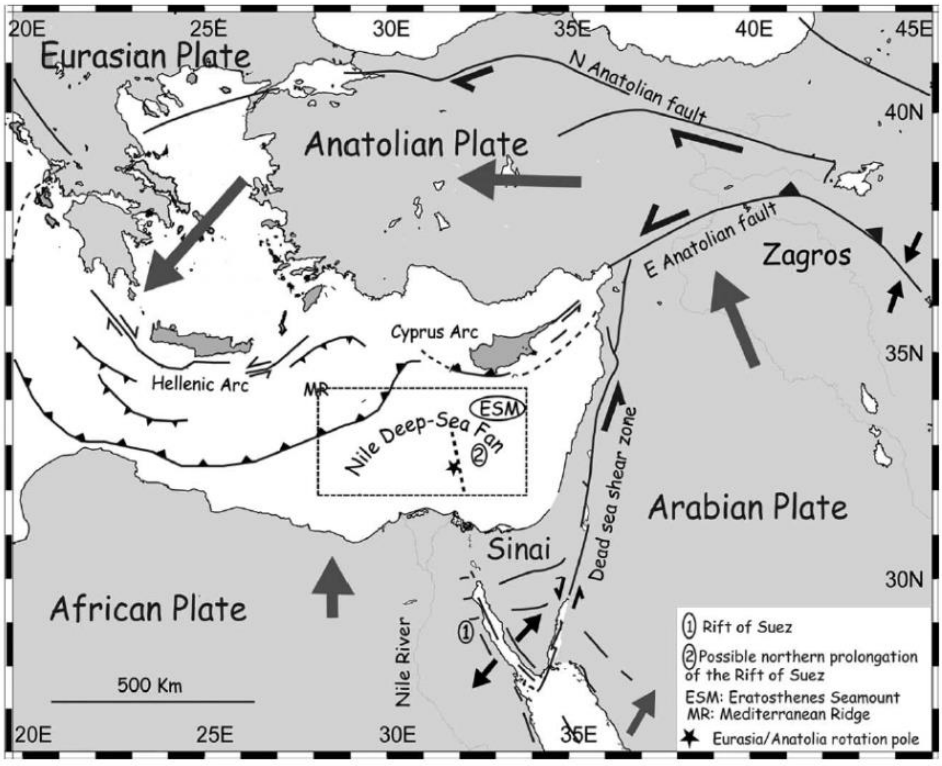

Figure 1.3. Geodynamic setting of the Eastern Mediterranean basin. The study area is indicated by the dotted box, grey arrows represent relative plate motions (Figure from Badawy et al., 2014)

1.2.2. Salt-related Structures in the Nile Delta. Evaporite is a type of rock that originally precipitates from either a saturated surface or near-surface brine (Fossum and Fredrich, 2002). Both halite (NaCl) and anhydrite (Na_2SO_4 or its hydrate form, gypsum) are primary compositions of evaporite. Evaporites are typically referred to as salt. Evaporites discovered in different parts of the world display different degrees of creep properties that are dependent on the proportion of the competent materials (e.g. siliciclastic materials and carbonates) (Warren, 2004). Deformation and displacement occur more easily in response to external forces when evaporites have creep properties. Certain types of evaporites, which have a strong creep behavior, are even able to flow in a manner similar to a Non-newtonian fluid. As a result, the formation of new structures and the reactivation of pre-existing structures are much easier near salt bodies (Tingay et al., 2011). In regions of low pressure and low salt viscosity due to brittle overburden rocks and regional extension (Schultz-Ela and Jackson, 1993), pyramid-shaped salt

diapirs are dominating. In regions where pressure is relatively high and overburden rocks are ductile, dome-shaped salt diapirs are always observed in the subsurface (Figure 1.4.) (Warren, 2004).

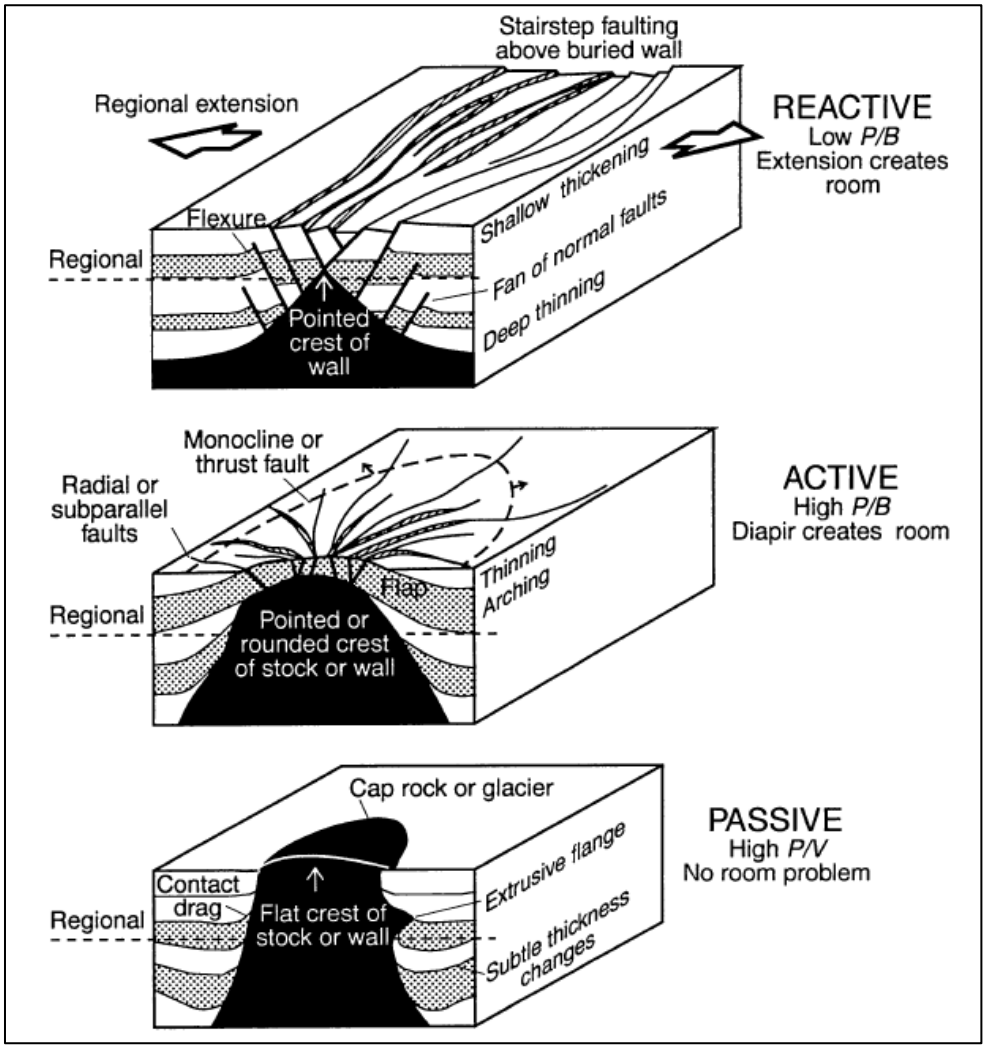

Figure 1.4. Three piercement modes for salt diapirs (black in color) and their related structures. P, V, and B refer to the salt pressure, salt viscosity, and the brittle strength of overburden layer. Figure from Warren, (1994)

For the Nile Delta, large continuous salt layers with "salt pyramids" are present in the northeast portion of the Nile Delta (Loncke et al., 2006; Tingay et al., 2011, 2012). For the supra-salt faults in the Nile Delta, regardless if they are pre-existing or newly formed, the gravitational potential and the influence of the salt layer are the two primary factors that affecting their revolution. Sedimentary mass that has been deposited on the

slope of the clastic wedge possesses a gravitational potential that is large enough to initiate a down-slope-moving tendency. Thus, a series of listric-growth faults are generated under this tendency (Warren, 2004). They are either active or can be easily reactivated due to the continuous accumulation of sediments. In contrast, due to the unique creep property, the salt body is not able to provide the frictional resistance that enough to prevent the movement on the faulting plane which in contact with salt body. As a consequence, supra-salt listric fault groups are incredibly active and their activities are enhanced by the underlain salt bodies or layers (Loncke et al., 2006; Warren, 2004). Inversely, the evolution of supra-salt faults has shaped the adjacent salt layer into "salt pyramids" from their original diapir shape (Warren, 2004) (Figure 1.5.). The fault types vary with respect to the part of the delta region in which they are located. They are also dependent on the regional stress field. Normal faulting groups are present in the extensional region near the delta shelf. Thrust faulting groups are present in the compressional region near the delta toe. And, rotational faults are common in the transition region on the slope (Loncke et al., 2006; Warren, 2004).

1.2.3. Present-day Stress Distribution in the Nile Delta. Four-arm caliper logs and formation micro imager (FMI) resistivity image logs are among the most common used tools in the oil industry to measure the orientation of the maximum horizontal stress (S_H) by identifying the azimuth of breakouts and drilling induced tensile failures (DITF) (Perez et al., 2005). A total of 44 boreholes were drilled in the offshore Nile Delta, and more than 446 breakouts and 19 DITFs have been screened out and analyzed as the regional stress field indicator (Tingay et al, 2011).

The S_H orientations, on average, have a strong regional diversity S_H orientation is in the NNE-SSW direction in the western province of the Nile Delta, E-W in the central province and ESE-WNW in the eastern province, for all of which Messinian evaporites are absent (blue symbols in Figure 1.6). In sharp contrast, S_H orientations are predominately NNE-SSW in the eastern portion that is underlain by Messinian evaporites (yellow symbols in Figure 1.6) (Tingay et al., 2012).

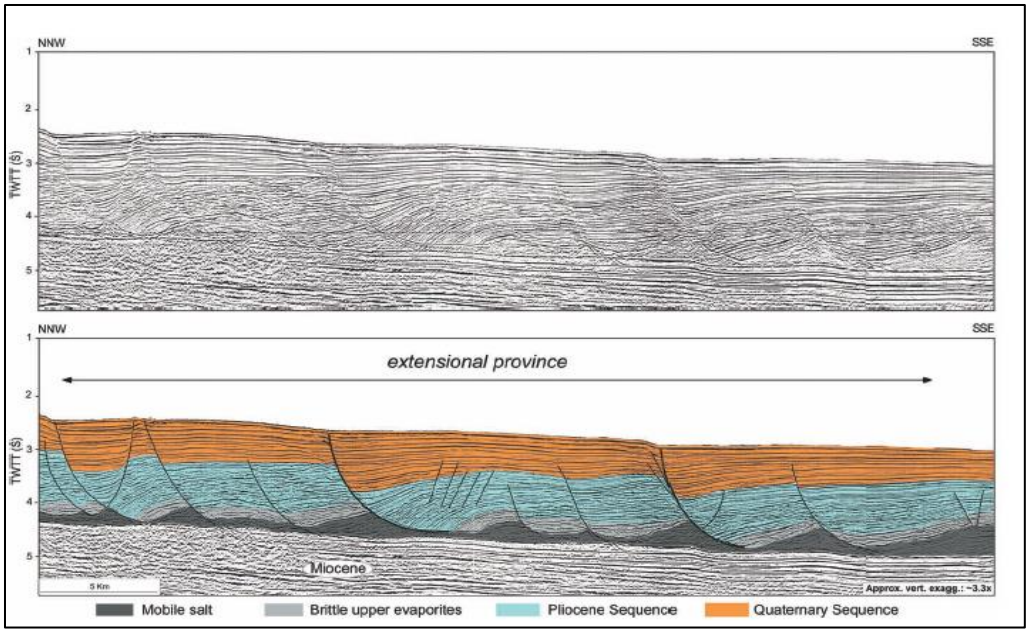

Figure 1.5. Listric fault groups interpreted from seismic data. Local stress field displays extensional, and the mobile salt (dark grey) forms "salt pyramids" (Figure from Reis et al., 2008)

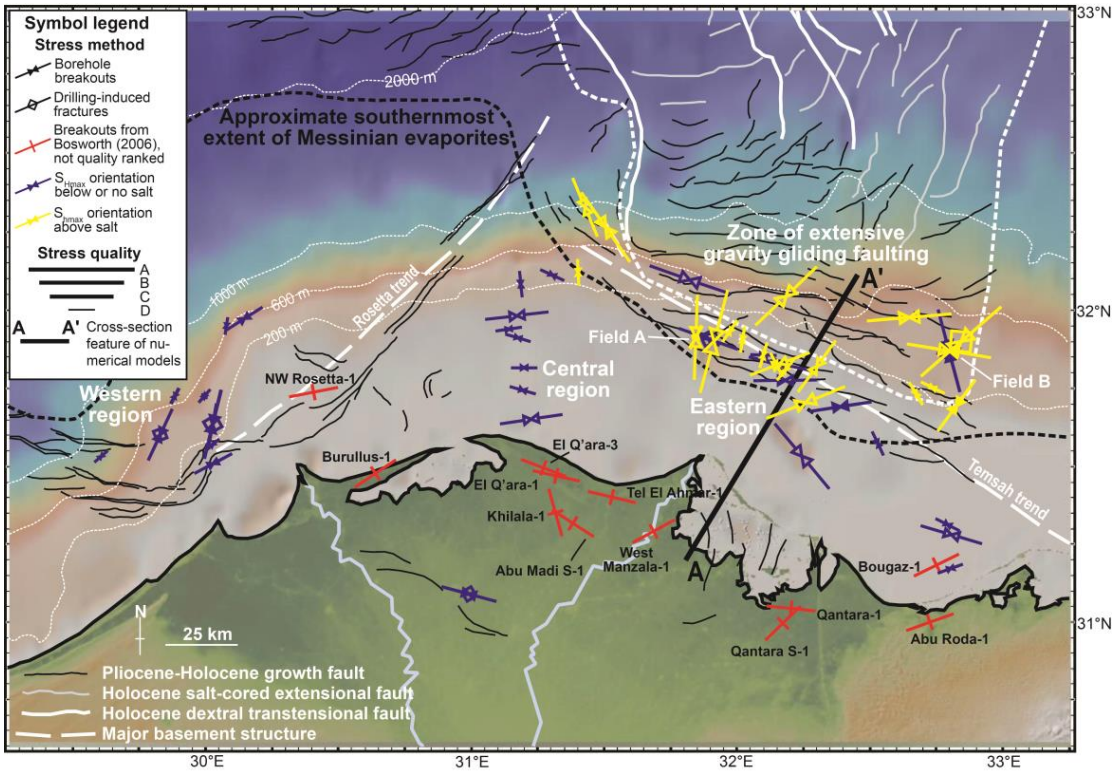

Figure 1.6. Stress distributions in the Nile Delta. Blue symbols indicate S_H orientations in sequences no/below the salt evaporite, yellow symbols represent S_H orientations above the salt evaporite. Figure from Tingay et al. (2012)

The S_H orientations also appear in two different patterns within sequences above and below the Messinian evaporites. Caliper and image logging interpretations of four wells in Field A indicate approximate S_H orientations of NNE-SSW (average 015°N ±9° standard deviation) in supra-salt sequences. And approximate S_H orientations of ESE-WNW (average 110°N ±5° standard deviation) are presented in sequences below the salt layer of Field A (Figure 1.7a). Field B is located at southeasternmost portion of the Nile Delta. Here, the supra-salt S_H orientations are scattered and approximately E-W. The sub-salt, however, is approximately NNW-SSE (Figure 1.7b). Over all, the S_H orientations above and below the salt layer are nearly perpendicular to each other, providing solid evidence that the Messinian evaporite layers serve as a mechanical detachment surface in the Nile Delta (Tingay et al., 2011).

Two hypotheses have been postulated by Tingay et al. (2012) in order to explain how the interaction between the salt layer and the supra-salt faults would lead to abnormal S_H orientations:

a) Gravitational gliding and induced drag forces
b) Mechanical property contrasts resulting in localized stress variations

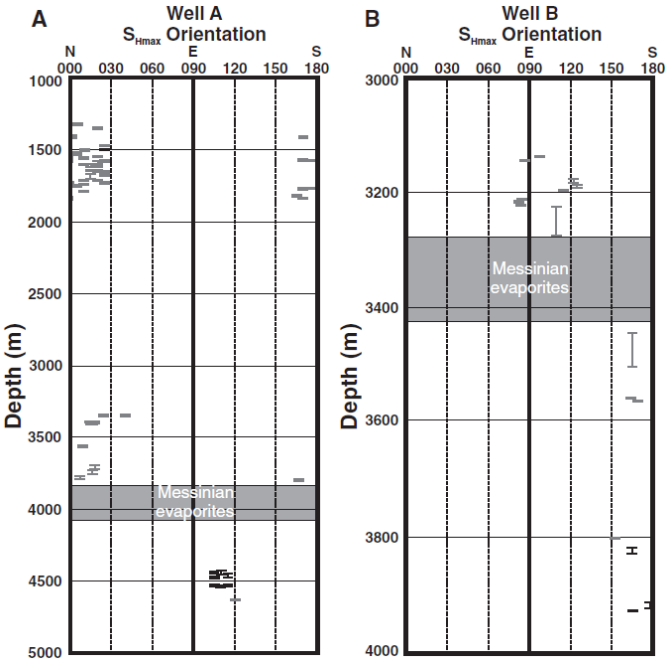

Figure 1.7. S_H orientations versus depth of Field A and Field B. Grey dots are S_H orientations indicated by breakouts and Dark dots are indicated by DITFs. Figure from Tingay et al. (2011)

1.2.4. The Gravitational Gliding Theory. According to the classic theory of stress distribution in a delta region, a typical clastic wedge, which is commonly observed in fluvial deltas, has the following features (Figure 1.8.) (Tingay et al., 2011; Badawy et al., 2014):

- Gravitational spreading is the predominate movement of overburden sediments that are either deforming or sliding along the slope of the clastic wedge because of the critical taper angle of the wedge.
- The delta shelf province (on the continental side) has an extensional stress regime, where S_H orientations are margin-parallel and the faulting type is normal fault.
- The delta toe province (on the sea side) has a compressional stress regime, where S_H orientations are margin-normal and the faulting type is thrust fault.

Based on the classic theory, the margin-parallel $S_{H_{max}}$ orientations are supposed to be in the delta shelf and slope province, and the margin-parallel S_H orientations in the delta toe province (Tingay et al., 2011). The data from the Nile delta shows S_H orientations as expected in the western and central regions, if its fan-shape is considered. Sequences in the eastern region that have either no Messinian evaporites or are below these evaporites also display a consistency with the prediction made by the classic theory. S_H orientations in sequences above the Messinian evaporates, however, appear to be approximately margin-normal rather than margin-parallel. A 90° rotation of the S_H orientation occurs above and below the salt layer, which is extremely unusual and poorly understood (Tingay et al., 2011, 2012).

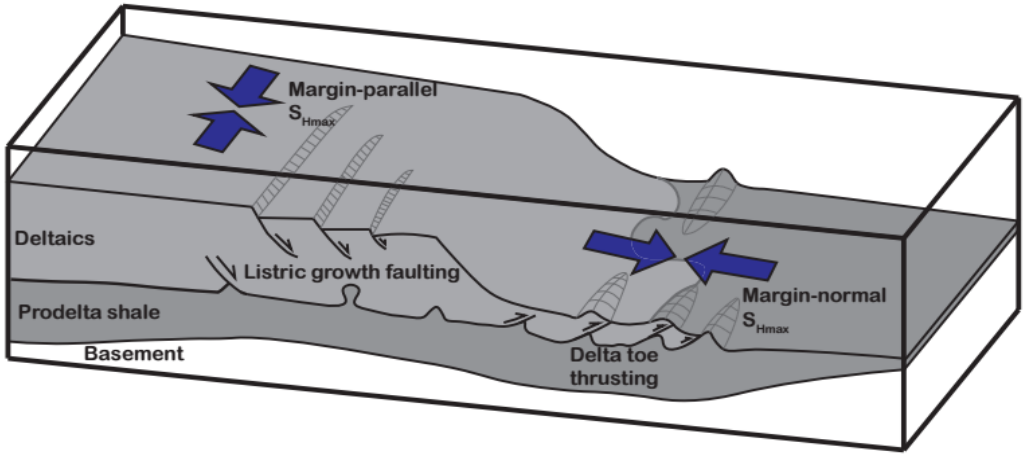

Figure 1.8. The stress distribution in a common delta region (after Tingay et al., 2011)

Tingay et al. (2011) proposed that the 90 degree inconsistency is likely the result of the force exerted by localized, salt-associated gravitational gliding of supra-salt faults. Like dragging a table cloth, the downslope moving tendency of the salt layer may impart a down-slope basal drag force. This force can enhance the faulting movement and generate a margin-normal S_H orientation in the supra-salt sequences. Although the occurrence of a few supra-salt large dextral transtensional faults in this region seems to support the hypothesis, quantitative evidence is insufficient in providing a persuasive basal drag mechanism that can explain the formation of both the present-day stress field and the structural styles in the supra-salt region (Warren, 2004; Tingay et al., 2011).

1.2.5. Localized Stress Variations. The second hypothesis postulated by Tingay et al. (2012) indicates that the margin-normal supra-salt S_H orientation may also be led by localized stress variations related to the special mechanical properties of the Messinian evaporites. For example, field measurements taken from the North Sea and the Gulf of Mexico (Morita and McLeod, 1995; Perez et al., 2005) reveal that S_H orientations in the supra-salt layers appear to be as highly scattered as they are in the eastern Nile Delta. In contrast, the result taken from numerical modeling studies (Jackson, 1994; 2003) indicates that stress orientations in the subsurface can be locally deflected by contrasts in rock elastic properties (e.g. elastic sandstone to visco-elastic evaporite). The S_H orientations tend to be deflected perpendicular to stiff material and parallel to weak materials (Tingay et al., 2010; Schultz-Ela and Jackson, 1993). The salt layer, may be acting as a "cushion", not only deflecting the S_H orientation within the layer but also affecting sequences above the layer (Figure 1.9.). Therefore, a modeling simulation, with key features incorporated, is of significance to unveil how the present-day supra-salt S_H orientations were generated in the eastern Nile Delta.

1.3. RESEARCH OBJECTIVES

Although extensive structural analyses based on seismic interpretation, bathymetric topography, and stress measurements have been conducted (Aal et al., 2000; Mascle et al., 2003; Loncke et al., 2006), no quantitative evidence on the cause of the stress variations in the Nile Delta is available. This study simulates the in-situ stress field

in the Nile Delta using 3D Finite Element Analysis. The main objective of this study is to improve the understanding of how salt bodies act as a mechanical detachment layer. The finite element models are utilized to evaluate if the gravitational gliding theory or mechanical property contrast are the cause for the varying stress orientations in supra and sub-salt sequences.

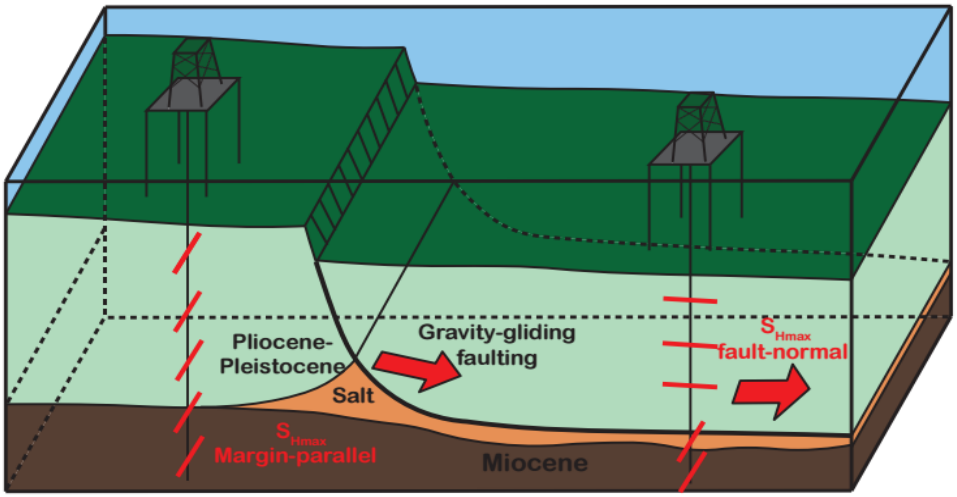

Figure 1.9. Salt evaporite affecting the faulting movement and the distribution of S_H orientations in the deltaic region (figure after Tingay et al., 2011)

1.4. RESEARCH QUESTIONS

The following specific research questions are addressed in this study:

- What is the influence of salt geometry on the distribution of supra- and sub-salt stress orientations?
- What is the influence of other key factors including the friction coefficient of the supra-salt faults and the rheological properties of the salt?
- Which hypothetical scenarios better explains the stress variations in the Nile Delta?

In order to address these questions several sensitivity analyses involving different model geometries, model boundary conditions and material parameters are conducted. Results are analyzed in the context of how S_H orientations distribute above and below the salt layer, i.e. which location near the supra-salt faults the S_H orientations become margin-normal.

2. THEORETICAL BACKGROUND

2.1. FUNDAMENTALS IN ROCK MECHANICS

Rock mechanics is the theoretical and applied science that governs the response of rock to the force field (Jaeger et al., 2007). A good understanding of stress and strain is necessary to understand different behaviors of rocks and interpret the information from geological structures.

2.1.1. Stress. A random rock surface can be uniquely characterized by its unit normal vector. The force imposed by the adjacent rock on the surface can be represented by a resultant force vector ($\vec{F}$). The traction on the surface area A can be defined by the traction vector ($\vec{T}$) as shown in Equation 1.

$$\vec{T}(\vec{n}) = \frac{\vec{F}}{A} \tag{1}$$

The traction vector ($\vec{T}$) over a point on the surface can be defined by limiting the surface area A to infinitesimal:

$$\vec{T}(\vec{n}) = \lim_{dA \to 0} \frac{1}{dA} d\vec{F} \tag{2}$$

Stress is an infinitesimal dynamic abstraction used to define the load level a material point is bearing at a given position and represents a pair of equal and opposite tractions acting on this position. The mathematical definition of stress ($\vec{\sigma}$) can be expressed by Equation 3.

$$\vec{\sigma} = \frac{\vec{F}}{A} \tag{3}$$

The SI unit of stress is the Pascal (1Pa=1N/m^2).

The total result of all the traction vectors passing through all the surfaces at a common point is the state of stress (SOS). The Cauchy stress tensor, comprised of nine components is able to represent the SOS at a point in the three-dimension scenario. The stress tensor can be expressed as:

$$\sigma = \begin{bmatrix} \sigma_{xx} & \tau_{xy} & \tau_{xz} \\ \tau_{yx} & \sigma_{yy} & \tau_{yz} \\ \tau_{zx} & \tau_{zy} & \sigma_{zz} \end{bmatrix} \tag{4}$$

The subscripts of each component are defined in the following rules:

- The subscripts i and j can be any of x, y and z, representing x, y and z axis respectively;
- i identifies the axis which is normal to the surface;
- j shows the direction of the stress component;
- σ_{ii} is the normal stress acting perpendicular to a surface, and τ_{ij} is the shear stress acting on a surface.

E.g. σ_{xx} is the normal stress in x-direction on a surface for which the normal vector is the x axis. The shear stresses on this surface are τ_{xy} and τ_{xz} pointing in the y-direction and z-direction, respectively (Figure 2.1.).

The stress tensor on any static point must be a symmetric matrix. τ_{xy} and τ_{yx}, τ_{xz} and τ_{zx}, and τ_{yz} and τ_{zy} each have the same magnitude. Figure 2.1 illustrates the traction components of the stress tensor on a control cube. The traction vector and the SOS at a point are given by Cauchy's 2nd law:

$$T_i = \sigma_{ij} \cdot n_j \tag{5}$$

Where T_i and σ_{ij} are the stress tensor and the traction vector on a plane, respectively. n_j is the normal vector of this plane. This equation can also be written in matrix form:

$$\begin{bmatrix} T_x \\ T_y \\ T_z \end{bmatrix} = \begin{bmatrix} \sigma_{xx} & \tau_{xy} & \tau_{xz} \\ \tau_{yx} & \sigma_{yy} & \tau_{yz} \\ \tau_{zx} & \tau_{zy} & \sigma_{zz} \end{bmatrix} \begin{bmatrix} n_x \\ n_y \\ n_z \end{bmatrix} \tag{6}$$

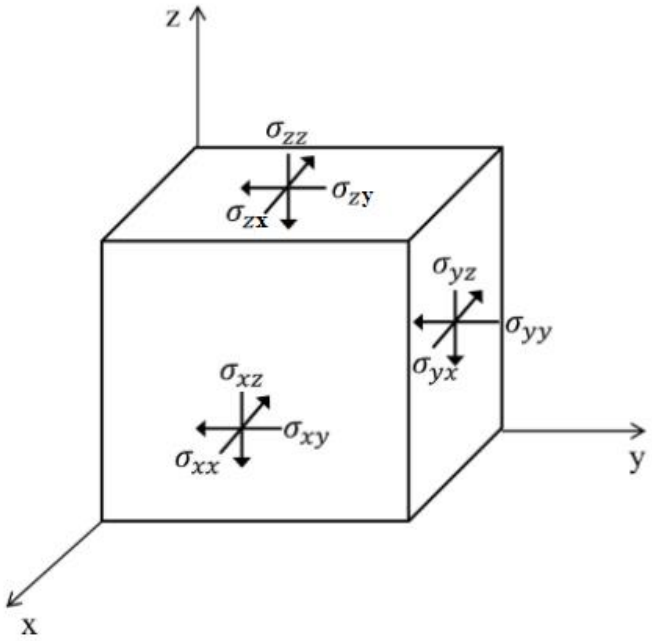

Figure 2.1. Illustration of the unit control cube and stress components acting on it

2.1.2. Principal Stresses. If the control cube shown in Figure 2.1 is rotated within the selected 3D coordinate system, a special direction can be found in which all shear stress components vanish from all surfaces on the control cube. This direction is defined as the principal orientation. The three normal stress components of stress tensor in the principal orientation are principal stresses. They can be expressed as:

$$\sigma = \begin{bmatrix} \sigma_1 & 0 & 0 \\ 0 & \sigma_2 & 0 \\ 0 & 0 & \sigma_3 \end{bmatrix} \tag{7}$$

For a random stress tensor, the corresponding principal stress tensor can be calculated by performing a principal axis transformation (Jaeger et al., 2007), which is obtained from:

$$\boldsymbol{\lambda \cdot X = X \cdot \sigma_{ij}} \quad \text{or} \quad \boldsymbol{\lambda = X \cdot \sigma_{ij} \cdot X^T} \tag{8}$$

Where $\boldsymbol{\sigma_{ij}}$ is the stress tensor at a point; $\boldsymbol{\lambda}$ is the eigenvalue matrix which is also the principal stress tensor; **X** is the eigenvector matrix and this matrix is related with the principal orientation. It needs to be noted that eigenvalue and eigenvector matrixes are uniquely for only one stress tensor and they can be calculated only based on the given

stress tensor. Moreover, directions three principal stress components are pointing to can be derived from the eigenvector matrix.

The von Mises Stress is a scalar stress that is used in determining the yield/failure of isotropic material when subjected to a complex loading condition. The von Mises Stress can be calculated from the principal stress tensor:

$$\sigma_v = \sqrt{\frac{1}{2}[(\sigma_1 - \sigma_2)^2 + (\sigma_2 - \sigma_3)^2 + (\sigma_3 - \sigma_1)^2]} \tag{9}$$

For The magnitude of the von Mises Stress represents the amount of differential stress, which is able to determine the likelihood of failure.

2.1.3. Strain and Strain Rate. Deformation will occur on a rock body when a force is acting on it. The term of strain is used to describe the amount of deformation. The generalized definition of strain can be introduced in a one-dimension context: the ratio of length change over the original length. The strain at a point *x* can be expressed by taking the limit of the infinitesimal shortening, where the original length equals to zero. The mathematical expression can be written as:

$$\varepsilon(x) = \lim_{L \to 0} \frac{L - L^*}{L} = \lim_{\Delta x \to 0} \frac{u(x + \Delta x) - u(x)}{\Delta x} \equiv \frac{du}{dx} \tag{10}$$

This definition can be generalized to 3D scenarios:

$$\varepsilon_{ij} = \frac{1}{2}\left(\frac{\partial u_i}{\partial x_j} + \frac{\partial u_j}{\partial x_i}\right) \tag{11}$$

Strain is a unitless parameter which displays the extent of deformation. Analogue to stress, strain also has directionality, and can be divided into normal strain and shear strain: normal stress induces normal strain and shear stress leads to shear strain. Moreover, the strain tensor, including normal strain and shear strain components, is used to express the strain condition on a point within a body under loading.

The strain rate, a parameter that measures the rate of strain magnitude change is defined as:

$$\dot{\varepsilon} = \frac{d\varepsilon}{dt} \tag{12}$$

The SI unit of strain rate ($\dot{\varepsilon}$) is s^{-1}. Most rock deformation develops at a very small strain rate, and 10^{-13}-10^{-14} s^{-1} is the general range of geological strain rates (Davis et al., 2011).

2.2. ROCK BEHAVIOR

How rock responses to the forces is fundamental in the discipline of rock mechanics. The mechanical properties of rocks can be interpreted in different scales. When the dimension increases to several kilometers, small and regional geological structures, such as preexisting fractures and joints, will not affect the continuity of large sequences. Only major large-scale structures and the overall rock property of continuous components are taken into consideration (Fjaer et al., 2008).

According to the relationship between stress and strain, three basic constitutive laws are able to describe the response of rock individually or in combination: elastic, plastic and viscous (Jaeger et al., 2007). Elasticity and plasticity are independent of time, for which strain develops instantaneously when subjected to a stress. Strain generated in elastic materials is proportional with the magnitude of stress. Viscous and viscoelastic materials, when subjected to loading, however, will generate strain gradually. Multiple factors, such as depth, temperature, pore pressure, and mineral composition, determine the rock properties (Turcotte and Schubert, 2001). The mechanical properties of each kind of rock need to be understood thoroughly in order to analyze the complex stress field induced by the interaction of different types of rock. As the interaction of elastic sediments and viscoelastic salt bodies is investigated in this study, a short summary of the theory of elasticity, viscosity, and viscoelasticity is given.

2.2.1. Elasticity. Elasticity is the tendency of solid materials to recover to their original shape after being deformed by either internal or external forces (Jaeger et al., 2007). Linear elasticity is the most fundamental and widely-used form of elasticity. Linear elasticity is described by the general Hooke's law:

$$\sigma_{ij} = C_{ijkl}\varepsilon_{kl} \tag{13}$$

C_{ijkl} is named the elasticity matrix that represents how the rock responses to an in-situ stress. It is defined that i, j, k, l may take the direction of x, y, or z, respectively.

The elasticity matrix contains the elastic constants such as the Young's modulus, E, and the Poisson's ratio, ν. The Young's modulus measures the axial stiffness of a linear elastic material under a load as stress per area that is needed to compress or stretch a rock sample (Jaeger et al., 2007). The SI unit of Young's Modulus is Pascal or Pa. It needs to be noted that the linear relationship between stress and strain, in general, is only valid when the deformation is very small. The Poisson's ratio (ν) is defined as the negative ratio of lateral strain to longitudinal strain, as presented in equation 14:

$$\nu_{ij} = -\frac{\varepsilon_i}{\varepsilon_j} \tag{14}$$

For isotropic rock, the same Young's Modulus and Poisson's Ratio can be used to express elasticity in all directions. Hence, the linear elasticity can be simplified and transformed in matrix form using the Voight notation:

$$\begin{bmatrix} \sigma_{xx} \\ \sigma_{yy} \\ \sigma_{zz} \\ \sigma_{yz} \\ \sigma_{zx} \\ \sigma_{xy} \end{bmatrix} = \frac{E}{(1+\nu)(1-2\nu)} \begin{bmatrix} 1-\nu & \nu & \nu & 0 & 0 & 0 \\ \nu & 1-\nu & \nu & 0 & 0 & 0 \\ \nu & \nu & 1-\nu & 0 & 0 & 0 \\ 0 & 0 & 0 & 1-2\nu & 0 & 0 \\ 0 & 0 & 0 & 0 & 1-2\nu & 0 \\ 0 & 0 & 0 & 0 & 0 & 1-2\nu \end{bmatrix} \begin{bmatrix} \varepsilon_{xx} \\ \varepsilon_{yy} \\ \varepsilon_{zz} \\ \varepsilon_{yz} \\ \varepsilon_{zx} \\ \varepsilon_{xy} \end{bmatrix} \tag{15}$$

2.2.2. Viscous Behavior. Viscosity is the property of a fluid that measures its resistance to a gradual deformation when subjected to a load. According to the relationship between strain rate and stress, a viscous fluid can be classified into several categories. Among them, the Newtonian fluid is the simplest type, which is characterized by a linear time-independent relationship between stress and strain rate (Figure 2.2.).

The viscosity of a Newtonian fluid is defined as the slope of the line, which is independent of stress and time. Hence, a Newtonian fluid is also referred as a pure viscous fluid and is represented by a massless dashpot in a physical model. The relationship of shear stress, shear strain rate and viscosity of a Newtonian fluid can be expressed as:

$$\sigma = 2\mu\dot{\varepsilon}^v = 2\mu\frac{d\varepsilon^v}{dt} \tag{16}$$

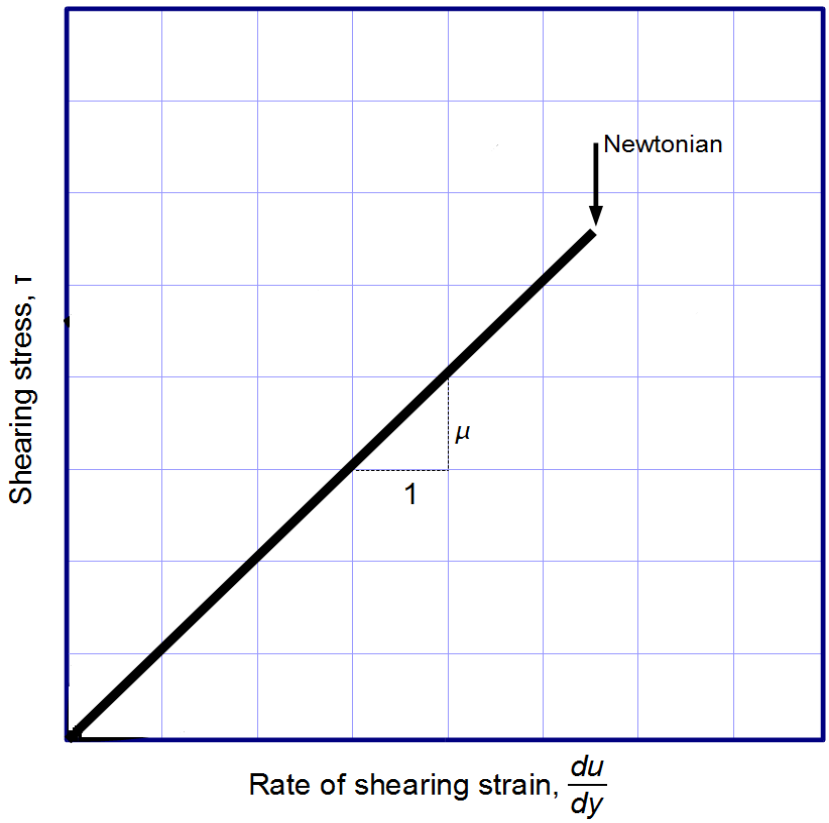

Figure 2.2. The shear stress vs. shear strain rate plot. Figure from Jaeger et al. (2006)

Where, $\dot{\varepsilon}^{v}$ is the viscous strain rate; ε^{v} is the viscous strain; σ is the deviatoric normal stress; μ is the dynamic viscosity of the Newtonian fluid The SI unit of viscosity is Pa·s. The total normal force acting on the fluid element is the sum of the fluid pressure and the viscous stress, as shown by Equation 17 to Equation 19:

$$\sigma_1 = p - \tau_1 = p - 2\mu\frac{\partial u}{\partial x} \tag{17}$$

$$\sigma_2 = p - \tau_2 = p - 2\mu\frac{\partial v}{\partial y} \tag{18}$$

$$\sigma_3 = p - \tau_3 = p - 2\mu\frac{\partial w}{\partial z} \tag{19}$$

Where fluid pressure p is defined as $p = \frac{1}{3}(\sigma_1 + \sigma_2 + \sigma_3)$ in a 3D scenario. It needs to be clarified that the system is considered to be isotropic and the fluid flow is assumed to be steady-state and without a resulting net torque.

The strain rate of a Newtonian fluid subjected to a deviatoric normal stress can be expressed as:

$$\dot{\varepsilon}^{v} = \frac{d\varepsilon^{v}}{dt} = -\frac{\partial u}{\partial x} = \frac{\sigma}{2\mu} \tag{20}$$

Inserting Equation 20 into Equations 17 to 19, the viscous strain rate along x, y, and z axis can be presented as:

$$\dot{\varepsilon}_1^{v} = \frac{d\varepsilon_1^{v}}{dt} = \frac{1}{2\mu}(\sigma_1 - p) = \frac{1}{\mu}(\tfrac{1}{3}\sigma_1 - \tfrac{1}{6}\sigma_2 - \tfrac{1}{6}\sigma_3) \tag{21}$$

$$\dot{\varepsilon}_2^{v} = \frac{d\varepsilon_2^{v}}{dt} = \frac{1}{2\mu}(\sigma_2 - p) = \frac{1}{\mu}(-\tfrac{1}{6}\sigma_1 + \tfrac{1}{3}\sigma_2 - \tfrac{1}{6}\sigma_3) \tag{22}$$

$$\dot{\varepsilon}_3^{v} = \frac{d\varepsilon_3^{v}}{dt} = \frac{1}{2\mu}(\sigma_1 - p) = \frac{1}{\mu}(-\tfrac{1}{6}\sigma_1 - \tfrac{1}{6}\sigma_2 + \tfrac{1}{3}\sigma_3) \tag{23}$$

Where σ_1, σ_2, and σ_3 are normal stresses along x, y , and z axes; p still represents fluid pressure as $p = \frac{1}{3}(\sigma_1 + \sigma_2 + \sigma_3)$. This relationship can also be expressed in matrix form:

$$\{d\varepsilon^{v}\} = [Q]^{-1}\{\sigma^{t}\}dt \tag{24}$$

or

$$\begin{bmatrix} \dot{\varepsilon}_1^{v} \\ \dot{\varepsilon}_2^{v} \\ \dot{\varepsilon}_3^{v} \end{bmatrix} = \frac{1}{\mu}\begin{bmatrix} \frac{1}{3} & -\frac{1}{6} & -\frac{1}{6} & 0 & 0 & 0 \\ -\frac{1}{6} & \frac{1}{3} & -\frac{1}{6} & 0 & 0 & 0 \\ -\frac{1}{6} & -\frac{1}{6} & \frac{1}{3} & 0 & 0 & 0 \\ 0 & 0 & 0 & 1 & 0 & 0 \\ 0 & 0 & 0 & 0 & 1 & 0 \\ 0 & 0 & 0 & 0 & 0 & 1 \end{bmatrix}\begin{bmatrix} \sigma_1 \\ \sigma_2 \\ \sigma_3 \\ 2\tau_{23} \\ 2\tau_{13} \\ 2\tau_{12} \end{bmatrix} \tag{25}$$

$$[Q]^{-1} = \frac{1}{\mu}\begin{bmatrix} \frac{1}{3} & -\frac{1}{6} & -\frac{1}{6} & & & \\ -\frac{1}{6} & \frac{1}{3} & -\frac{1}{6} & 0 & 0 & 0 \\ -\frac{1}{6} & -\frac{1}{6} & \frac{1}{3} & & & \\ 0 & 0 & 0 & 1 & 0 & 0 \\ 0 & 0 & 0 & 0 & 1 & 0 \\ 0 & 0 & 0 & 0 & 0 & 1 \end{bmatrix} \quad (26)$$

Where $[Q]$ is the property matrix of Newtonian viscous material, which is defined as Equation 26.

2.2.3. Viscoelasticity. Viscoelasticity refers to a material that behaves both elastic and viscous characteristics when undergoing deformation (Jaeger et al., 2007). In general, a visco-elastic material, when subjected to a load, will have an instantaneous elastic response and a long-term viscous response (Turcotte and Schubert, 2008). Several physical models are established to describe the viscoelastic behavior shown in different materials. The Maxwell model is a simple viscoelastic model that approximates the stress-strain response of the viscoelastic material with an elastic spring and a viscous dashpot in series (Figure 2.3). The dashpot and spring are assumed massless and the load (stress) carried by each of them is assumed to be equal all times. Thus, the total stress and strain of the system is governed by the time-independent strain rate, as expressed by the first-order differential equation below:

$$\dot{\varepsilon} = \dot{\varepsilon}_{spring} + \dot{\varepsilon}_{dashpot} = (\dot{\sigma}/k) + (\sigma/\eta) \quad (28)$$

Where $\dot{\sigma}$ is the rate of elastic stress change; and $\dot{\varepsilon}$ is the strain rate of the system.

The constitutive relationship of the Maxwell viscoelastic model shown in equation 27 indicates that the total strain consists of two parts: an elastic strain (ε_{ij}^{e}) and a viscous strain (ε_{ij}^{v}):

$$\varepsilon_{ij} = \varepsilon_{ij}^{e} + \varepsilon_{ij}^{v} \quad (29)$$

It needs to be noted that, as shown in Figure 2.3b, a Maxwell visco-elastic material, when subjected to a load, will have an instantaneous elastic response and a

long-term viscous response. Inserting Equation 14 and Equation 25 into Equation 28, the total strain in the system can also be expressed in a matrix form:

$$\{d\varepsilon\} = \{d\varepsilon^v\} + \{d\varepsilon^e\} = [Q]^{-1}\{\sigma^t\}dt + [D]^{-1}\{d\sigma\} \tag{30}$$

$$[Q]^{-1} = \frac{1}{\eta}\begin{bmatrix} \frac{1}{3} & -\frac{1}{6} & -\frac{1}{6} & 0 & 0 & 0 \\ -\frac{1}{6} & \frac{1}{3} & -\frac{1}{6} & 0 & 0 & 0 \\ -\frac{1}{6} & -\frac{1}{6} & \frac{1}{3} & 0 & 0 & 0 \\ 0 & 0 & 0 & 1 & 0 & 0 \\ 0 & 0 & 0 & 0 & 1 & 0 \\ 0 & 0 & 0 & 0 & 0 & 1 \end{bmatrix} \tag{31}$$

and

$$D = \frac{E}{(1+v)(1-2v)}\begin{bmatrix} 1-v & v & v & 0 & 0 & 0 \\ v & 1-v & v & 0 & 0 & 0 \\ v & v & 1-v & 0 & 0 & 0 \\ 0 & 0 & 0 & 0.5-v & 0 & 0 \\ 0 & 0 & 0 & 0 & 0.5-v & 0 \\ 0 & 0 & 0 & 0 & 0 & 0.5-v \end{bmatrix} \tag{32}$$

Where [Q] is the viscous material property matrix and [D] is the elastic material property matrix.

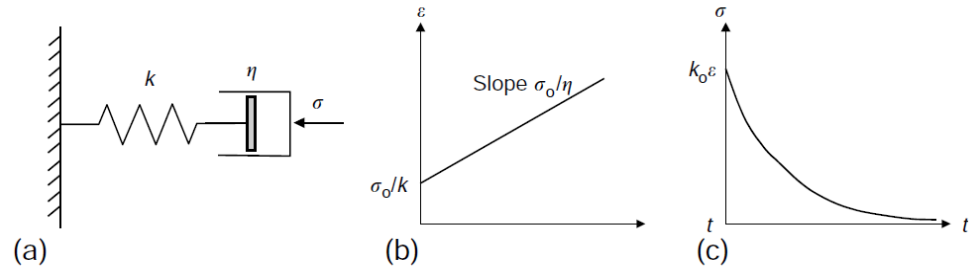

Figure 2.3. Illustrations of physical models for material with different mechanical properties. (a) Physical model of Maxwell visco-elastic material. (b) Response of a Maxwell material to an instantaneously applied load (stress). (c) Response of a Maxwell material to an instantaneously applied load (strain). Figure after Jaeger et al. (2007)

2.2.4. Creep. Creep represents irreversible time-dependent deformation at constant stress and temperature. Metals, polymers, unconsolidated concretes and rocks are materials that present creep behavior. When subjected to an external load, materials with creep more easily deform and behave more ductile rather than brittle (Figure 2.4.). When the load is removed, the deformation only recovers partially. A certain part of deformation, depending on the type of material and the magnitude of the load, cannot be recovered permanently (Figure 2.4.). Creep has two major categories:

- Solid state diffusion dominated creep. Thermal energy is the main driving force for the inter-atomic diffusion of solid state creep. This type of creep always occurs at high temperature.
- Gliding dominated creep. At relatively low temperatures or high stress environment, materials may behave more plastic and inter-atomic or inter-grain gliding will dominate creep response.

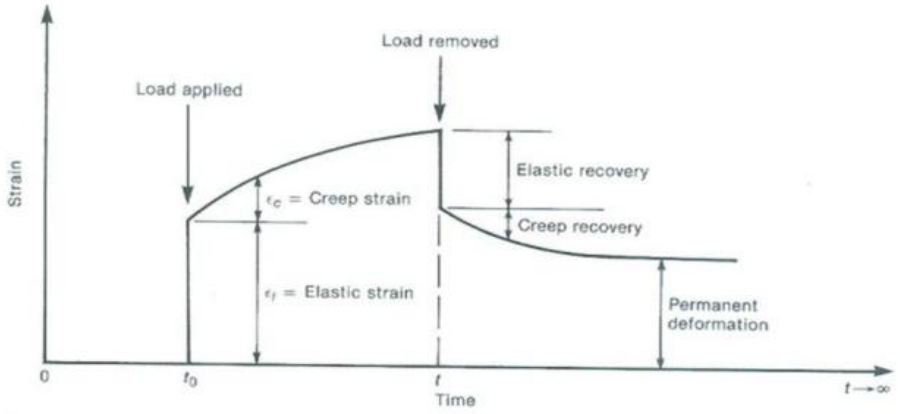

Figure 2.4. Creep strain – time curve (Figure from McGregor et al., 2005)

Tar sands, compaction shales and salt rock have very prominent creep behaviors among all types of rock (Goodman, 1989). Salt, under a relatively high magnitude of deviatoric stress and low temperature, presents creep behavior due to its unique microcrystalline structure: the slipping between its crystal planes occurs easily. As shown in Figure 2.5, Jackson et al. (1994) illustrates the three creep stages:

- Stage 1, primary creep stage. When the material is subjected to a constant load, the deformation (strain) increases, but the rate of increasing reduces gradually.

This process is also called *work hardening*. The strain rate keeps decreasing until it reaches a constant value.

- Stage 2, secondary creep stage. This stage is also referred to as *steady-state creep*. At this stage, the strain-time curve stays in a linear form and the deformation is increasing at a constant rate. Secondary creep is the most stable and long-lasting stage for the majority of all creep materials.
- Stage 3, tertiary creep stage. When the testing time becomes long enough, the stress and strain accumulated would exceed the tolerance of the material. During this stage, the strain rate increases exponentially and the material deforms drastically. As a result, brittle behavior gradually overcomes the ductile behavior and failure will finally occur.

Since the overburden pressure on Messinian evaporites is relatively stable and no drastic changes occurs, secondary creep is the only creep behavior that salt bodies experience under the in-situ environment. As a result, a physical law that represents steady-state creep is sufficient to define the creep response of salt bodies in this numerical modelling study.

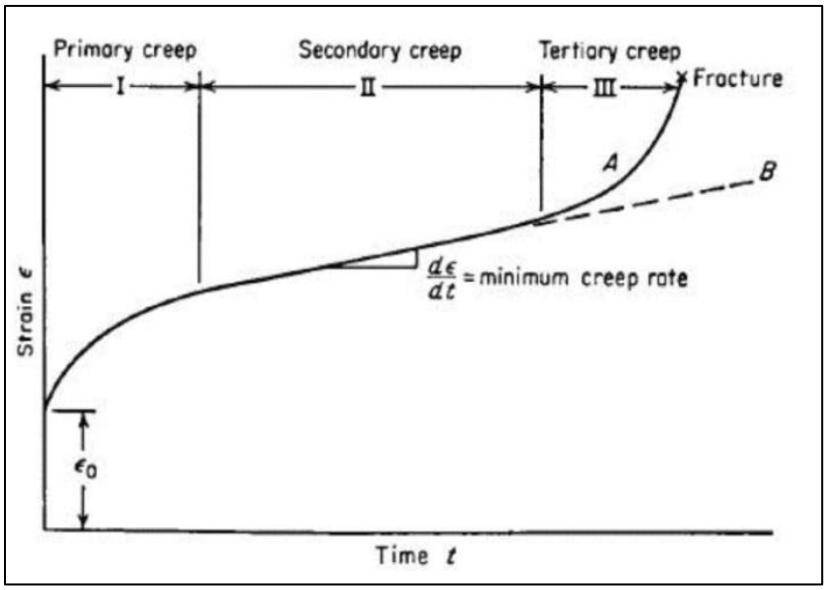

Figure 2.5. Strain – time curve of salt rock that exhibits creep behavior (From Jackson et al., 1994)

The Maxwell model, as introduced previously, is a simple viscoelastic model that is suitable to describe the secondary stage of salt rock creep (Senseny et al., 1992), because of their similarity in stress-strain rate relationship (both stress-strain rate show linear and time-independent). Thus, the constitutive relationships of the Maxwell viscoelastic model shown in Equation 26-30 are able to define creep response of the salt bodies in this study.

Senseny et al., (1992), Cristescu et al., (1993), Keken et al., (1993), and Gampala et al., (1995) also established empirical creep laws according to data obtained from strain tests. They are known as the logarithmic law, the exponential law, and the power law. The logarithmic and exponential laws are used to simulate the creep behavior of metal and polymers and the power law is more suitable to describe salt rocks (Senseny et al., 1992; Cristescu et al., 1993; Davis et al., 2011). The equation of power law creep can be written as:

$$\varepsilon^c = A\sigma_d^n t^m \tag{33}$$

Where: ε^c is the transient creep strain; σ_d is the deviatoric stress; t is the time; and A, a, m, n are temperature dependent material constants. It needs to be noted that the transient creep strain calculated by Equation 28 represents the steady state creep strain after transformation, as will be discussed in Chapter 3.4.

2.2.5. Frictional Properties. Friction is the phenomenon occurring when two discrete surfaces in contact are oppositely displaced along a direction parallel to their contact plane by a shear force, which is sufficient to overcome the resistance induced by the roughness of the contacting bodies. A thorough understanding of friction is of great significance for rock mechanics. Several physical models are proposed to express the frictional response of materials with different mechanical properties and under different conditions. The most universal model divides the friction into a static friction at the initiation and a dynamic friction during sliding.

$$T_f = T_{fs} + T_{fd} = \mu_s N + \mu_d N \tag{34}$$

Where: T_f is the friction force; T_{fs} and T_{fd} are static and dynamic friction forces; μ_s and μ_d are static and dynamic friction coefficient; N is the normal load acting on the contact surface.

Byerlee (1978) found that bilinear empirical equations are able to represent the frictional behavior for rocks at certain circumstances. This behavior is affected by in-situ pressure rather than rock type. The following equations show the relationship between shear stress necessary to overcome friction (τ) and normal stress (σ):

$$\tau = 0.85\sigma \quad \text{for } \sigma<200\text{MPa} \tag{35}$$

$$\tau = 50\text{MPa}+0.6\sigma \quad \text{for } 200< \sigma<1700\text{MPa} \tag{36}$$

Byerlee's law is applicable to rocks that have the following features:

- predominantly brittle behavior
- shallow burial depth with low in-situ stresses
- more suitable when fracturing/sliding along a pre-existing fault

Considering the depth of supra-salt faults (0-4000m) and the vertical stress magnitude (0-80MPa), Byerlee's law predicts that the frictional behavior of supra-salt faults is characterized by a linear relationship between frictional shear stress and normal stress. Rae (1963), Jaeger (1959), and Hoskins et al., (1968) provide a reasonable friction coefficient (μ) range for shallow sedimentary rock: 0.42 to 0.64. Hence, in this study, a friction coefficient (μ) of 0.6 will be applied in the basic model, and the value of 0.4 and 0.2 will be tested to evaluate the influence of friction enhancement.

3. MODELING METHOD

3.1. NUMERICAL ANALYSIS

The development of digital computational technology and the advance in numerical methods have significantly helped to simulate physical processes in the field of rock mechanics subjected to complex boundary conditions and provide approximate solutions. Many numerical methods feature the following steps, as shown in Figure 3.1) dividing a continuous domain (Figure 3.1a) into many smaller units (discretization); 2) calculating solutions at selected points within the model and approximating solutions to the whole domain (approximation). Due to the specific distinction in discretization and approximation, there are several mainstream numerical methods which aim to solve different problems. They include the Finite Element Method (FEM), the Finite Difference Method (FDM), the Discrete Element Method (DEM) and the Boundary Element Method (BEM). Zienkiewicz (2005) compared the FEM with other numerical methods and concludes that the FEM has advantages on solving problems with very complex geometries, multiple material behaviors, and drastic changes in short period of time.

Numerical modeling methods are of great importance in geosciences. Numerical models enable to simulate the evolution of geological structures over a long period. Numerical models are able to incorporate many key features such as mechanical properties of different rocks, the pore pressure distribution, boundary constrains of the modeling domain, and both external and internal loads. It needs to be noted that rather than reproducing what happened in nature in detail, the true strength of numerical methods are that it approximates mathematical solutions at acceptable precision and thus guarantees that whole system is modeled with a relatively high accuracy (Healy et al., 2012). Striking a balance between modeling accuracy and limited computational resource is among top concerns of a numerical modeling study.

3.2. FINITE ELEMENT METHOD (FEM)

Zienkiewicz (2005) defined the FEM as "a numerical method for finding approximate solutions to boundary value problems for partial differential equations (PDE)". Physical processes such as rock deformation are described by the governing PDE and the corresponding boundary conditions of the problem acting in/over a specific domain (i.e. an area or volume). A PDE is a mathematical expression that describes a continuous physical process in which dependent variables are functions of independent variables (partial derivatives). PDEs comprise the kinematic process, the constitutive law of the material, and the equilibrium equations. Boundary conditions represent known solutions of the unknown or tractions on the domain boundary. As introduced previously, a continuous domain can be discretized into many "finite elements". The corners of elements that border on adjacent elements or the joints where elements intersect with each other are defined as "nodes". For this study, rock properties and external/internal loads are considered as known factors, and the displacement of each node is unknown. For a single element within the system, the general equation for describing the force-displacement relationship can be written as:

$$q^e = K^e u^e + f^e \tag{37}$$

Where q^e is the nodal force acting on the element; K^e is the element stiffness matrix; u^e is the displacement vector of the nodes of the element and is the unknown in this equation; f^e is the nodal force vector representing any external load acting on the element; q^e, u^e, and f^e can be vectors that contain m components which representing each node of the element. In order to obtain approximate solution for the displacement at any point within a finite element, the displacement vector of the system ($\vec{u}$) can be approximated by Equation 38:

$$\vec{u} \approx \tilde{u} = \sum_a \overrightarrow{N_a} \widetilde{u_a^e} \tag{38}$$

$\overrightarrow{N_a}$ is the shape function that prescribes the geometry of the element in terms of independent variables and enables to obtain an approximate solution at any point within the element; $\widetilde{u_a^e}$ refers to the displacement vector for each nodes. Based on the shape

functions derived for each individual element, the force equilibrium for all elements in the system (i.e. $\Sigma(Ku+f)=0$) can be achieved by assembling a global equation sets and solving for u, as shown in Equation 39:

$$Ku + f = 0 \tag{39}$$

Here, K is the global stiffness matrix; u is the unknown displacement vector; f is the nodal forces required to balance any load acting on the element. FEM simulators are able to solve Equation 34 and provide the value of u at each node. Thus, the stress and strain magnitudes can be calculated at each node and the state of stress for the modeling domain can further be obtained. In this study, the software package Abaqus^{TM} (Hibbit et al., 2001) is used for the FE simulations and Altair Hypermesh is used as a pre-processor to discretize the modeling domain.

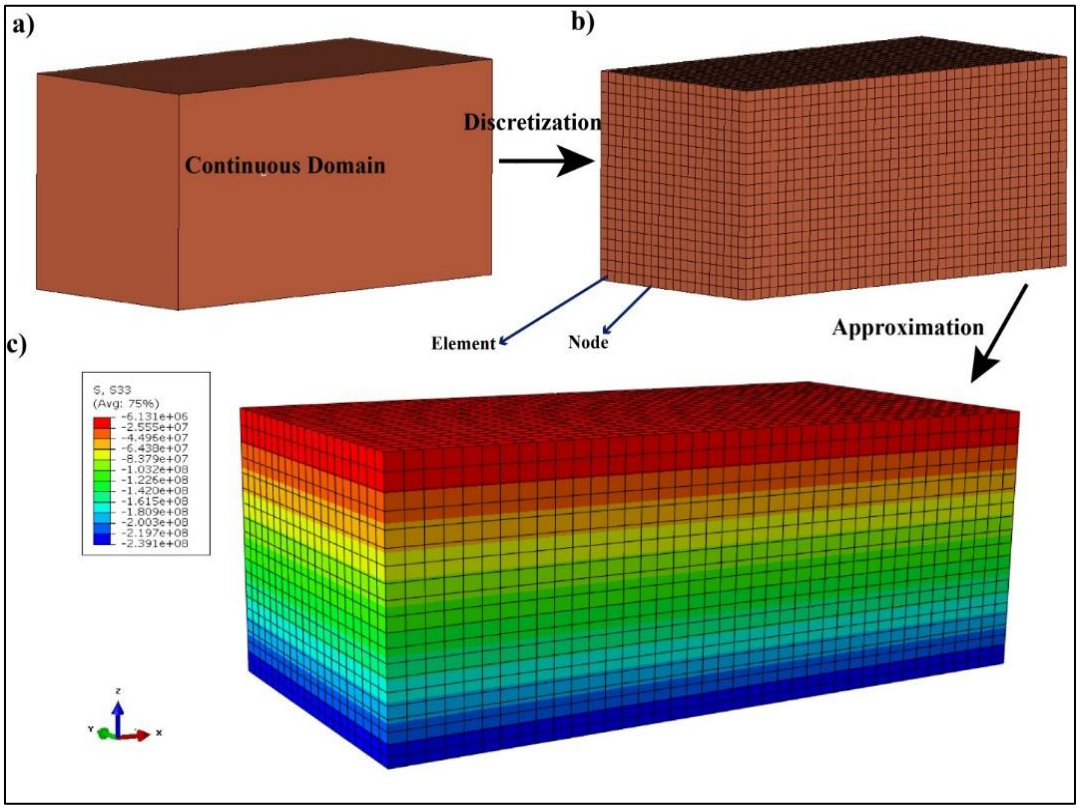

Figure 3.1. The general procedure of numerical modeling method. a) Continuous domain, and it can be discretized into many small units as shown in b). After proper material properties and boundary conditions are applied, etc. a simulator is able to provide modeling result, as shown in c)

3.3. FINITE ELEMENT ANALYSIS (FEA) FOR IN-SITU STRESS SCENARIOS

A rock body in the subsurface is subjected to an in-situ stress field transmitted by the surrounding rocks and is in a state of equilibrium. Rocks are subjected to the gravitational load resulting from the overburden and horizontal loads from different sources (i.e. tectonic forces, lateral density contrasts, Poisson's effect, etc.) (Jaeger et al., 2007). Since numerical modeling studies only simulate rock behavior over a limited time period, they are unable to reproduce the gradual loading procedure and the same in-situ environment that the rock has experienced during its depositional history. In a numerical model gravitational and horizontal loads are added to the rock body instantaneously, which may induce different responses due to different material properties of rock, which will induce instantaneous displacements across the model. As a Maxwell visco-elastic material, the salt body generates high stress magnitudes, which may need a very long time to relax. Numerical simulations involving the creep-behavior material such as salt need to ensure that the stresses have enough time to equilibrate and dissipate across the modeling domain (Schultz-Ela, Jackson, 1993; Fredrich et al., 2003; Buchmann and Connolly, 2007).

Buchmann and Connolly (2007) and Eckert and Liu (2014) proposed a pre-stressing method to overcome the rapid loading problem in numerical simulations for geological structures. Pre-stressing consists of two steps to achieve a gradually and balanced loading status. In the first step, the model is subjected to the gravitational load and horizontal loads (for models featuring lateral displacement boundary conditions) and elastic properties are assigned to each component. The resulting state of stress will be used as an initial equilibrated stress field in a second (time dependent) load step which introduces the creep behavior of salt bodies. The simulation time period is determined based on the degree of relaxation of the salt body (von Mise stress <1MPa) (Fredrich et al., 2003), by which a relatively steady state is attained within the entire model domain.

3.4. MODEL GEOMETRY AND BOUNDARY CONDITIONS

Based on data from seismic surveys, bathymetric surveys, and the structural analysis of the Nile Delta (Martin et al., 2004; Mascle et al., 2003; Loncke et al., 2006), a

100 km long, 1 km wide, and 10 km deep cross sectional model geometry is chosen (line A-A' in Figure 3.2) to represent the typical geometrical features of the offshore Nile Delta. Messinian evaporites (pink in Figure 3.3.) are distributed in the offshore part of the deltaic sediments and listric growth faults separate sedimentary blocks overlaying the Messinian evaporites (Figure 3.3.). Since the detailed geometry of the subsurface structures and the exact spatial distribution of the evaporites are not known in sufficient detail (Tingay et al., 2011), the model geometry is simplified based on a structural analysis of the Nile Delta by Marten et al. (2004) (Figure 3.3.). Inert and minor structures are omitted and only major structures and sequences are included in the model.

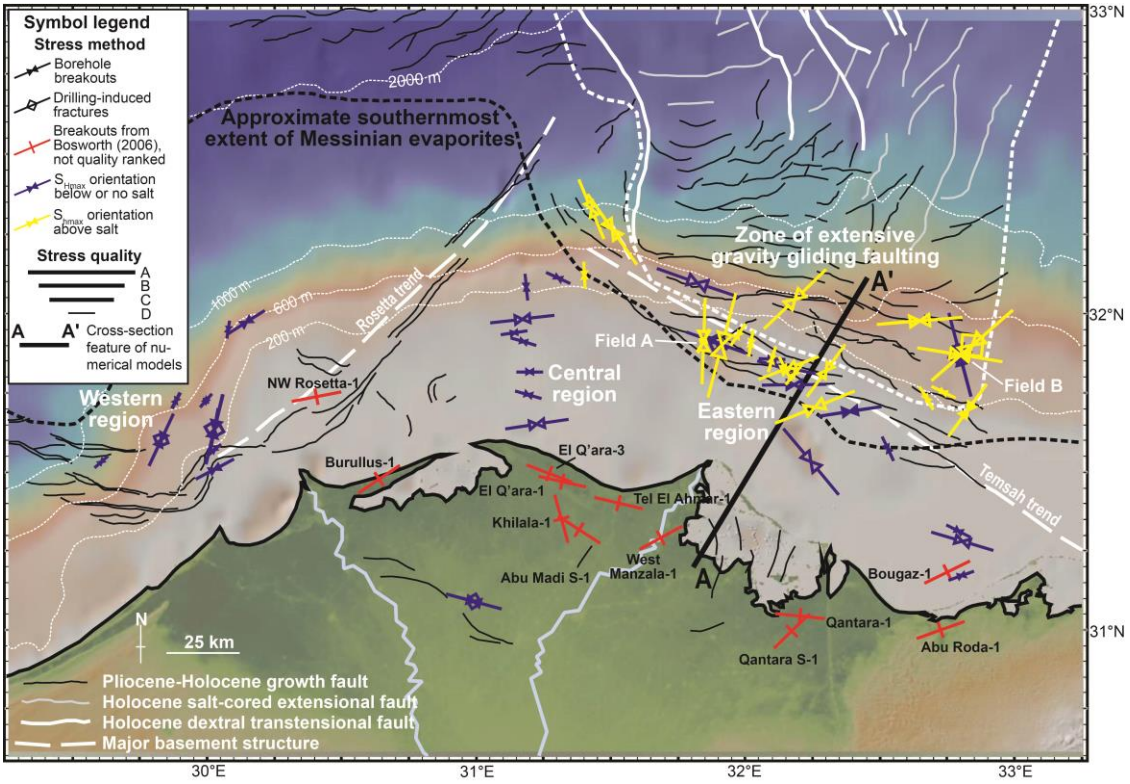

Figure 3.2. The geological map of the zone of interest of this study. Straight line A-A' represents the modeling domain of this study, which starts from the coastal line, ends up in the evaporite-bearing zone (within the white dashed line), and connects several normal supra-salt faults (grey lines). Figure components from Tingay et al., (2011); WSM database; Mascle et al., (2003); Bosworth (2006)

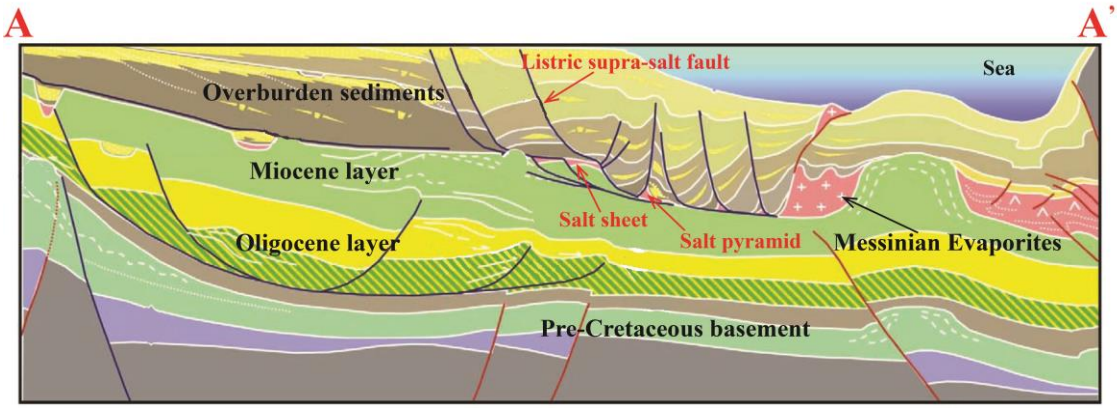

Figure 3.3. Illustration of and intersection from southwest to northeast of the Nile Delta. Geological structure types and bedding sequences. Numerical models in this study are designed based on this plot. Figure from Martin et al., (2004)

The model geometry includes several components (Figure 3.4.):

- Continental shelf with Pliocene, Miocene, and Oligocene layers (red, dark blue, and green block in Figure 3.4.)
- Pre-Cretaceous Underburden basement (grey block)
- Pleistocene-Holocene overburden layer composing the clastic wedge, which has a 5 degree dip. Four listric normal faults are included in the clastic wedge
- Messinian Evaporites are distributed below the overburden layer and above the Miocene layer. Different shapes of salt bodies are considered (Figure 3.5.):
  - Continuous and flat salt sheet (Figure3.5a.)
  - Isolated salt pillows below growth faults (Figure3.5b.)
  - Connected continuous salt sheet and salt pyramids below growth faults (Figure3.5c.)

It should be noted that the Pliocene block (red) and the sedimentary overburden blocks (light to dark yellow) are located above the Miocene layer and are dipping at a 5 degree angle, composing the deltaic clastic wedge. Salt sheets or pyramids are situated between the overburden layers and the Miocene layer and also have a 5 degree dip angle. The sedimentary blocks (Blocks 1-4; Figure 3.4a) are separated by frictional contact surfaces representing the listric growth faults. According to the Byerlee's law (Byerlee, 1978; Warren, 2004; Jaeger et al., 2006; Luo et al., 2010), the faults feature a coefficient of friction of 0.6.

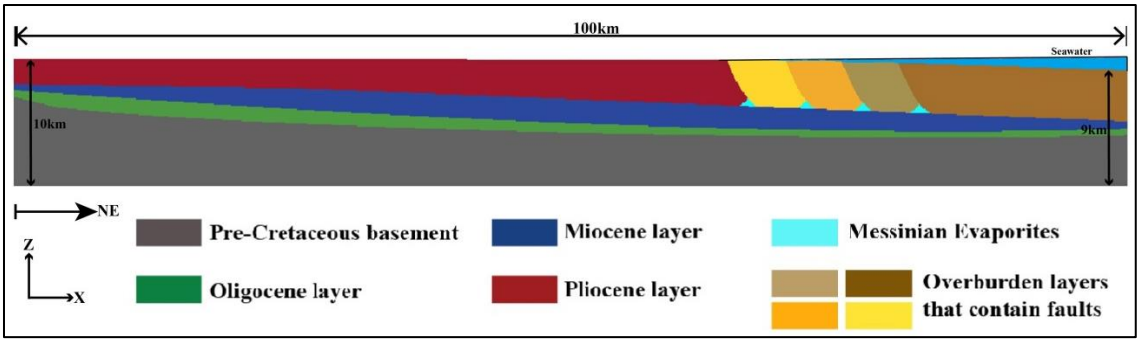

Figure 3.4. The overall model geometry of this study. It has a dimension of 100km(length)×1km(width)×10km(depth). Sea starts from the middle of the model and the sea depth at the right model boundary is 1km

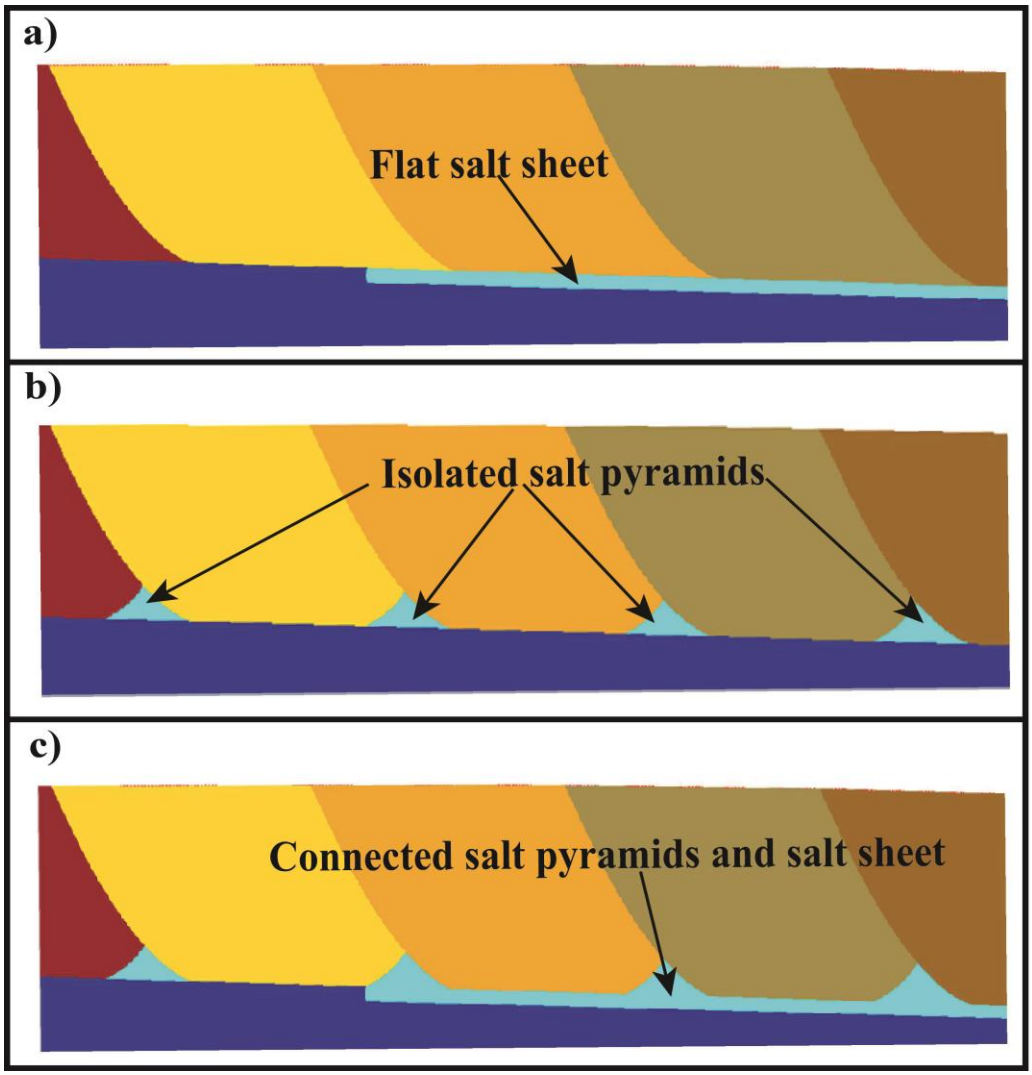

Figure 3.5. Three models with different salt bodies are tested in this study. a) a flat salt sheet is lying beneath the listric faulting group, b) salt bodies in the model shapes in four isolated salt pyramids, c) the flat salt sheet connects with three salt pyramids

Tectonic analyses conducted in this region (Badawy et al., 2004, 2014; Aal et al., 2000) only provide qualitative and approximate observations of the tectonic stress orientations and information about horizontal stress magnitudes and pore pressure magnitudes are unavailable to the public (Tingay et al., 2011). Since the major stress regime is extensional (vertical stress is the maximum principle stress) across the modeling domain (Aal et al., 2000; Badawy et al., 2004), and the isotropic horizontal stresses are observed (Tingay et al., 2011) an exemplary state of stress (SoS) is assumed with $S_h = 0.67S_V$ and $S_H = 0.75S_V$. The boundary conditions are calculated at the depth of the bottom of the overburden layer and applied to the whole model. Thus, further analysis will choose the bottom of the overburden layer as the reference depth (~4000m), where stress magnitudes are calibrated.

As stated in Chapter 3.2, the model geometry is subjected to two load steps in order to simulate the resulting state of stress. The pre-stressing load step applies displacement boundary conditions thus to achieve the exemplary state of stress (Figure 3.6 a, b.).

The second load step simulates the stress relaxation process and the possible gravitational gliding of the supra-salt sediments. This step features uni-axial strain boundary conditions, for which no lateral displacements are assigned on the model boundaries along x and y directions (Figure 3.6b.).

In a nature subsurface environment, salt bodies exist in a relaxed status (Fredrich et al., 2003; Warren, 2004; Hudec and Jackson, 2007). Thus, an approximate modeling time is determined according to the stress state within the salt body. The modeling procedure will stop when the von Mise stress magnitude within the salt body becomes lower than 1MPa (Fredrich et al., 2003). A time period of 1600 years is obtained from tests conducted in advance, which guarantees all models satisfy this requirement.

Since the spatial pore pressure distribution is unknown for the model region considered (Tingay et al., 2011), this study only considers total stresses. The possible influence of pore pressure evolution during the salt relaxation will be discussed in Chapter 5.4. Moreover, a seawater load is applied on the top of the model and will change with respect to the sea depth.

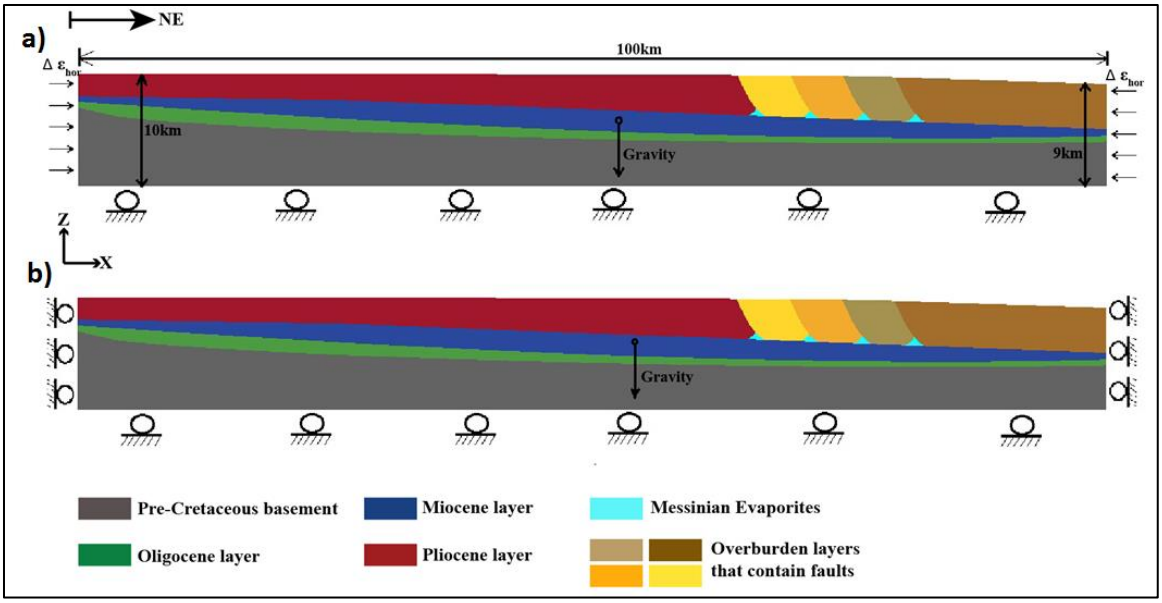

Figure 3.6. Illustration of the boundary conditions of the model and the two steps of their application. a) Prestressing step where horizontal, gravitational, and seawater loads are applied, which will result a SoS of $S_{H_{min}} = 0.67S_V$ and $S_{H_{max}} = 0.75S_V$. b) Second load step, where only gravitational and seawater loads are applied

3.5. MATERIAL PROPERTIES

Abaqus™ offers a general material library that contains constitutive equations for different mechanical responses (Hibbit et al., 2001). This study relies on the capacity of Abaqus™ to define elastic and visco-elastic materials and conduct a time-dependent analysis for a time period of 1600 years. Material behavior is defined by the following parameters: 1) density, 2) Young's modulus (E), 3) Poisson's ratio (v), 4) viscosity. Since the detailed material properties of the rocks from the Nile Delta are unknown, exemplary values from the literature (Schultz-Ela and Jackson, 1993; Luo et al., 2010; Nikolinako et al., 2011; Tuitt et al., 2014) are chosen, as shown in Table 3.1.

Luo et al., (2010) and Nikolinako et al., (2011) studied the influence of a semi-cylindrical salt body to the surrounding rock matrix. In their studies, the salt body is defined as a Maxwell viscoelastic material and simulated in Abaqus™. Similarities are also found considering the setting of the salt body, including the burial depth, overburden stress magnitude, and the neglect of temperature and pore pressure. As a result, the

mechanical property parameters of the salt body are adopted from the studies of Luo et al. (2010) and Nikolinako et al. (2011) (Table 3.1, 3.2.).

Table 3.1. The elastic parameters assigned on different sediment components

Component	**Density**	**Young's Modulus**	**Poisson's Ratio**
Supra-salt sediments	2300 kg/m^3	20 GPa	0.25
Pliocene layer	2500 kg/m^3	40 GPa	0.25
Miocene layer	2600 kg/m^3	40 GPa	0.25
Oligocene layer	2600 kg/m^3	40 GPa	0.25
Pre-Cretaceous layer	2600 kg/m^3	40 GPa	0.25

Table 3.2. Viscoelastic parameters of salt body (Luo et al., 2010; Nikolinako et al., 2011)

Parameter	**Value**
Density (ρ)	2000 kg/m^3
Young's Modulus (E)	30 GPa
Poisson's ratio (v)	0.25
Viscosity (μ)	10^{18} Pa·s

In the finite-element simulator of Abaqus^{TM}, the elastic behavior is activated by the keyword *ELASTIC and the elastic material property matrix [D] in Equation 27 can be defined by defining Young's modulus and Poisson's ratio inputs. The visco-elastic behavior is activated by the keyword *CREEP. According to the relationship between the strain rate, time and strain obtained from laboratory studies (Rybacki et al., 2008; Chen et al., 2005; Zavada et al., 2015), the power law creep presented in Equation 28 can be transformed and used in its "time hardening " form or in its "strain hardening" form. The

strain hardening form calculates the strain rate as a function of strain, which fits the behavior of salt rock. The equation of strain hardening form can be written as (Hibbitt et al., 2011):

$$\dot{\varepsilon}^{cr} = (A\tilde{q}^{n}[(m+1)\bar{\varepsilon}^{cr}])^{\frac{1}{m+1}} \tag{40}$$

Where $\dot{\varepsilon}^{cr}$ is the uniaxial equivalent creep strain rate, defined as $\dot{\varepsilon}^{cr} = \sqrt{\frac{2}{3}\dot{\varepsilon}^{cr} : \dot{\varepsilon}^{cr}}$; $\tilde{q}$ is the uniaxial equivalent deviatoric stress; $\bar{\varepsilon}^{cr}$ is the equivalent creep strain; A, n, and m are related to temperature: A=$\frac{1}{3\mu}$ in a 3D scenario, where μ is the dynamic viscosity of the salt; n and m can be obtained by lab strain tests. The magnitudes of μ, n, and m are shown in the Table 3.1.

4. RESULT

In this chapter, all modeling results will be described in the following context for each salt geometry: spatial distribution of principal stress orientations; deformation and displacement of each component; the movement of supra-salt listric faults. Figure 4.1 shows the zone of interest in the model, where stress reorientations are expected.

In most regions below the depth of 2000m, where the major model features are located, the vertical stress (S_V) is the maximum principal stress (σ_1). Thus, the intermediate principal stress (σ_2) and the minimum principal stress (σ_3) can be used to represent the horizontal stresses in zones of interest. As introduced in the model setup section, the pre-defined stress field features margin-normal maximum horizontal stress (S_H) and margin-parallel minimum horizontal stress (S_h), which are shown by σ_2 and σ_3, respectively. As a result, the reorientation of σ_2 and σ_3 directions is an important indicator of structural movement that needs to be remarked in this study.

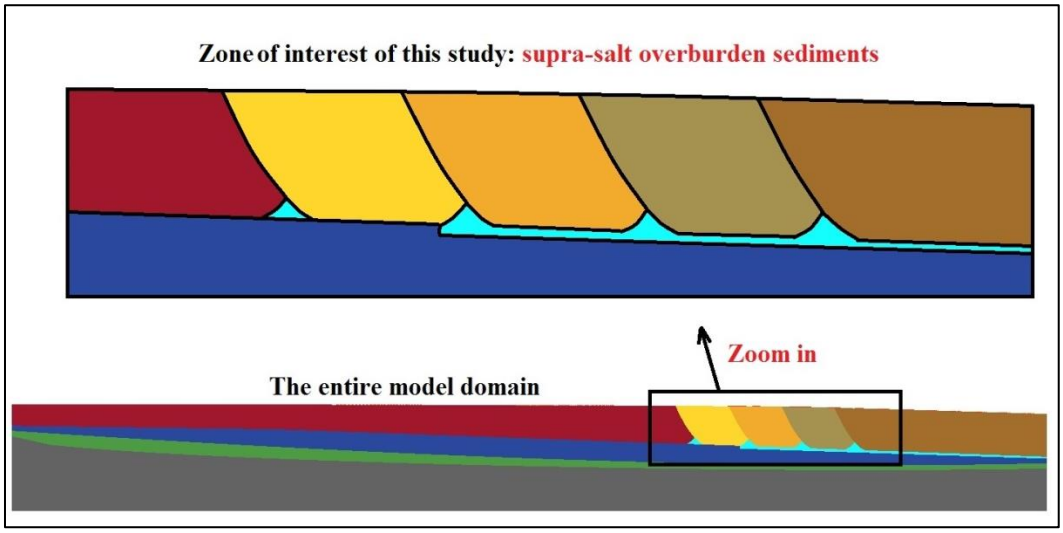

Figure 4.1. Illustration the zone of interest within the entire model domain. Supra-salt sediments contain listric supra-salt faults, which are the key features of this study

4.1. PRESTRESS MODEL

The pre-stress models are characterized with all boundary conditions and loads as introduced in chapter 3.3. Only a single analysis step ignoring all time-dependent

properties is performed, which means the salt body is processed as an elastic material. Thus, gravitational gliding of listric faults within pure elastic sediments is simulated, which represents a scenario where the model is gravitationally gliding without the influence of the salt body. Figure 4.2 shows the intermediate principal stress and the minimum principal stress orientations in different parts of the model domain. Margin-parallel S_H are observed in most of the model domain below 2000m depth except 2000-meters-long left-most part of the model, where S_H are oriented margin-normal. This observation perfectly coincides with the stress field predicted by the classic deltaic model shown in Figure 1.8 (Tingay et al., 2012).

4.2. FLAT SALT SHEET

Figure 4.2a shows the resultant displacement vector and magnitude within the supra-salt overburden sediments. Block 2, 3, and 4 display obvious downward and rightward displacements, on average, 1.3m, 2.2m, and 3.1m respectively. The resultant displacement in Block 1 is directed towards the delta shelf region. Figure 4.2 b only shows the displacement component along x-axis. It clearly shows that the Block 1 moves in the opposite direction than the other blocks. It also can be noticed from Figure 4.2 a, b that the displacement direction above and below the salt sheet (area within the black frame) is opposite (Figure 4.3.). Unlike for Block 2, 3, and 4, sequences below the salt layer tend to move leftwards. This provides the first evidence that the flat salt sheet detaches the material movement above and below.

Figure 4.4 shows the tangential slip between the two adjacent blocks. An increasing maximum movement of slip can been noticed from fault 1 to 4: 0.1m, 0.6m, 0.9m, and 1.2m. Fault 1 has the smallest displacement among the four faults. For fault 2 to 4, underlain by the salt sheet, the amount of gliding is more significant. In addition, the relative movement of the four faults stops immediately as the fault plane reaches the salt sheet and the contact surfaces have no movement on the salt sheet. It should be noted that Block 1 directly contacts with the Miocene layer, as a result, Block 1 is able to slide at the bottom.

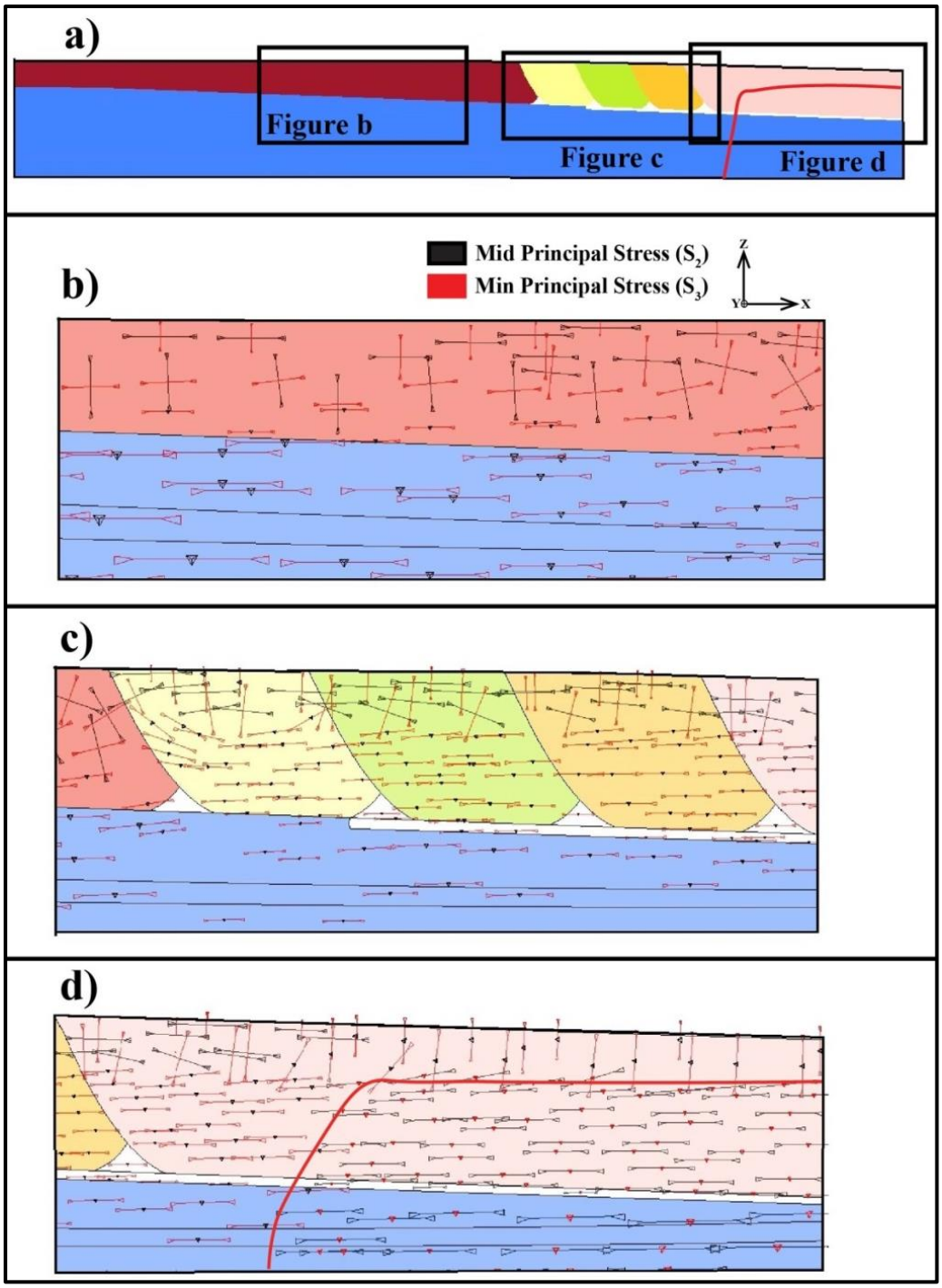

Figure 4.2. Illustration of principal stress orientations of the pre-stressing model. a) Model geometry of the continuous salt sheet and pyramids model which contains zones of interest. This model is selected as the example to illustrate the resulting stress field by the pre-stressing step; b) Margin-parallel S_H distributes in the delta shelf; c) Margin-parallel S_H is observed in both the supra-salt overburden blocks and sub-salt sediments, a margin-normal S_H zone is annotated; d) S_H is margin-normal in supra-salt overburden Block 4 and margin-parallel in sub-salt sediments

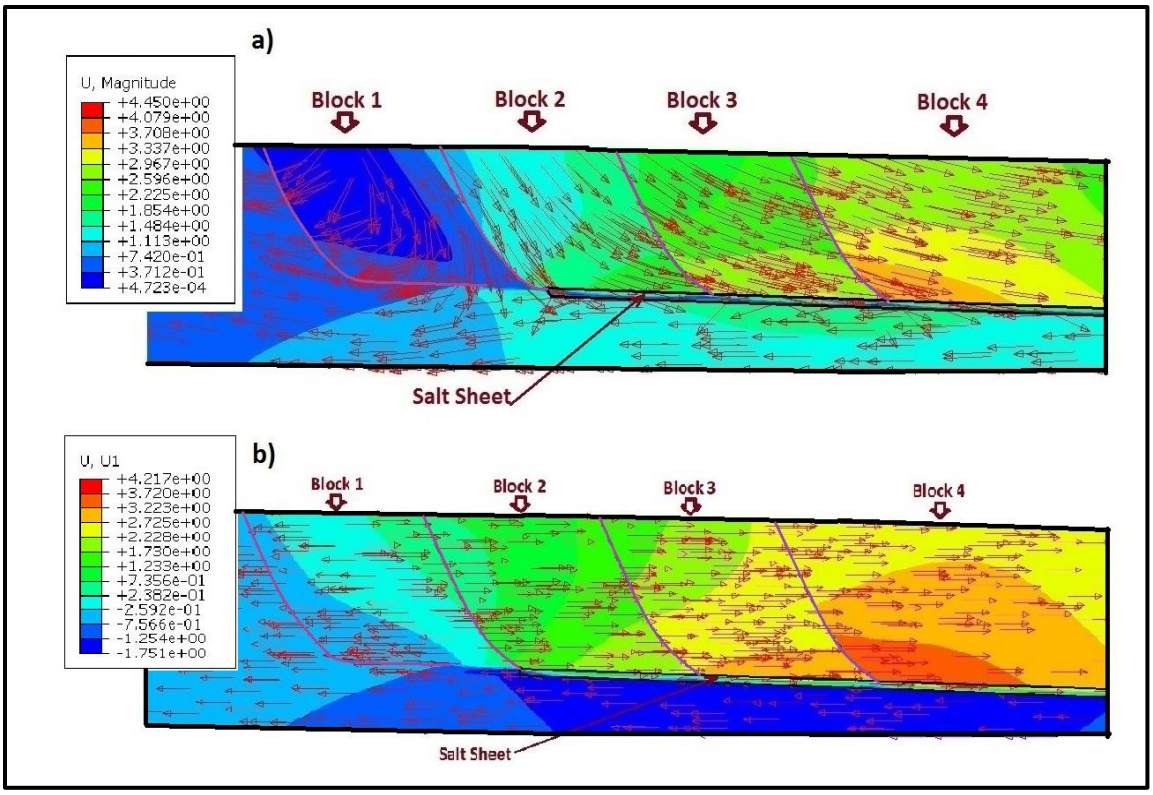

Figure 4.3. The displacement vector and magnitude of supra-salt sediments in the model featuring a flat salt sheet. a) The overall resultant displacement, b) The displacement component along x-axis. Opposite displacement directions are presented above and below the salt sheet

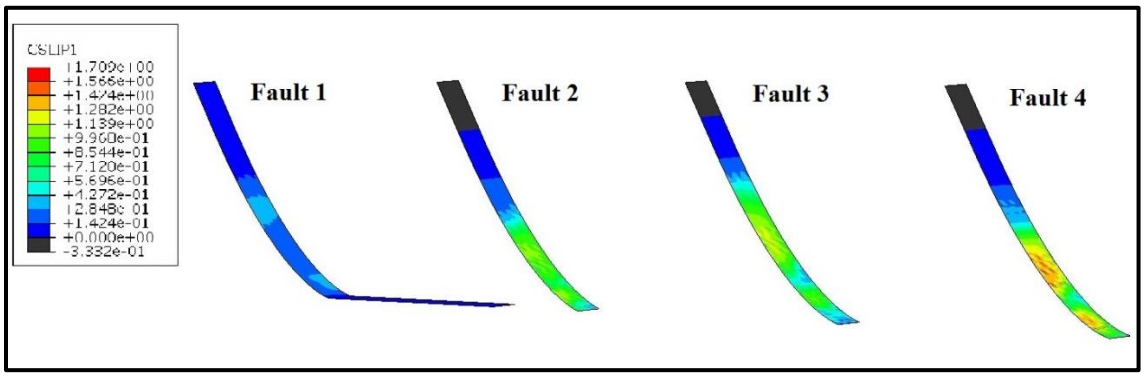

Figure 4.4. The tangential displacement on the planes of the four supra-salt listric faults in the model featuring a flat salt sheet. The color contour shows the x-direction displacement magnitude

Figure 4.5a, b, c, and d illustrate the orientation of the maximum principal stress (σ_1), the intermediate principal stress (σ_2), and the minimum principal stress (σ_3) within the supra-salt sediment blocks, the flat salt sheet, and the Miocene layer below the salt sheet. In the shallow part of the clastic wedge (depth from 0-1500m), σ_1 and σ_2 are oriented in the horizontal direction and σ_3 acts along the vertical direction as the vertical stress (S_V). It is shown that S_H (margin-parallel) > S_h (margin-normal) > S_V (vertical), which is a compressional stress regime.

As shown in the Figure 4.5b, the stress field in the delta shelf generally coincides with the classic delta model: maximum horizontal stress directs in margin-parallel and minimum horizontal stress orients in margin-normal.

For greater depths (1500-4000m), S_V gradually becomes σ_1, the two horizontal stresses turn into σ_2 and σ_3. It is shown that S_V (vertical)>S_H (margin-parallel) >S_h (margin-normal), which is an extensional stress regime. For regions near the end of the four faults, a 90 degrees rotation of S_H and S_h are observed, whereby S_H becomes margin-normal and S_h becomes margin-normal (red insets in Figure 4.5d).

Below the salt sheet, in the Miocene, Oligocene, and the Pre-Cretaceous layers, σ_1 is S_V, σ_2 has a margin-parallel orientation which is the same as in the salt sheet and overburden blocks, and σ_3 has a margin-normal orientation, which is also the same as in the overburden blocks.

There are two major stress reorientation zones in the model domain. As shown in Figure 4.5c, a region with margin-normal S_2 is observed in the Miocene layer, very close to the left edge of the flat salt sheet. A remarkable displacement difference between the salt sheet and the nearby Miocene sediments can also be observed in Figure 4.3b (red insets): the salt sheet tends to move leftwards for 1m but the Miocene sediments almost have no displacement. As shown in Figure 4.5d (red insets), a large margin-normal S_H dominated region occurs in Block 4, which starts from the end of fault to the right end of the model. Correspondingly, prominent down-slope displacement also happens in this region.

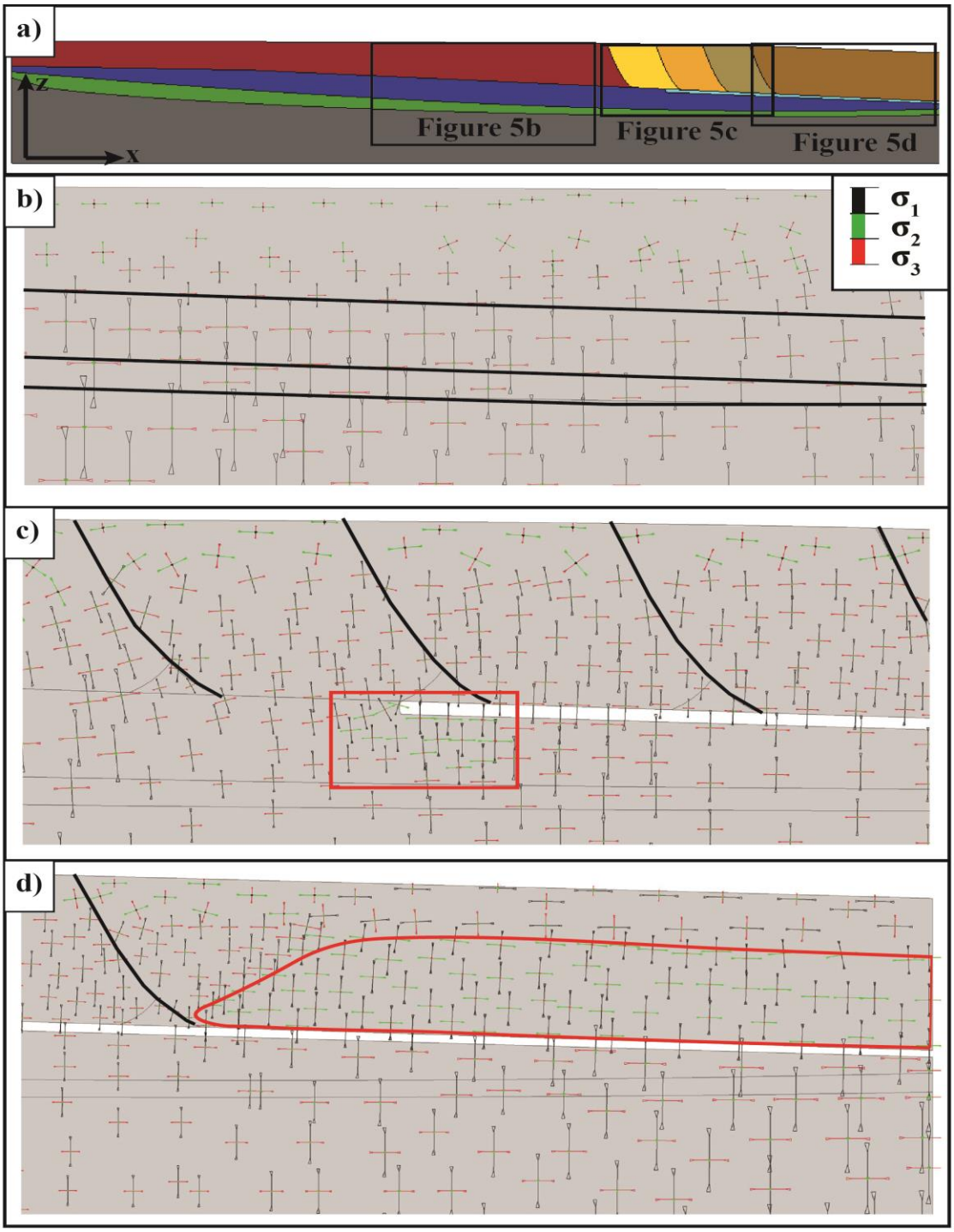

Figure 4.5. Illustration of principal stress orientations in the model featuring a flat salt sheet. a) Illustration of locations of each zone of interest in the model domain; b) Margin-parallel S_H in the delta shelf, which coincides with the classic model; c) Margin-parallel S_H is observed in both the supra-salt overburden blocks and sub-salt sediments, a margin-normal S_H zone is observed at the left edge of the salt sheet (red inset); d) S_H is margin-normal in supra-salt overburden Block 4 (red inset) and margin-parallel in sub-salt sediments. A clear separation of supra-salt and sub-salt S_H orientation is presented

4.3. ISOLATED SALT PYRAMIDS

The magnitude (color contour) and direction (vectors) of the displacement field in the supra-salt overburden sediments are illustrated in Figure 4.6a (resultant) and 4.6b (x-component). Besides the downward displacement of all components, the fourth fault becomes the boundary of separating the opposite moving directions: Block1, Block 2, and Block 3 have obvious leftward (towards the delta shelf) displacement (on average, 0.3m, 0.25m, and 0.2m, respectively); Block 4 tends to move rightwards (towards the delta toe) (0.4m). On the left and right side of each salt pyramid, rightwards and leftwards displacements are observed in the overburden blocks. This opposite movement becomes increasingly obvious for salt pyramids from left to right. In addition, unlike for the model featuring the flat salt sheet, a consistent moving tendency of the supra-salt overburden sediments and the Miocene layer below is observed on this model (Figure 4.6b.). The salt bodies in this model do not detach the general moving directions between overburden sediment blocks and the Miocene base layer.

Figure 4.7 presents the tangential slip of the four supra-salt faults. Displacement magnitudes increase from Fault 1 to Fault 4. Fault 1 has an average sliding of 0.35m, Fault 2 has 0.5m, Fault 3 has 0.8m, and Fault 4 has 1m. Like the model featuring the salt sheet, all four faults stop sliding at the point, where the fault planes touch the salt pyramids. Before this point, the gliding magnitude reaches the maximum.

Figure 4.8a shows the entire model domain that contains the isolated salt pyramids. As shown in Figure 4.8b, the stress field in the delta shelf generally coincides with the classic delta model: the maximum horizontal stress is in margin-parallel and minimum horizontal stress is margin-normal.

Figure 4.8c shows the orientations of the three principal stress components in the interest zone, respectively. For all regions above 1500m, the maximum principal stress (σ_1) is oriented either in margin-parallel direction or in margin-normal direction and the vertical stress (S_V) is always the minimum principal stress (σ_3). At greater depth (1500-3000m), Sv becomes σ_1. The maximum horizontal stress (S_H) appears to be margin-parallel and the minimum horizontal stress (S_h) appears to be margin-normal. However, at the bottom of the four blocks, the two horizontal stress orientations rotate 90 degrees; S_H becomes margin-normal and S_h becomes margin-parallel. This rotation occurs most

remarkably in the middle of each block bottom, which coincides with the region featuring enhanced displacement.

In the Miocene layer below the overburden sediments and salt pyramids, the three principal stress orientations are similar to orientations at depth of 3000-4500m: σ_1 is vertical; S_H is margin-parallel; S_h is margin-normal (Figure 4.8c.). There is an apparent 90 degrees rotation of S_H observed in sequences above and below the four salt pyramids. In addition, although the S_H orientations in the right part of the model are oriented margin-normal (Figure 4.8d.), no detaching movement is observed between supra-salt and sub-salt sediments (Figure 4.6a.).

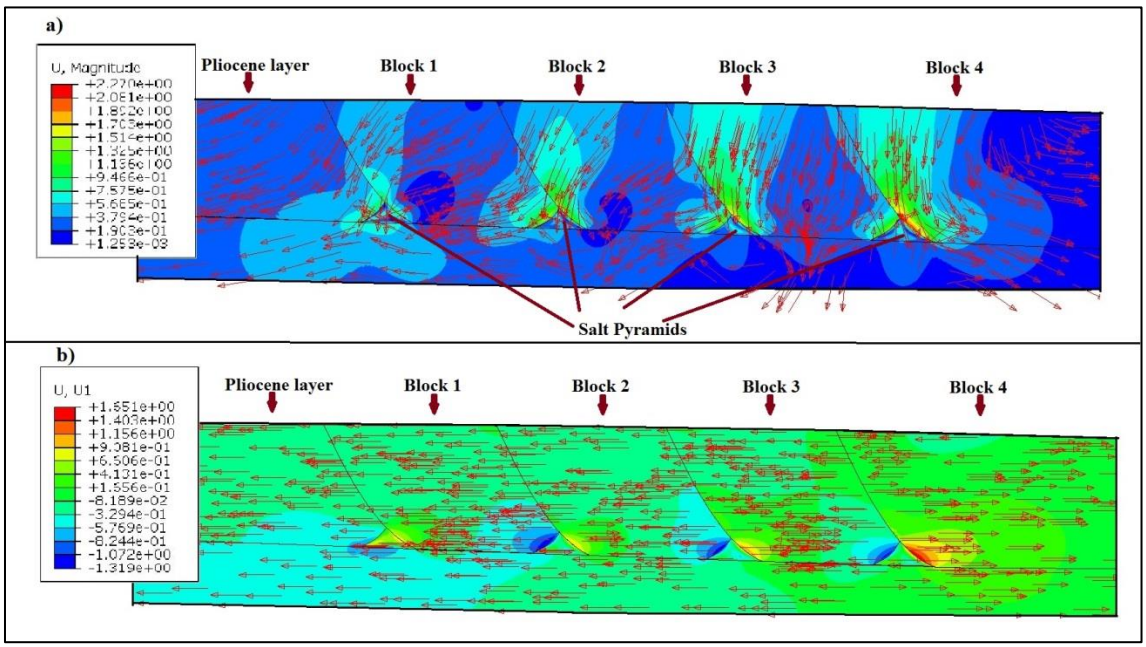

Figure 4.6. The displacement vector and magnitude of supra-salt sediments in the model featuring isolated salt pyramids. a) Overall resultant displacement, b) Displacement component along x-axis. No opposite moving is observed above and below the salt body

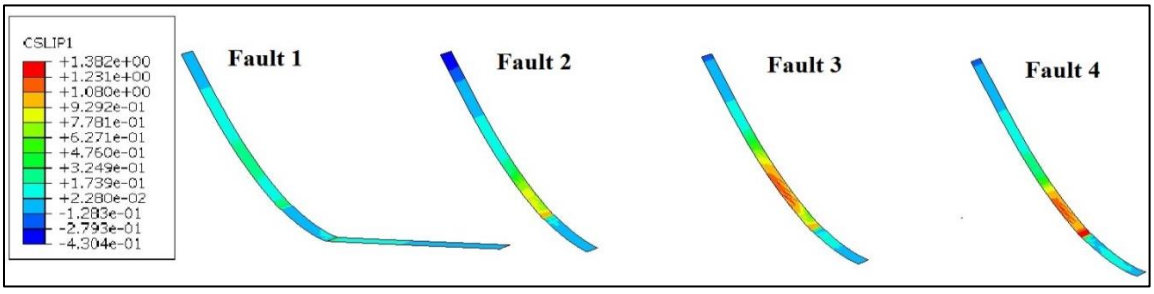

Figure 4.7. The tangential slip on the four fault planes in the model featuring isolated salt pyramids. The color contour represents the magnitude of displacement along x-direction

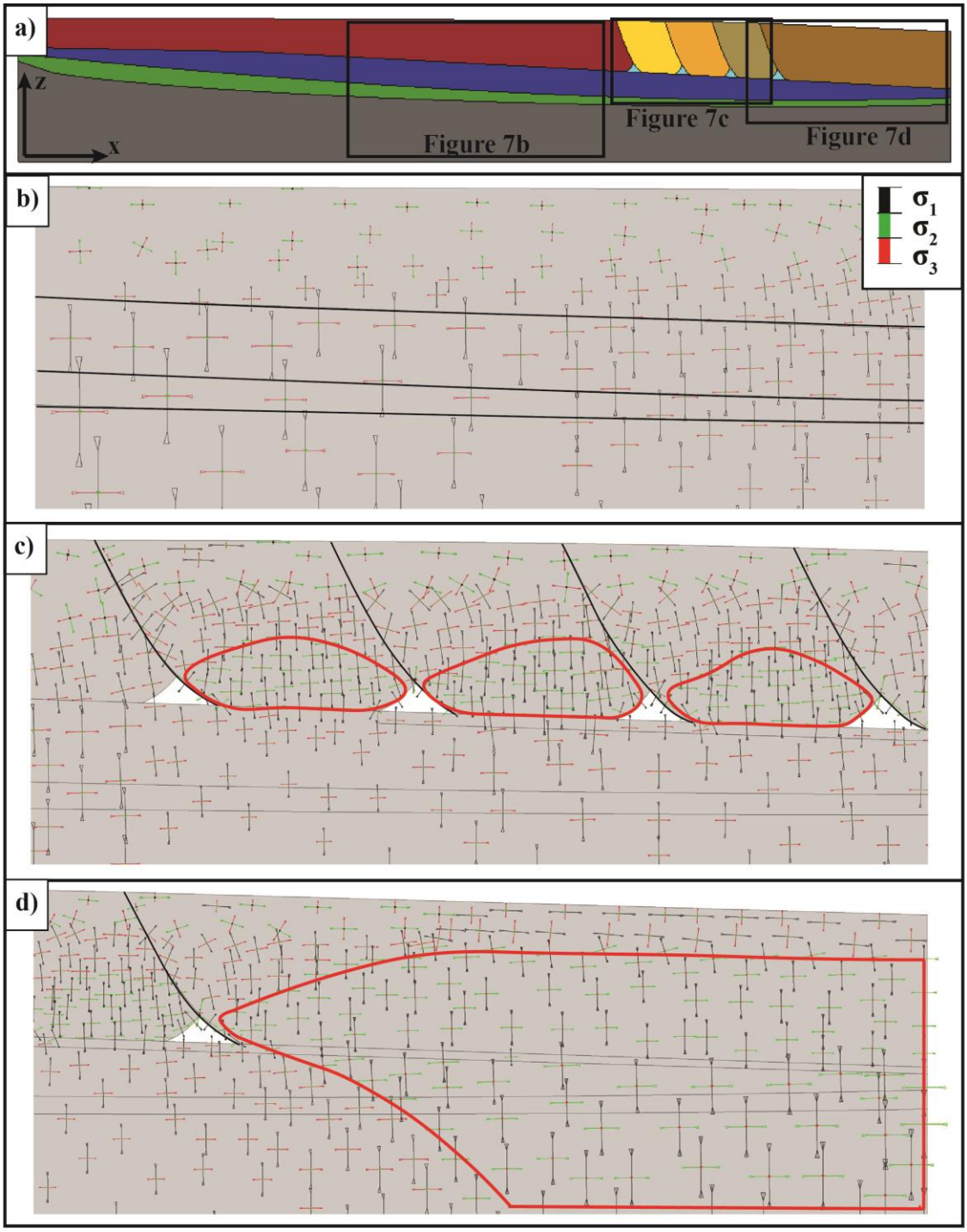

Figure 4.8. Illustration of principal stress orientations in the model featuring isolated salt pyramids a) Illustration of locations of each zone of interest in the model domain; b) Margin-parallel S_H distributes in the delta shelf, which coincides with classic deltaic model prediction; c) Margin-parallel S_H is observed in both the supra-salt overburden blocks and in sub-salt sediments, margin-normal S_H zones are observed in regions between salt pyramids, which are annotated by red insets; d) S_H is margin-normal in supra-salt overburden Block 4 (red inset)

4.4. CONNECTED FLAT SALT SHEET AND SALT PYRAMIDS

Figure 4.9 demonstrates the resultant and x-component displacement in the zone of interest, for which magnitude and direction are given by the color contour and vectors. The Pliocene layer and the left part of Block 1 are moving towards the delta shelf. Block 2, 3, and 4 are gliding towards the delta toe, at an average magnitude of 1.5m, 4.3m, and 6m along x-axis. It is clear to observe that the continuous salt sheet and pyramids detaches the displacement of the layer above and below: Block 2, 3, and 4 are moving in the opposite direction than the Miocene base layer.

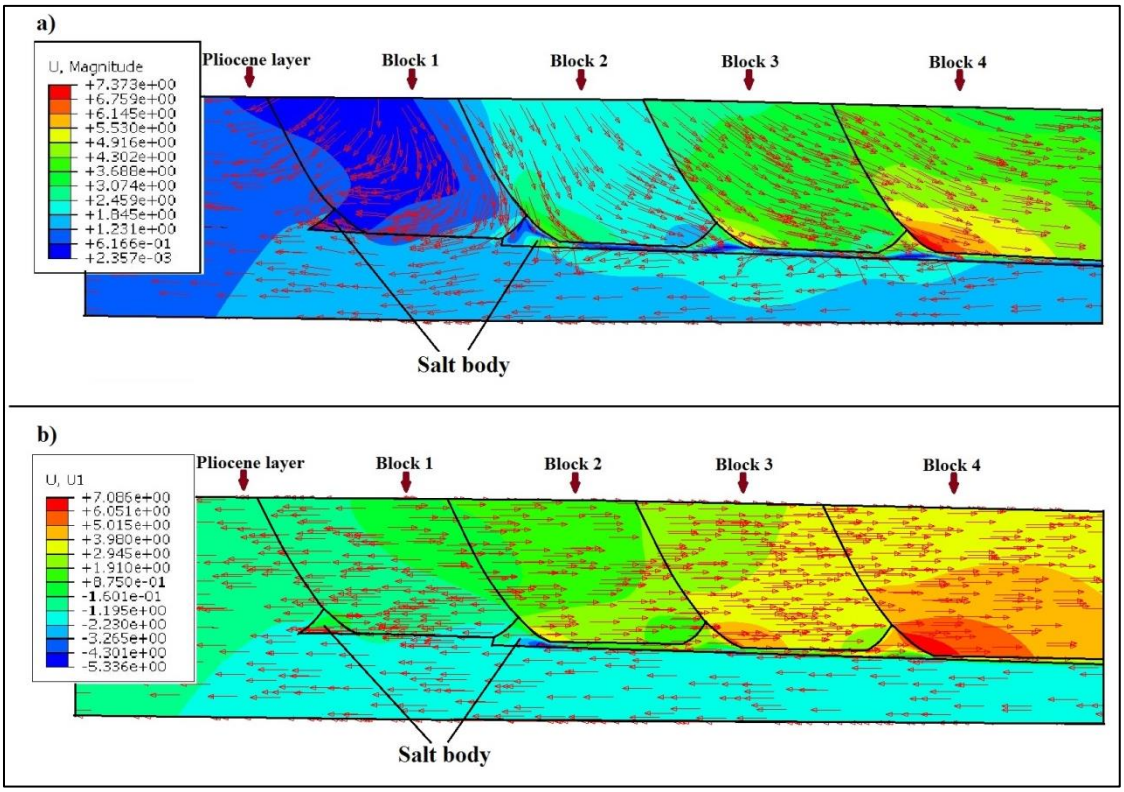

Figure 4.9. The distribution of displacement vector and magnitude in the model featuring continuous salt sheet and pyramids. a) The resultant displacement in the supra-salt sediments. b) The displacement component along x-axis in the supra-salt sediments. The continuous salt layer detaches the displacement direction of sediments above and below

Figure 4.10 shows the gliding magnitude of the four faults, the color contour shows the positive displacement along x-axis. The amount of gliding for Fault 1 is very small (0.5m at the bottom of the fault), for Fault 2, 3, and 4 are much larger and close in

magnitude (2.7m, 2.5m and 2.6m at the bottom of each fault). Same as for the previous models, the gliding of the faults stops, when the fault plane reaches the salt body.

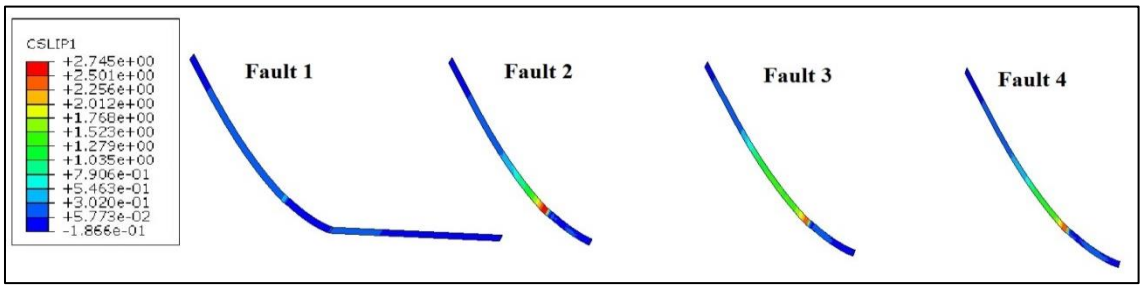

Figure 4.10. The gliding magnitude of four faults in the model featuring continuous salt sheet and pyramids. The color contour represents the positive displacement along the x-direction

The three principal stress orientations for the zones of interest in the model are shown in Figure 4.11a, b, c, and d. For the all regions with a depth smaller than 1000m, the vertical stress (S_V) is the minimum principal stress.

In the central part of blocks 1-4 (between 1500m and 3500m, S_V becomes σ_1, the margin-parallel stress decreases to become σ_2, and σ_3 becomes margin-normal.

Between 3500m and the top of the salt bodies (including the salt pyramids and flat salt sheet), a 90 degrees rotation of the horizontal stresses can be observed in Block 1-3. The intermediate principal stress becomes margin-normal and the minimum principal stress turns margin-parallel. This rotation is more obvious in Block 2-3 above the salt sheet and between the two adjacent salt pyramids (red frames in Figure 4.11c).

Below the salt bodies and overburden sediments, the horizontal stress orientations rotate 90 degrees again with respect to the bottom of Block 1-3. S_V remains σ_1, but the margin-parallel horizontal stress turns to be σ_2, and the margin-normal horizontal stress becomes σ_3.

In Block 4, S_2 is margin-normal in the middle and lower part of the block (Figure 4.11d.). For this part drastic down-slope displacement is also observed (Figure 4.9a.).

A general margin-parallel σ_2 orientation is observed in the delta shelf and base layers (Figure 4.11b, d.). Obvious detachments of both displacement direction and S_H orientation can be distinguished above and below the salt body.

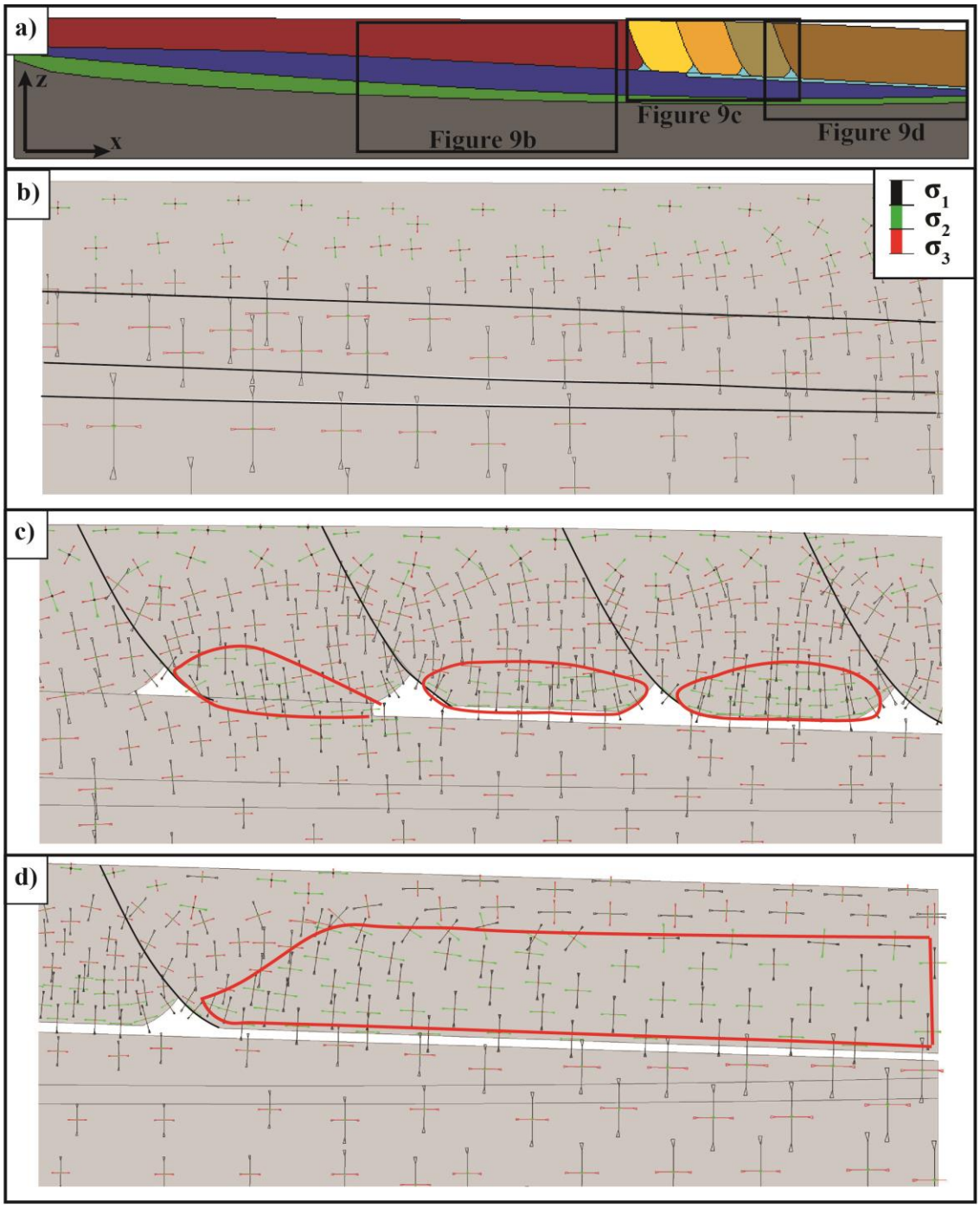

Figure 4.11. Illustration of principal stress orientations in the model featuring continuous salt sheet and pyramids. a) illustration of locations of each zone of interest in the model domain; b) Margin-parallel S_H distributes in the delta shelf, which coincides with the classic deltaic model; c) Margin-parallel S_H is observed in both the supra-salt overburden blocks and in sub-salt sediments, margin-normal S_H zones are observed at the edge of the salt sheet and between salt pyramids, which are annotated by red insets; d) S_H is margin-normal in supra-salt overburden Block 4 and margin-parallel in sub-salt sediments. A clear separation of supra-salt and sub-salt S_H orientation is presented

4.5. DIFFERENT FRICTION COEFFICIENTS

In order to test the influence of the magnitude of the gravitational gliding process, three different friction coefficients, 0.6, 0.4, and 0.2 respectively, are assigned to the fault surfaces of the model featuring the connected salt sheet and pyramids. All other parameters remain unchanged and all boundary conditions and loads are same as for the base model.

Figure 4.12 shows the resultant displacement magnitude (shown by the color contour) and x-component direction vector in the interest zone of three models for the different friction coefficients. From Figure 4.12 a, b and c, it can be observed that a decreasing of friction coefficient is able to enhance the displacement of the supra-salt sediments. Each 0.2 decrease from 0.6 to 0.2 can lead to 13.5% more displacement, on average. However, the change of friction coefficients does not affect the opposite moving directions of supra-salt overburden sediments. Also the intermediate principal stress orientations in the three models are not influenced by different friction coefficients (Figure 4.13 a, b, and c.).

4.6. DIFFERENT SALT VISCOSITIES

Three different viscosities are assigned to the salt bodies for the model featuring the connected salt sheet and pyramids. The base case has a viscosity of 10^{18} Pa·s; viscosities of 5×10^{17} Pa·s and 2×10^{18} Pa·s are tested for comparison. All other parameters are unchanged and the simulating time is still 1600 years which is able to guarantee that the salt bodies with different viscosities are fully relaxed, i.e. von Mise stress <1MPa.

Figure 4.14 a, b, c, and d show the resulting total displacement magnitude (shown by the color contour) and the displacement vector along x-axis. There is almost no difference observed between the three models. Both displacement magnitude and direction are the same in the three models. 4.15 a, b, and c shows the resulting intermediate principal stress (σ_2) magnitude and orientations. Like the resulting displacement, the σ_2 magnitude and orientations are also unchanged among the three models with different viscosities (Figure 4.15.).

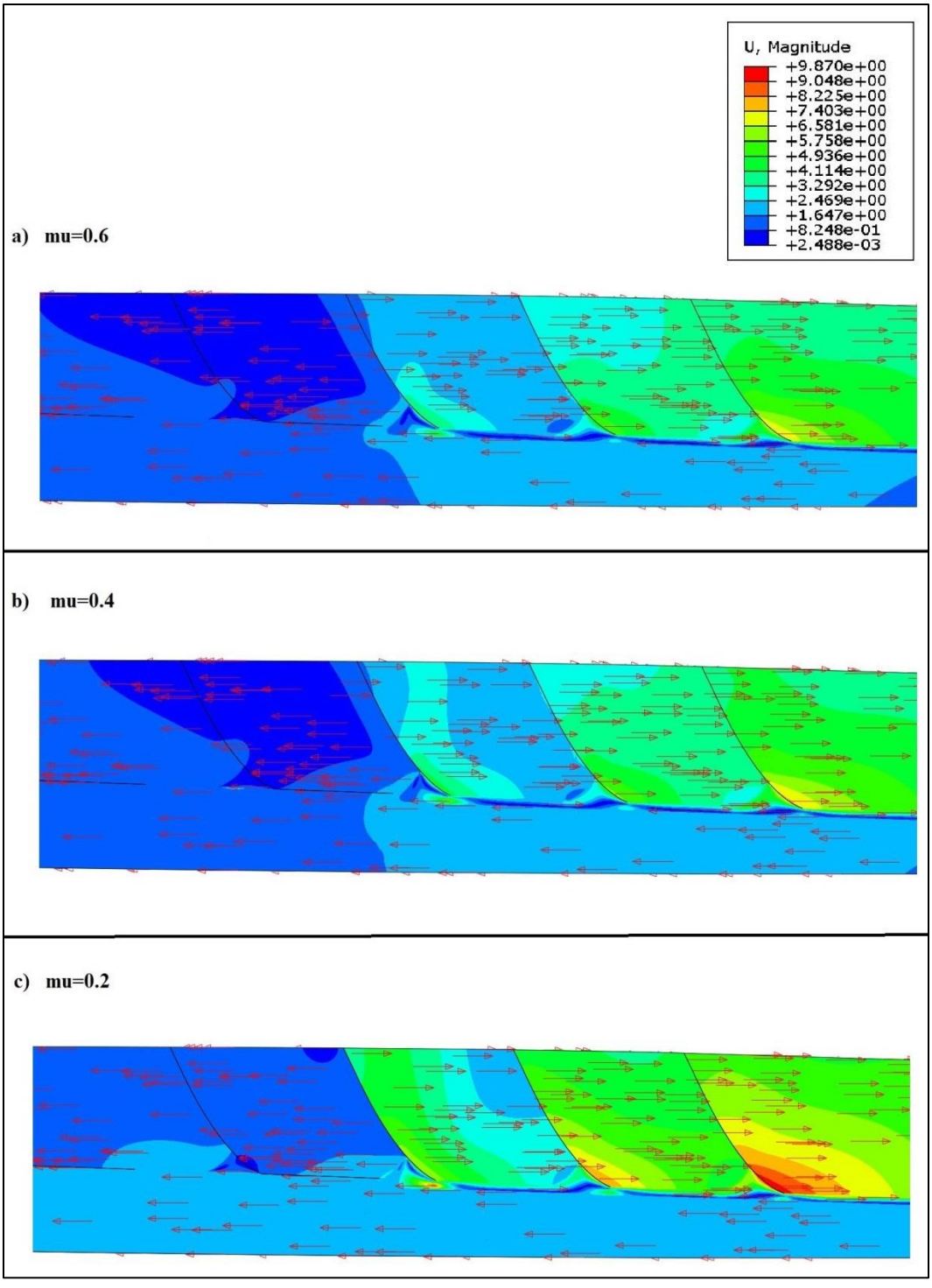

Figure 4.12. The resulting displacement for different friction coefficients. The model featuring the continuous salt sheet and pyramids is selected as the example. The color contour represents the magnitude of resultant displacement (increasing along positive x-axis and z-axis). The arrows represent the displacement along x-axis. A remarkable increasing of displacement is observed when mu becomes small

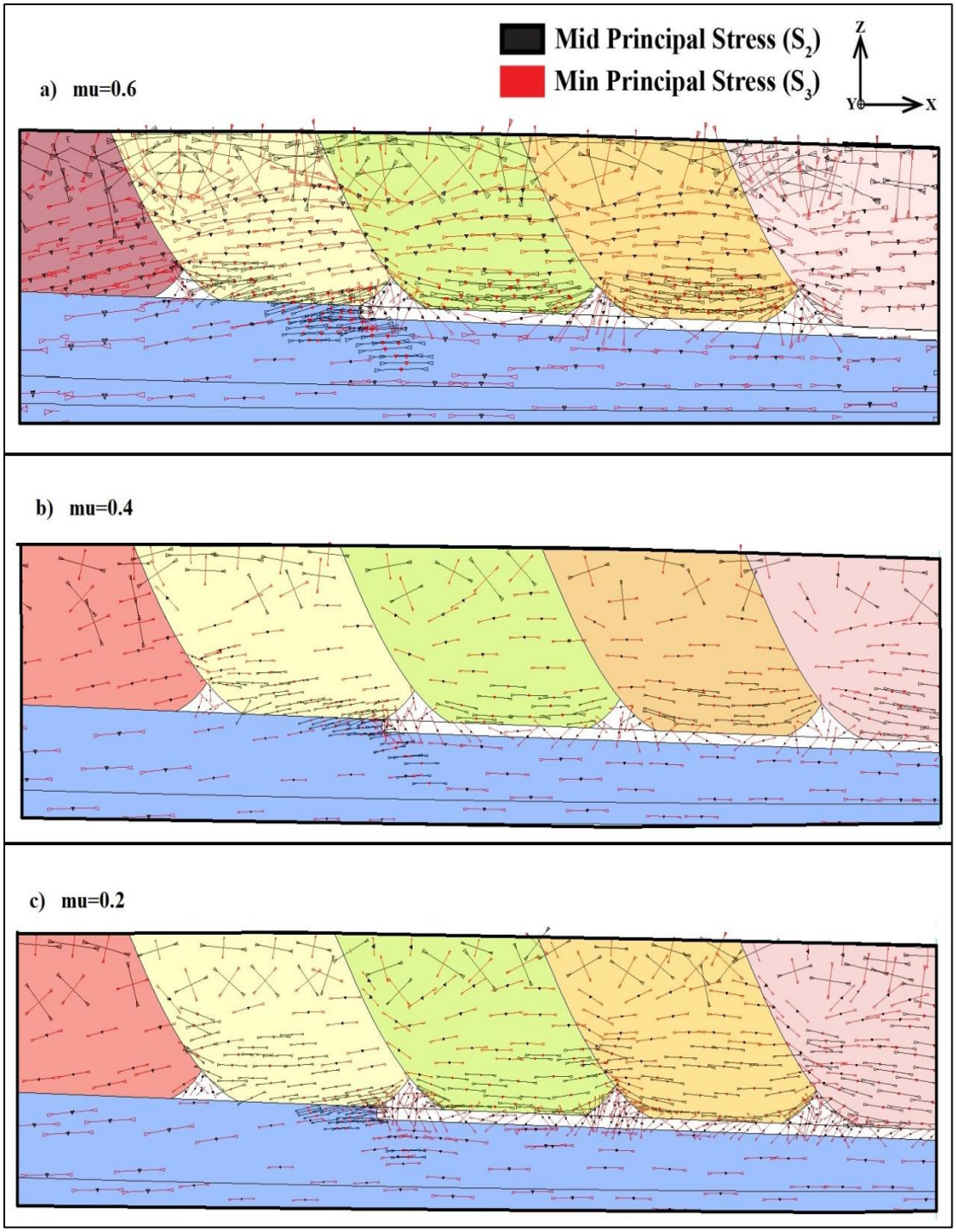

Figure 4.13. The Intermediate principal stress distribution in models with three different friction coefficients. The model featuring the continuous salt sheet and pyramids is selected as the example. a) Friction coefficient is 0.6, which is also the base case. b) Friction coefficient is 0.4. c) Friction coefficient is 0.2. An increasing of margin-normal S_H zones is observed when mu decreases

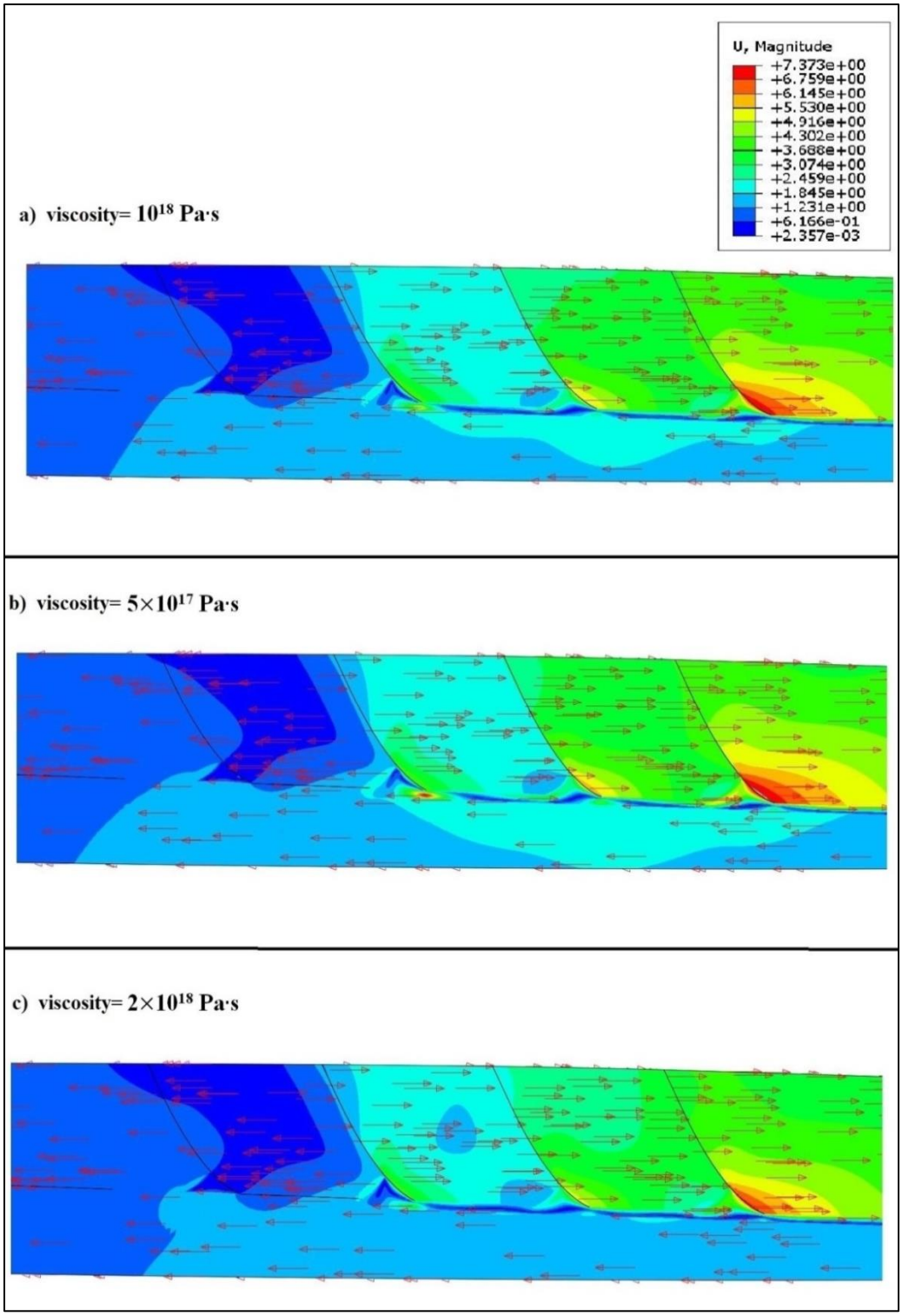

Figure 4.14. The resulting displacement of different viscosities. The model featuring the continuous salt sheet and pyramids is selected as the example. The color contour represents the magnitude of resultant displacement (increasing along positive x-axis and z-axis). The arrows represent the displacement along x-axis. Almost same magnitude of displacement is observed in the three models

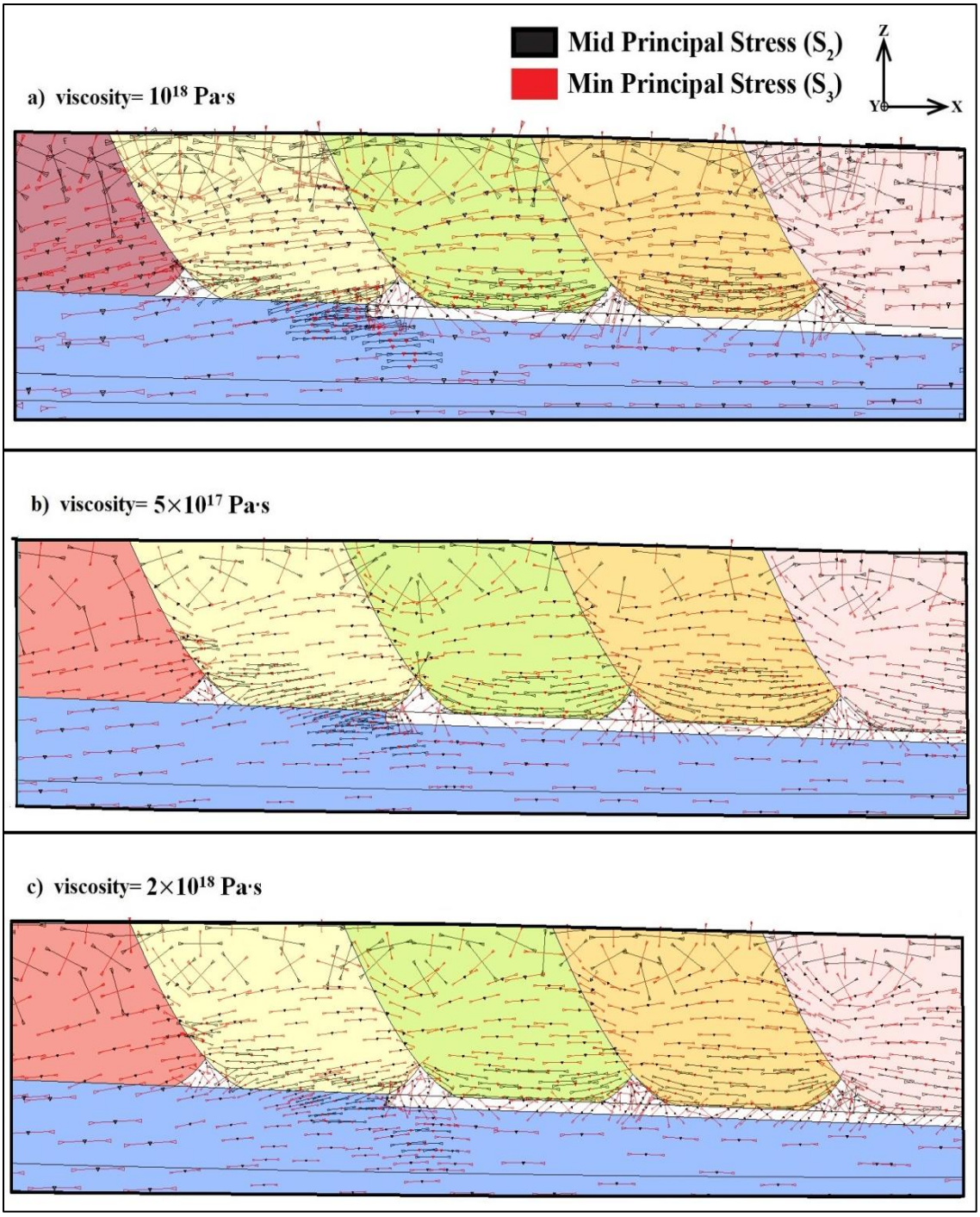

Figure 4.15. The Intermediate principal stress distribution in models with three different viscosities. The model featuring the continuous salt sheet and pyramids is selected as the example. a) Viscosity of the salt body is 10^{18} Pa·s, which is also the base case. b) Viscosity of the salt body is 5×10^{17} Pa·s. c) Viscosity of the salt body is 2×10^{18} Pa·s. An increasing of margin-normal S_H zones is observed when mu decreases

5. DISCUSSION

Various numerical modeling studies (Fredrich et al., 2003; King et al., 2012; Nikolinakou et al., 2012) have shown that salt relaxation is able to affect the state of stress in adjacent regions. In this study, 3D finite-element analysis has been used to simulate different scenarios of the gravitational gliding of supra-salt faults in the Nile Delta. Sensitivity analysis accounting for different shapes of the salt body, frictional behavior of the fault properties, and the rheology of the salt body are investigated. The opposite displacement directions and the rotation of stress orientations above and below the salt body provide additional quantitative support that salt acts as mechanical detachment zone. In this chapter different models will be analyzed and evaluated with respect to the two hypothesis postulated by Tingay et al., (2011), in order to attribute the cause for the stress orientations observed in the Nile Delta.

5.1. LOCALIZED STRESS VARIATIONS DUE TO MECHINICAL PROPERTY CONTRASTS

Tingay et al., (2011) propose that mechanical property contrasts between the salt body and the adjacent block is a possible source that induces a localized maximum horizontal stress (S_H) rotation. The rheological contrast (i.e. salt is viscoelastic, sediments are elastic) is able to exert significant influence in certain regions, where there are special salt geometries undergoing structural movements.

Due to the visco-elastic behavior, all shear stresses in the salt vanish and all normal stresses tend to be isotropic and equal to the overburden load. Figure 5.1 shows the stress magnitudes extracted from the salt body during relaxation, which indicates a synchronized change of S_{11}, S_{22}, and S_{33} magnitudes. The resulting horizontal stresses, equal to the vertical stresses at the same location, are far exceeding the magnitude of horizontal stresses in the surrounding elastic rocks. On the other hand, driven by the elevated horizontal stresses, the salt body tends to squeeze out and push the adjacent rock from the edge and the angular zone. In regions near the edge or the angular zone of the salt body, the margin-normal horizontal stress (S_{xx}) becomes the maximum horizontal

stress (S_H), and thus a region where additional compression is generated. Detailed analysis for each scenario with respect to different shapes of the salt body will be performed in this context.

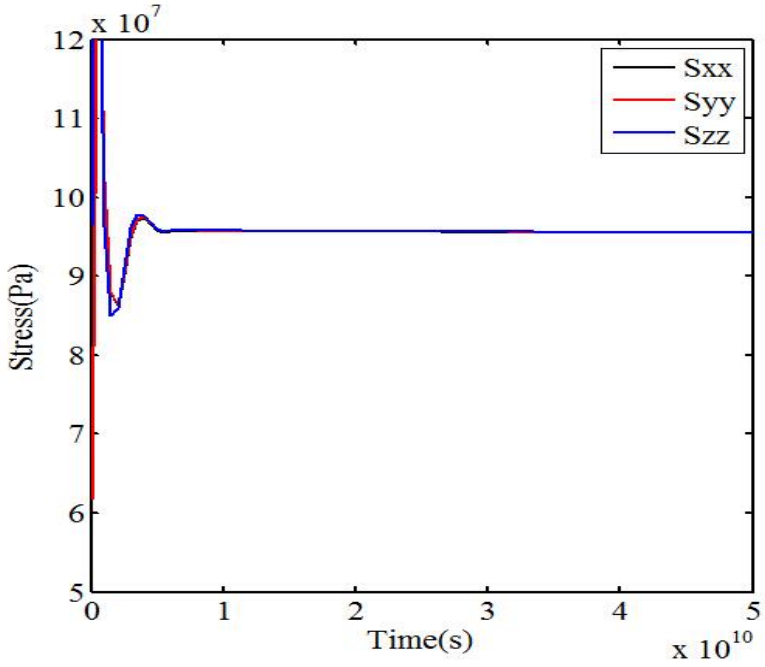

Figure 5.1. The magnitude of normal stresses (S_{xx}, S_{yy}, and S_{zz}) within the salt body during the relaxation

5.1.1. The Model Featuring a Flat Salt Sheet. In the model featuring a flat salt sheet, the stress field changes significantly in the region near the left edge of the salt sheet, where S_2 has rotated from margin-normal to a margin-parallel during salt relaxation. In this region, the elastic material in the Miocene layer has been compressed by the salt body, which is squeezed out by the pushing force from the gravitational gliding of the overburden sediments. As a result, the margin-parallel horizontal stress (S_{xx}) magnitude has exceeded the margin-normal horizontal stress (S_{yy}) magnitude and a prominent differential stress has been developed during salt relaxation (Figure 5.2; 5.3a,b.). Thus, the rotation of the S_H can be observed above and below the salt body, which coincides with the field observation for field B in the Nile Delta. However, due to the geometry of the salt sheet, the salt body can only be squeezed out to the left edge of the salt sheet. Most of the region below or far from the salt sheet (Figure 5.2; 5.3c, d.) is

not affected by the pushing force exerted by the salt body and features a margin-parallel S_H orientation (negative S_{xx}-S_{yy}) during the relaxation of salt.

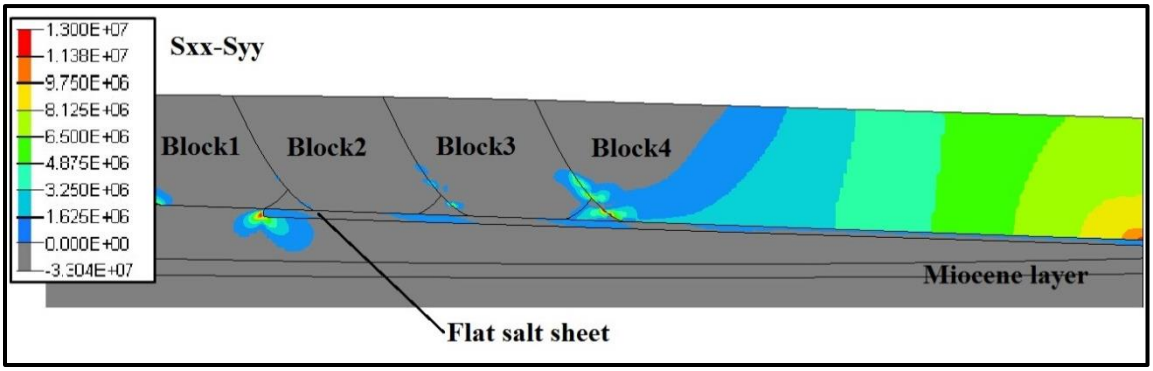

Figure 5.2. Contour plot showing the magnitude of S_{xx}-S_{yy} in the model featuring a flat salt sheet, indicating the margin-normal horizontal stress becomes dominant in Block 4 and the left edge of the flat salt sheet

5.1.2. The Model Featuring Isolated Salt Pyramids. As mentioned in Chapter 4.3, localized stress variations occur at the bottom of each overburden sediment block, and margin-normal S_H orientations are uniquely observed in those regions. Due to the gravitational potential, Block 1-4 pose great loads on the top of each salt pyramid, thus squeezing out the salt mass laterally and exerting horizontal compression to the elastic rock between adjacent salt pyramids. As a result, in regions between the salt pyramids, the x-direction stress component (S_{xx}) increases during salt relaxation and exceeds the y-direction stress component (S_{yy}) (Figure 5.4.). The compressed zones are formed when localized margin-normal horizontal stress becomes dominant, as shown for data points a), b), and c) in Figure 5.5. In the Miocene layers below the overburden sediments and salt pyramids, the salt bodies have almost no downward "out-pushing" due to the pyramid-shaped geometry. Thus, the stress field in the sub-salt sediments is barely affected during the salt relaxation and margin-parallel S_H are predominant (Figure 5.5d.). As observed in Chapter 4.3, no displacement discrepancy occurs between supra-salt and sub-salt sediments. The resulting displacement field does not show the detachment above and below salt bodies as observed in the Nile Delta (Tingay et al., 2011). However, this model provides a possible explanation for the generation of localized margin-normal S_H in the supra-salt sediments.

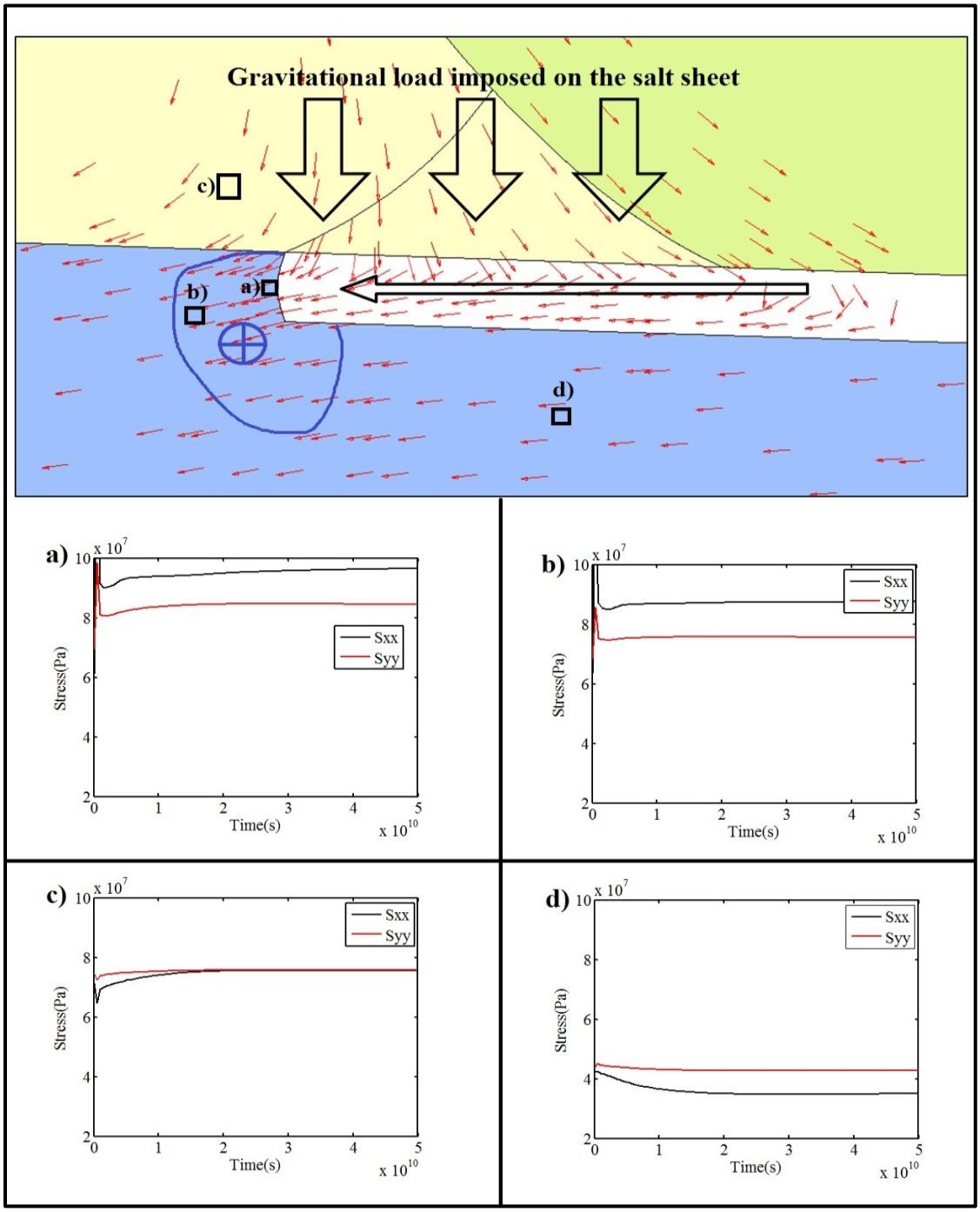

Figure 5.3. Upper part: Illustration of the compressed region being formed by the pushing and squeezing out by the salt body. The boxes a), b), c), and d) are the normal stresses on x and y direction changing with time. Data shown in a) is extracted at the location close to the left edge of the salt sheet; data plotting in b) is extracted at the compressed zone; c) at the supra-salt sediments; and d) at the sub-salt sediments

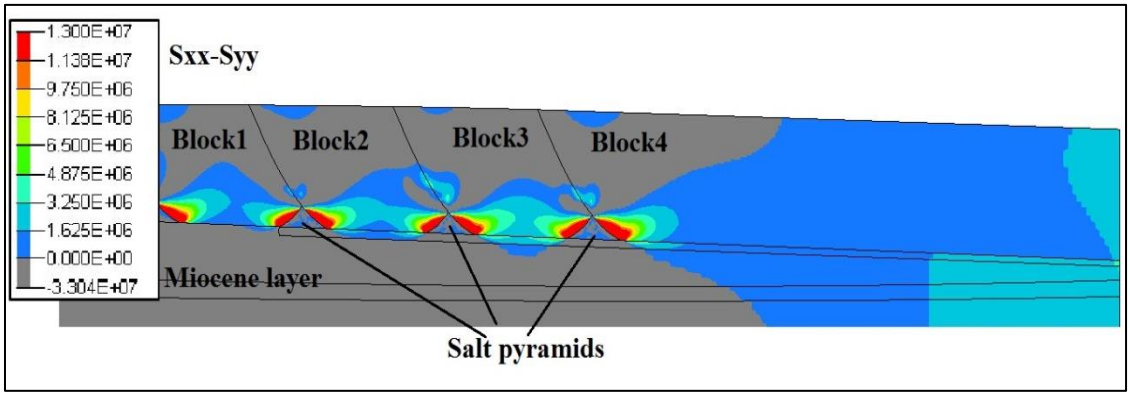

Figure 5.4. Contour plot of the magnitude of S_{xx}-S_{yy} in the model featuring isolated salt pyramids, indicating the margin-normal horizontal stress becomes dominant in the regions between salt pyramids and the right end of the model domain

5.1.3. The Model Featuring Salt Sheet Connected with Salt Pyramids. The displacement field shows that Block 2-4 gravitationally glide rightwards, Block 1 has a chaotic displacement field and generally moves torwards the left. As salt relaxation progesses with time, margin-normal S_H orientations are observed at the bottom of each block, but S_H orients margin-parallel in sediments below the continous salt body except for the region close to the left edge of the salt body (Figure 5.6.). Compressed zones are generated in the region labeled by blue eclipses in Figure 5.7. The formation of the compressed zones between salt pyramids (Figure 5.7 a,b.) and the predominant S_{xx} magnitude can be explained by the lateral squeezing evidence from isolated salt pyramids model. And the explanation for the model featuring the flat salt sheet is also suitable for the compressed region close to the left edge of the continous salt body (Figure 5.7c.). It needs to be mentioned that the salt squeezing-out effect has been enhanced by the gravitational gliding of Block2-4 (Figure 5.5a, 5.7d.). During the relaxation of salt bodies, like in the model with the flat salt sheet, an obvious decoupling has occurred: the continuous salt body isolates both the displacement field and the stress field within the sediments above and below. Thus the field observation for Field A in the Nile Delta can be explained.

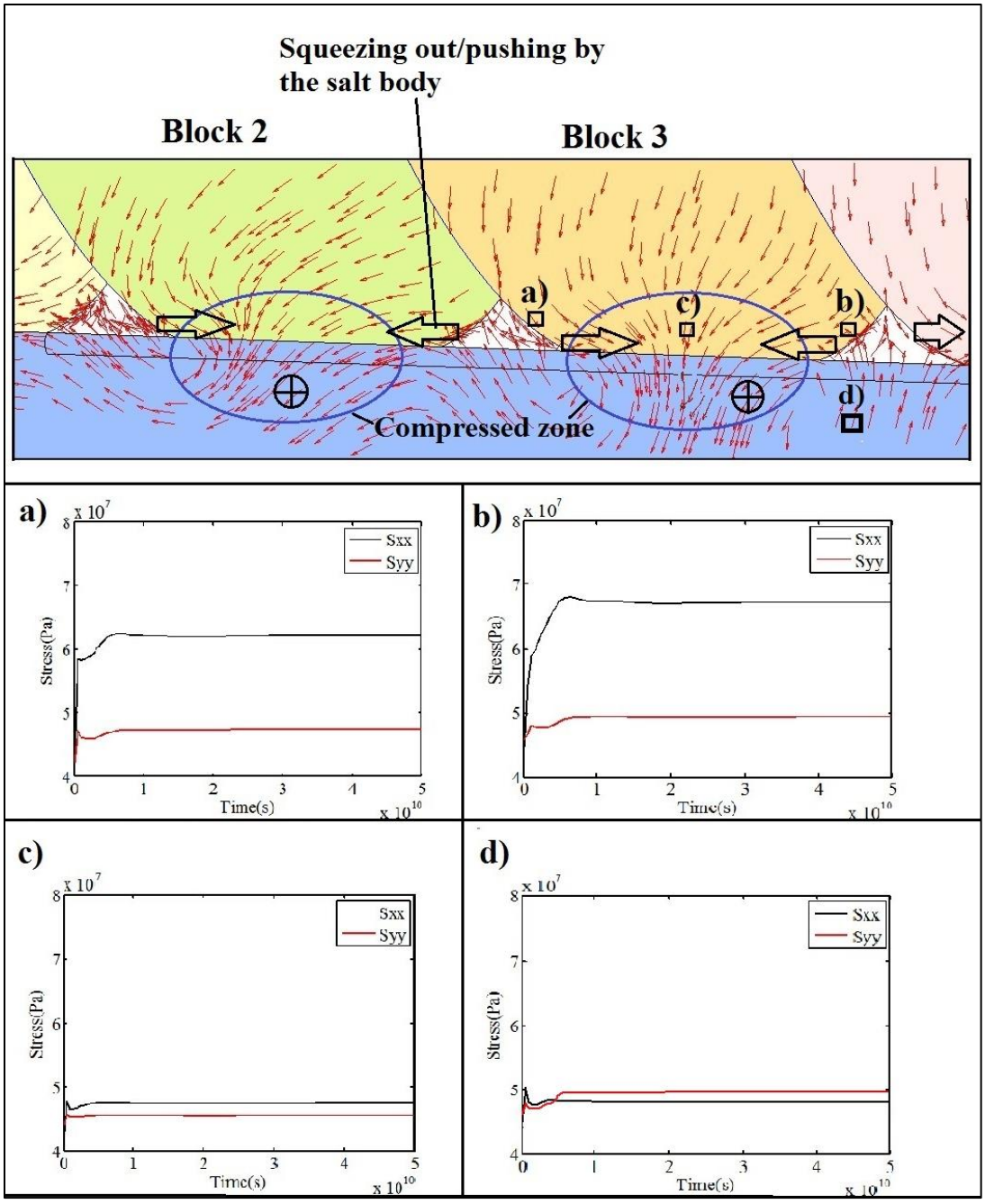

Figure 5.5. Upper part: Illustration of the locations of the compressed regions (blue eclipses) around the salt pyramids. The salt pyramids are squeezed out laterally, which induces compressed zones between two adjacent salt pyramids. Lower part: a) and b) The change of stresses along x and y direction on the right and left side of the salt pyramid in Block3; c) The change between the two adjacent salt pyramids; d) The change in the lower part of the compressed zone below c) in the Miocene layer

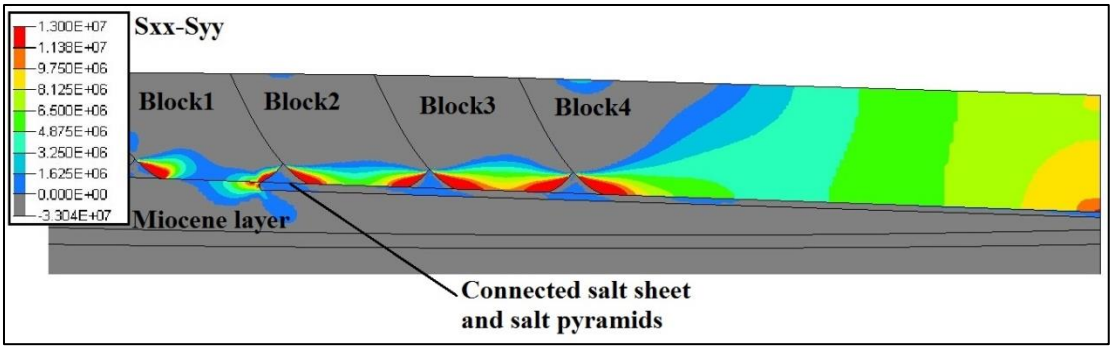

Figure 5.6. Contour plot of the S_{xx}-S_{yy} magnitude in the model featuring continuous salt sheet and pyramids, indicating the margin-normal horizontal stress becomes dominant in the Block 4 and the left edge of the flat salt sheet

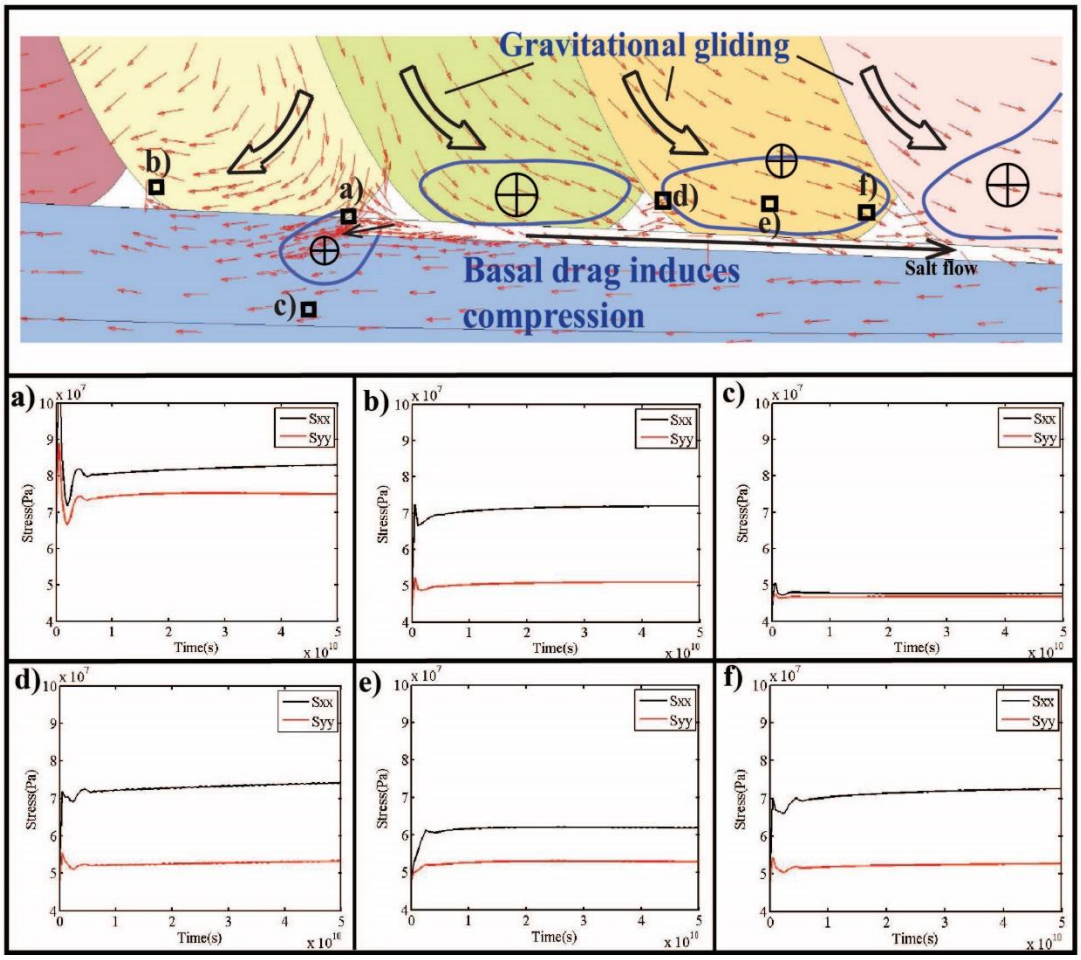

Figure 5.7. Upper part: Illustration of the compressed region being formed by the pushing and squeezing out by the salt body. Lower part: a) to e) showing the S_{xx} and S_{yy} magnitude change with time. a) locates near the left edge of the salt sheet; b) on the right side of the salt pyramid; c) in Miocene layer below the salt sheet; d) on the right side of the second salt pyramid connected to salt sheet; e) in the middle part of Block 3 bottom; f) on the left side of the third salt pyramid connected to salt sheet

5.2. BASAL DRAG INDUCED BY GRAVITATIONAL GLIDING

Basal drag is a term that initially describes the tectonic plate lithosphere movement due to the thermal-driven convection in the asthenosphere (Hudec and Jackson, 2007). In their conceptual model, Tingay et al., (2011) proposed to explain the stress orientation discrepancy above and below the salt layer by basal drag induced by the gravitational gliding of the supra-salt sediments.

When supra-salt sediments are gliding along listric faults, the salt body below the sediments is subject to a down-slope pushing force. Since the salt body is unable to transmit shear forces, friction is absent between salt sheet and overburden sediments, and the overburden sediments will be attached to the salt body during gravitational gliding. The salt body is able to "flow" under external loads at a low resistance. In terms of the entire supra-salt sediments, the down-slope gravitational gliding is enhanced by the flowing salt like being dragged by a force exerted from a basal region. As a result, sediments underlain by continuous salt body tend to move towards delta toe more drastically than underlain by elastic rocks. As introduced in Chapter 1.2.1, a non-moving model boundary condition is set on the left end representing the presence of the Eratosthenes seamount (Tingay et al., 2011; Loncke et al., 2006), which restricts the gravitational gliding. Within the overburden sediments, the margin-normal stress component increases and becomes dominant, thus a compressed zone is generated. However, at certain regions (mostly near the lower part of the faults), the salt body may have a localized damping effect to the gravitational gliding of supra-salt sediments. It needs to be emphasized that the basal drag effect is the predominant effect exerted by the salt in models of the flat salt sheet and the connected salt pyramids and salt sheet. The basal damping is only a localized phenomenon, and only occurs in the model containing both salt sheet and pyramids. Both of them contribute to the margin-normal S_H orientation observed in the supra-salt sediments.

5.2.1. The Model Featuring a Flat Salt Sheet. In this model, supra-salt sediments in Block 4 have a margin-normal maximum horizontal stress (S_H) orientation. The sub-salt layers features a margin-parallel S_H orientation. As shown in Figure 5.8a, the high differential stress (S_{xx}-S_{yy}) magnitude indicates the margin-normal horizontal stress (S_{xx}) becomes predominant the majority of Block 4, where S_{xx} and S_{yy} are equal at the

beginning of the simulation. Figure 5.8a also shows S_{yy} dominated the area in Block 1-3, which reduces slower than S_{xx}. The displacement field in Figure 5.8b shows that Block 1 mainly moves leftwards, while Block 2 and 3 feature obvious gravitational gliding occurred towards the right side. Thus a stress release zone with a margin-parallel S_H is generated in Block 2 and 3. The gravitational gliding of Block 2-4 results in the mass within the salt sheet flowing towards delta toe and dragging the bottom of Block 4 rightwards. In the Block 4, a compressed zone with predominately margin-normal S_H (within the dashed line in Figure 5.8a and b) is thus formed by the basal drag effect.

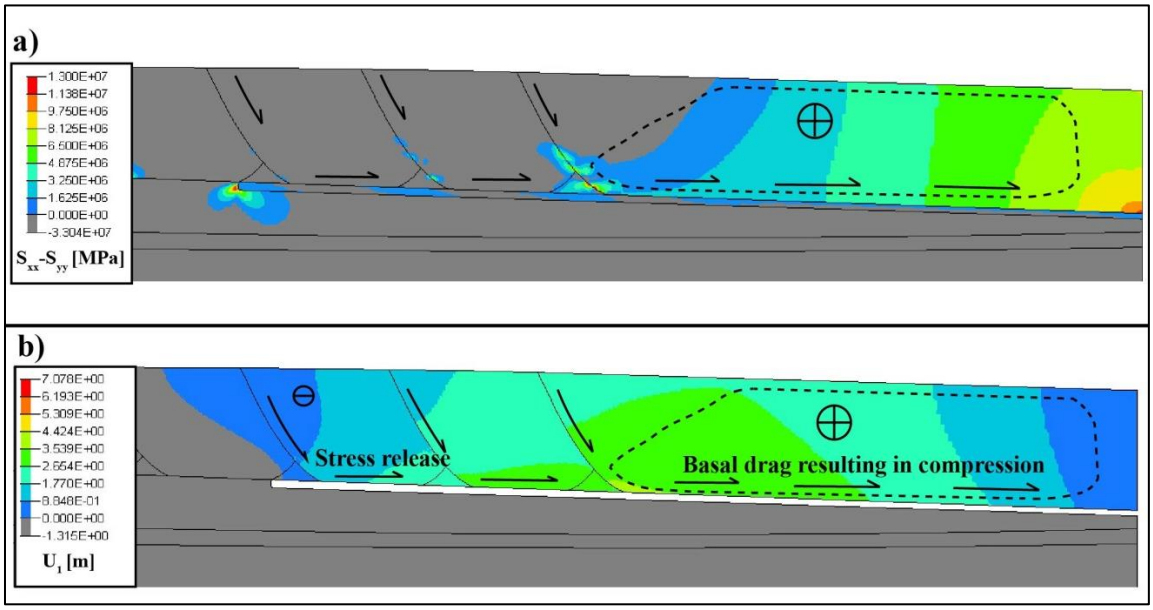

Figure 5.8. A comparison of differential stress and x-direction displacement fields in the model featuring a flat salt sheet. a) Differential stress contour of S_{xx}-S_{yy} in all supra-salt sedimentary blocks showing S_{xx} overcome S_{yy} significantly and result in zone of compression in the Block4. b) The contour plot of displacement along x-axis, U_1. The region between growth faults is featured by a stress release, caused by the gravitational gliding of Block 2 and 3. Basal drag results in prominent displacement in Block 4, where predominant S_{xx} and compressed zone are observed

5.2.2. Connected Salt Sheet and Salt Pyramids. In this model, as introduced in Chapter 4.4, the margin-normal S_H orientations occur in the bottom part of Block 2-3 and the majority of Block 4 (Figure 5.9a.). The particular geometry of the salt body is the main reason that results in the widely distributed margin-normal S_H. Gravitational gliding

occurs in Block 2-4, but Block 1 moves in the opposite direction (Figure 5.9b.). The increased S_{xx} magnitude between two salt pyramids in Block 1 is induced by the lateral squeezing force, as explained in Chapter 5.1.3. The increased S_{xx} magnitude in Block 2 and 3 is the result of the gravitational gliding induced basal drag. Rather than being released like the model featuring the flat salt sheet, compressional stresses accumulate at the bottom of Block 2 and 3 due to the continuity of the salt body and the presence of the salt pyramids. The salt pyramids above the salt sheet act as barriers and impede the gravitational gliding of Block 2 and 3. As a result, the margin-normal S_{xx} surpasses S_{yy} in magnitude (Figure 5.9a.) and generates zones of compression (Figure 5.9b.). Meanwhile, the salt sheet between pyramids is also subjected to pushing forces from compressed zones above. Thus, the down-slop salt mass flow is enhanced which resulting a more drastic basal drag effect than the other model. Block 4, has a larger displacement and generates the margin-normal S_{xx} with higher magnitude.

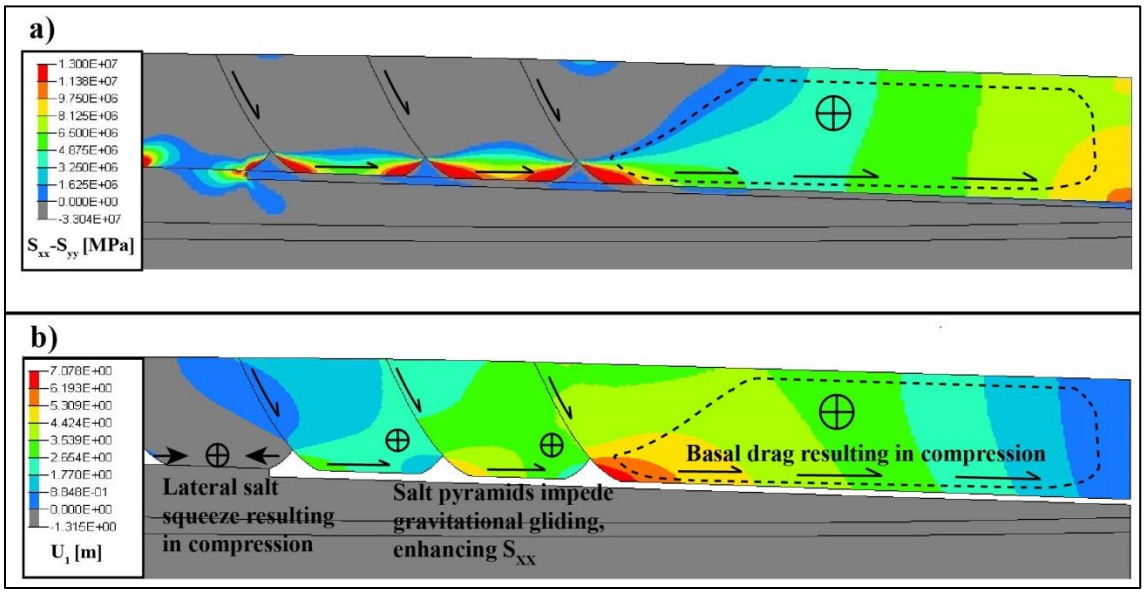

Figure 5.9. A comparison of differential stress and x-direction displacement fields in the model featuring connected salt sheet and pyramids.. a) Differential stress contour of S_{xx}-S_{yy} in all supra-salt sedimentary blocks shows S_{xx} overcome S_{yy} significantly and result in zone of compression in the bottom of Block 1-3 and Block4; b) Contours of displacement along the x-axis, U_1. Gravitational gliding is obvious for Block 2-4, and compressed zones are located in the bottom of Block 1-3 and Block 4

5.3. THE INFLUENCE OF SALT VISCOSITY

As presented in Chapter 4.6, a salt viscosity change does influence neither the gravitational gliding of supra-salt sediment nor the stress and displacement field in the final result. It can be explained that the salt bodies with various viscosities are sufficiently relaxed by the end of the simulation.

As shown in the Figure 5.10, a temporary stress perturbation is developed at the initial stage because of suddenly loading the salt body which has a creep behavior. The lower salt viscosity the more drastic stress perturbation appears. But when the stress perturbation is dissipated, the stress magnitudes of salt with different viscosities become almost equal. As a consequence, the resulting stress and displacement fields of salt with different viscosities are same by the end of the simulation.

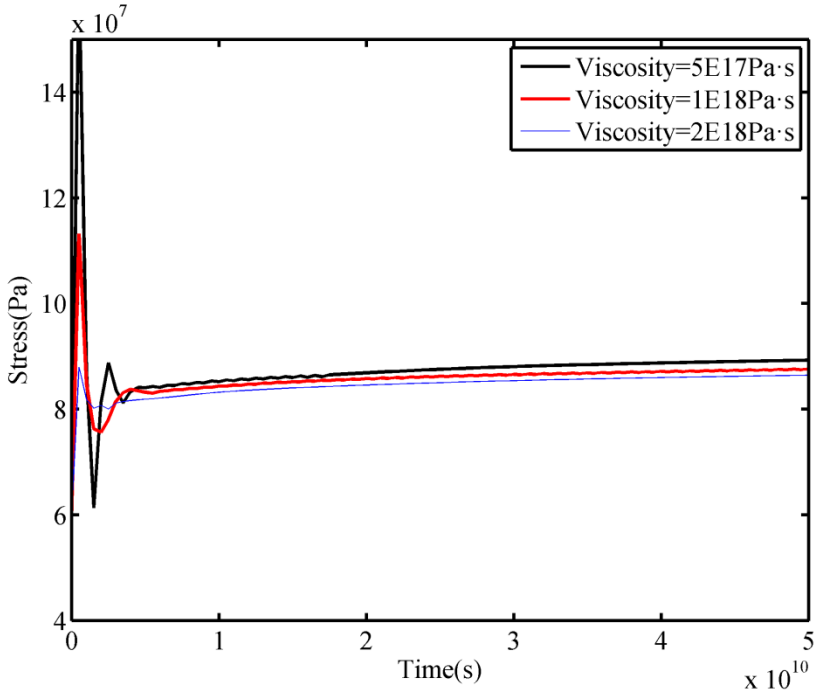

Figure 5.10. The stress magnitudes (S_H is selected as an example) in the salt body of different viscosities change with time. The perturbation of stress magnitude is more drastic in the salt body with lower viscosity at the beginning. Then, stress magnitudes become equal

5.4. THE INFLUENCE OF FRICTION COEFFICIENT

The friction coefficient (mu) on the fault plane is able to pose significant influence on the gravitational gliding of supra-salt sediments. Figure 5.11 shows the differential stress contours of the supra-salt sediments for different mu assigned on the faulting planes. With mu decreasing, the supra-salt sediment gravitational gliding is enhanced (Figure 4.13.). As a result, the regions showing increased S_{xx} (Figure 5.11.), including the area between the salt pyramids and the basal dragging zone in Block 4, are all expanded and have a higher differential stress magnitude.

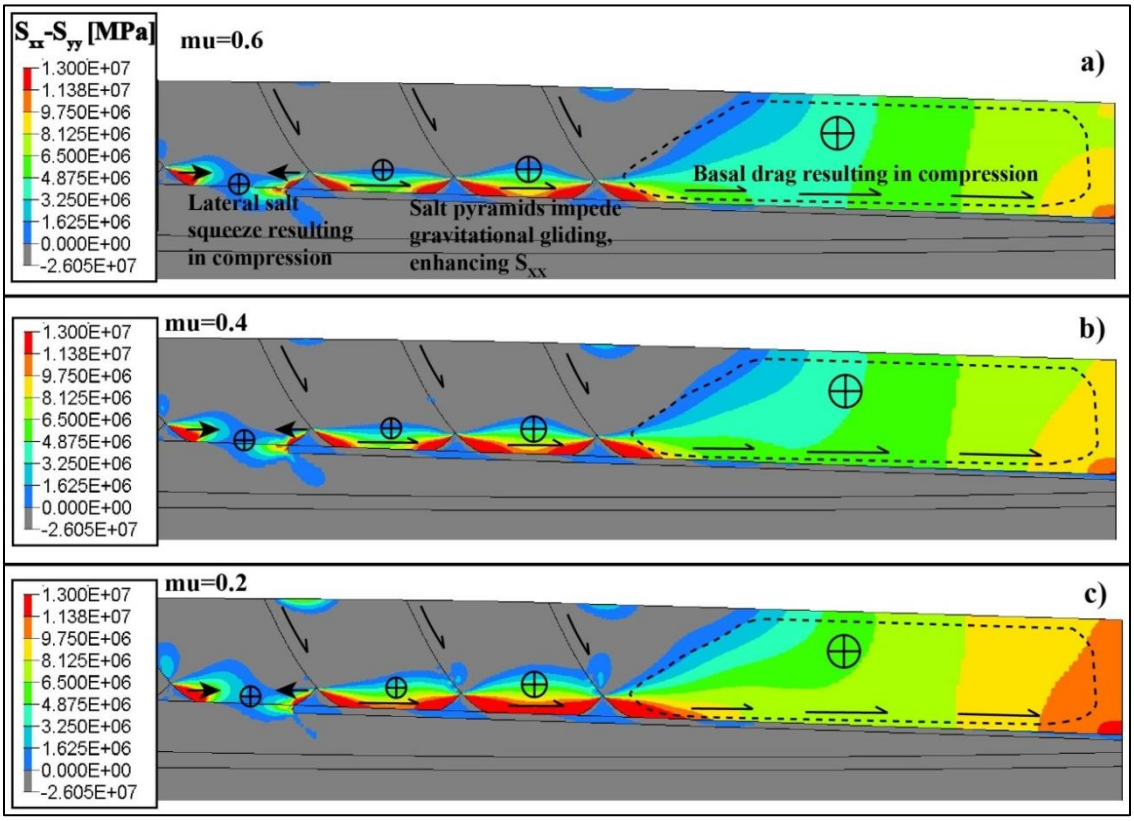

Figure 5.11. Differential stress contour of S_{xx}-S_{yy} in all supra-salt sedimentary blocks in the model with different friction coefficients. a) The model with a friction coefficient of 0.6 assigned on faulting plane; b) The model with a friction coefficient of 0.4; c) The model with a friction coefficient of 0.2. Compressed zones are located in the bottom of Block 1-3 and Block4, and compressed zones become bigger when the friction coefficient becomes smaller

5.5. THE ROLE OF PORE PRESSURE

In this study, all stresses are assigned to be total stresses and the entire model domain is assumed to have a hydrostatic pore pressure distribution. Studies on evaporites (Senseny et al., 1992; Cristescu, et al., 1993; Warren, 2004; Nikolinakou et al., 2011) have shown that evaporites are impermeable sediments with very low porosity and permeability, for which pore pressure is absent. As shown in Figure 5.12, the pore pressure gradient vanishes in the salt body and will continue below the salt body. When the salt body is large and continuous enough, the fluid within the sediment above and below the salt body can be isolated. Compared with the normal pore pressure gradient, a high pore pressure (overpressure) is likely to be accumulated above the salt body, and a low pore pressure (underpressure) is likely to be generated below the salt body during the long-term evolution (Figure 5.13.) (Shaker and Smith, 2002; Hantschel and Kauerauf, 2009). Shaker and Smith, (2002) consider the density difference between salt and adjacent rock as the primary reason that leads the generation of the salt-related overpressure and underpressure. It needs to be emphasized that the overpressure and underpressure zones can only be formed when the salt body is continuous and thick enough (Farmer et al., 1996). In this study, the salt sheet has a thickness of 270m and a length of 28km, which would be able to induce underpressure and overpressure.

The change in pore pressure can be described by the principle of pore pressure - stress coupling (Altmann et al., 2010, 2014). According to the pore pressure - stress coupling mechanism, the effective principal stresses (σ_1', σ_2' and σ_3') are increasing or decreasing at different rates when pore pressure is changing:

- σ_2' and σ_3' are increasing/decreasing at the same rate when pore pressure is increasing/decreasing;
- σ_1' is increasing/decreasing faster than σ_2' and σ_3' when pore pressure is increasing/decreasing.

It has been introduced in Chapter 4.2 that the vertical stress is the maximum principal stress in the model domain deeper than 1500m, and thus the maximum and minimum horizontal stresses (S_H and S_h) are the intermediate and minimum principal stresses. Consequently, an increase of pore pressure in the supra-salt overpressure zone

(Figure 5.13.) imposes the same influence to S_H and S_h magnitudes, which does not affect the resulting horizontal stress orientations in the supra-salt sediments.

Case studies in the Gulf of Mexico (Shaker and Smith, 2002; Baker et al., 2003; Shaker, 2007) provide quantitative evidence that for a continuous and thick salt body buried at depths of around 3000m, the overpressure magnitude above the salt body is around 0.2MPa, and the underpressure below the salt body is not obvious. As a consequence, since the magnitude of differential stress (S_V-S_h) in the compressed zones of the model has a general magnitude range of 10-20MPa, the effect of overpressure and underpressure can be neglected.

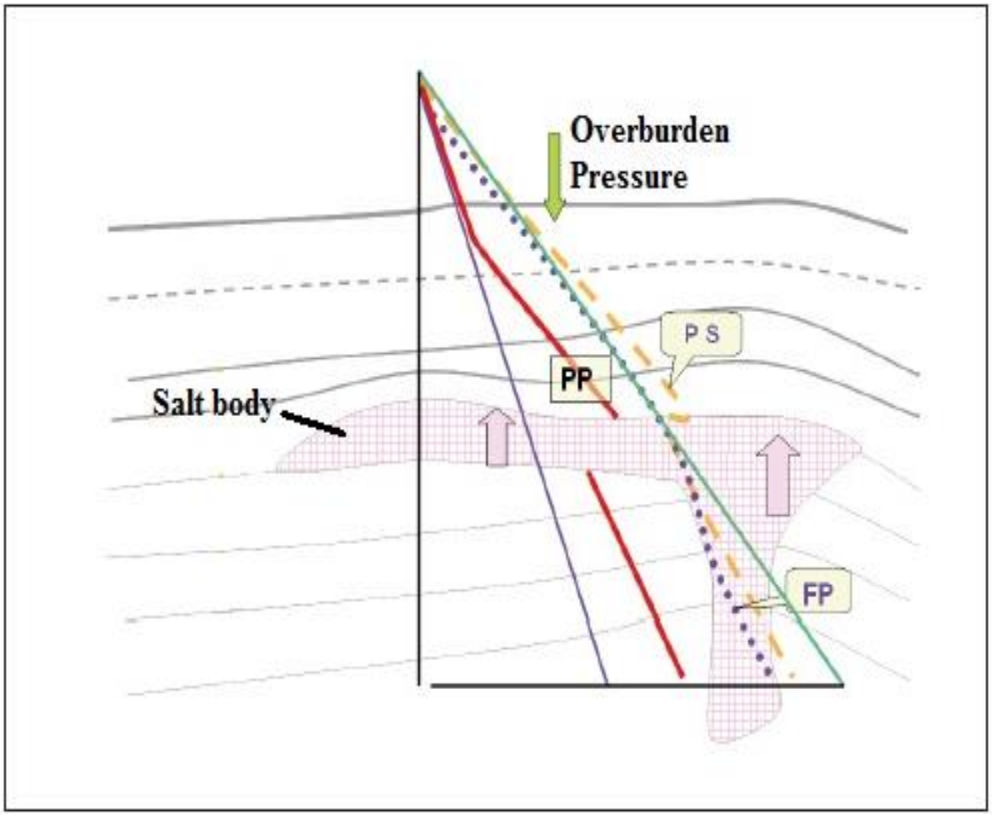

Figure 5.12. Illustration of pressure gradients through the salt body. Red solid line represents the pore pressure gradient, which interrupted by the salt body. Yellow dashed line is maximum principal stress; Blue dashed line is the minimum principal stress; Blue solid line is the hydrostatic pressure; Green solid line is the overburden pressure gradient. Figure from Shaker and Smith, (2015)

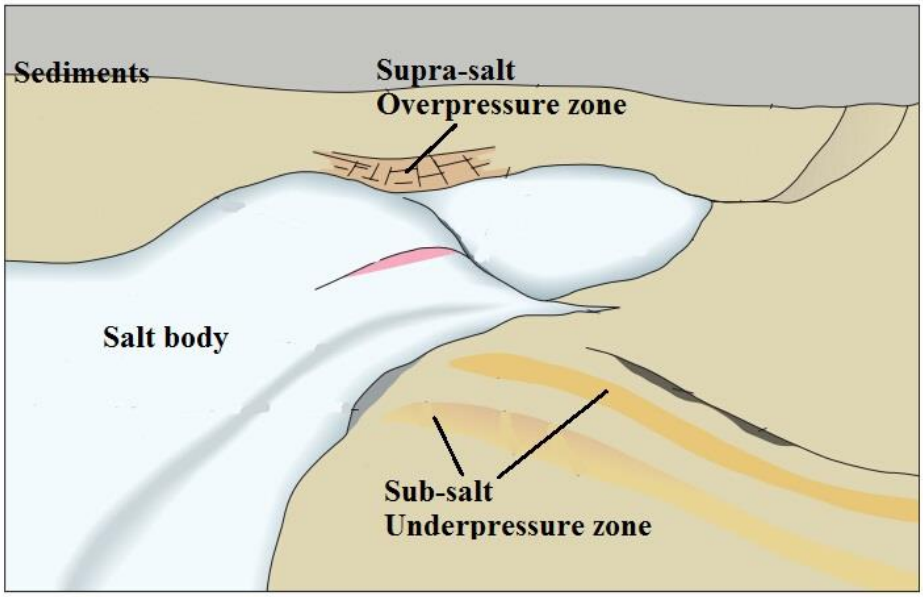

Figure 5.13. Illustration of the location of overpressure and underpressure zone with respect to a large and continuous salt body. Normally, overpressure zones are developed above the salt body and underpressure zones are developed below the salt body. Figure from Gabrielsen, (2008)

5.6. LIMITATIONS

This study aims at modeling the gravitational gliding of supra-salt sediments using the finite-element simulator of Abaqus™. However, due to the nature of this study and the availability of reliable data, this study has some limitations.

1) The most fundamental limitation of this study is the lacking of field calibration. The only available qualitative data sources are the World Stress Map database and field data from Tingay et al., 2011. For certain zones of interest, stress data is lacking. No quantitative stress data is available to verify the stress magnitudes in modeling results.
2) Material property data is unavailable in the study region. The material property parameters assigned in this study are adapted from studies of other researchers (Hudec and Jackson, 2007; Luo et al., 2010; Nikolinakou et al., 2011). The data from field measurements such as density log, hydraulic/mini-frac test, and caliper/image logs is inaccessible due to confidential reason (Tingay et al., 2012).

3) Neglecting the pore pressure is also a major limitation. As discussed in Chapter 5.4, the pore pressure distribution is able to affect the stress field to a certain extent. Overpressure and underpressure regions are able to develop during the relaxation of salt, which may affect the regional stress regime due to the pore-pressure and stress coupling effect (Tingay et al., 2012; Altmann et al., 2010, 2014; Eckert et al., 2014).

5.7. IMPLICATIONS FOR HYDROCARBON PRODUCTION

During the relaxation of salt bodies and the evolution of supra-salt faults, the stress field changes significantly. As discussed in Chapter 5.1, the mechanical property contrast and basal drag effects can lead to the reorientation of the stress field and the elevation of stress magnitudes in certain regions. This may exert significant influence to the operation of oil/gas exploration and exploitation. In the context of the discovery of the 30 trillion cubic feet gigantic "Zohr" gas field in the supra-salt region in the northeast Nile Delta (Eni, 2015), a sufficient understanding of how salt-related stress field changes affect the mechanical applications such as seal breach, wellbore stability, perforation design, and sanding prevention is of great importance to the oil industry.

Fault seal is a key factor controlling hydrocarbon accumulation. Its integrity and condition determine the quality and economic value of the reservoir (Jones et al., 2002). The fault filled with impermeable minerals which block the fluid flow, normally features a very low mechanical strength (almost zero) and can be easily reactivated (Yielding et al., 1997; Jones et al., 2002; Fjaer et al., 2008). During the gravitational gliding of supra-salt sediments, the salt bodies are being squeezed out and impose abnormally high loads to the adjacent sediments, which greatly increases the seal breach risk of supra-salt faults. In regions near the tips and edges of salt bodies (Figure 5.13a: A, B, C), the differential stresses increase (shown by the high von Mises stress magnitudes in Figure 5.14a) and the corresponding Mohr Circle plots (Figure 5.14b.) indicate failure may occur. For a fault plane located in the supra-salt sediments, near the top tip of the salt pyramid, has the largest magnitude of differential stress which means the highest likelihood of seal breach (Figure 5.14b: A). In parts that both far from the salt pyramid and in contact with the salt pyramid, the resulting differential stresses are not remarkable (Figure 5.14c.), which

indicates less failure risk and stable sealing. It needs to be clarified that the stress magnitudes based on which failure is judged are lacking calibration and cannot represent realistic conditions of rocks in the Nile Delta. This study aims to qualitatively assesse the general likelihood of failure in terms of the resulting stress field and compares the seal breach risk at different location with respect to the salt geometry.

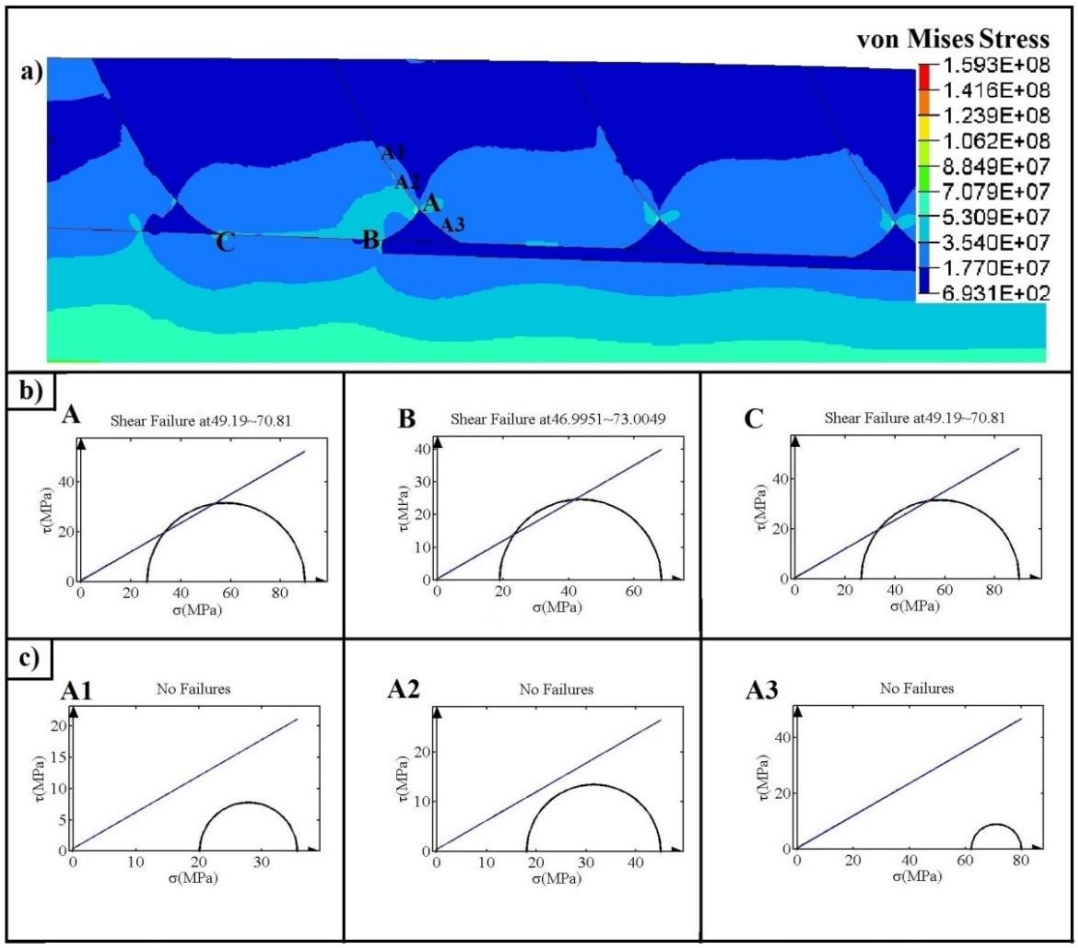

Figure 5.14. Illustration of failure occurrence in different locations. The model featuring a continuous salt sheet and salt pyramids is selected as an example. a) Contour represents the magnitude of von Mises Stress. b) The Mohr Circle plots of regions that have higher likelihood of failure. A locates near the top tip of the salt pyramid, B locates near the left edge of the salt sheet, C locates near the bottom tip of salt pyramid. c) The Mohr Circle plots of different parts at the supra-salt fault. A1 and A2 locates above the salt pyramid, A3 locates at the edge of salt pyramid. A cohesion of zero and a friction angle of 30 degree are assigned

Drilling trajectory design is another challenge in the supra-salt regions of the Nile Delta. For horizontal wells in an extensional stress regime, the stability of the wellbore is largely dependent on the drilling direction (Hillis and Williams, 1993):

1) The minimum horizontal stress (S_h) direction is the most stable drilling direction because the maximum horizontal stress (S_H) and the vertical stress (Sv) that act on the borehole have the smallest magnitude of differential stress.
2) The S_H direction is the least stable drilling direction due to the largest differential stress between Sv and S_h, which are acting on the borehole plane.

In regions between salt pyramids and above continuous salt sheet, the intermediate principal stress (i.e. S_H) is oriented margin-normal. Horizontal wells that targeted these regions should be drilled along a margin-parallel trajectory. Drilling trajectories should also avoid passing through high failure risk regions near the tips and edges of salt bodies.

Moreover, perforation stability and related sand production are highly affected by salt-related stress reorientation (King, 1989). For reservoirs located in weakly consolidated sequences, like supra-salt sediments in the Nile Delta, appropriate perforation orientation is especially important for maximizing perforation effect and minimizing sand production (Almaguer et al., 2002). Various field and experimental studies (Santrarelli et al., 1991; Morita and Mcleod, 1995; Hoek et al., 2000; Venkitaraman et al., 2000; Tronvoll et al., 2004) have confirmed that perforating along the intermediate stress orientation can greatly reduce the possibility of perforation failure and subsequent sand influx. According to the previous discussion, the preferred perforation orientations for reservoirs situated in different regions with respect to different salt bodies in the model domain of this study are shown as following:

- For regions near the tips of salt pyramids and edge of salt sheet, the preferred perforation orientation should be in margin-parallel direction;
- For the rest of the model domain deeper than 1500m, the preferred perforation orientation should be in margin-normal direction.

6. SUMMARY AND CONCLUSIONS

This study simulates the gravitational gliding of supra-salt faults with different salt geometries, friction coefficients on supra-salt growth faults, and salt body viscosities. The modeling results are able to reproduce the same stress and displacement field as the field observation, which provides additional evidence that evaporites act as mechanical detachment zones during the structural evolution. The overall resulting stress field in the entire model domain corresponds with the stress distribution predicted by classic deltaic model. The hypotheses proposed by Tingay et al, (2011) in order to explain how the salt body affects the stress field are validated by the modeling result, qualitatively and quantitatively.

When salt bodies are presented in isolated salt pyramids, localized stress variations occur due to the mechanical property contrast between the creep salt and the elastic sediment blocks. Due to the gravitational gliding the salt is "squeezed out" laterally and compresses the adjacent elastic sediment blocks. Thus, compressed zones with margin-normal S_H are generated in regions between the growth faults. However, no obvious and continuous detachment between supra-salt and sub-salt sediments is observed during the whole possess of salt relaxation. Hence, the model with isolated salt pyramids is not sufficient enough to reproduce both field S_H measurements and geological structural observations. Localized stress variations also occur at the left edge of the flat salt sheet resulting in compressed zones, where margin-normal S_H are generated below the salt sheet due to the influence of salt geometry and S_H remains margin-parallel above the salt sheet.

For the model featuring continuous salt sheet and pyramids, basal drag effect due to the gravitational gliding induces a margin-normal S_H concentration within the supra-salt sediments. Both models featuring a flat salt sheet and continuous salt sheet and pyramids have the most prominent basal drag effect occurred in the 4th sediment block. A long and continuous salt body detaches the stress and displacement fields, and thus opposite S_H orientations and opposite displacement directions above and below it are the result. This modeling result provides quantitative evidence to confirm the key observation in the study of Tingay et al, (2011 and 2012) that evaporites act as a detachment zone.

Reduction of the frictional resistance on the supra-salt faults is able to enhance the gravitational gliding of supra-salt sediments, thus amplifying the effect of both mechanical property contrast and basal drag. However, the viscosity change of the salt body cannot pose any influence on the modeling result, because the modeling time is long enough to balance the instantaneous stress concentration due to viscosity change.

The stress orientation data from the field operation (Figure 1.6.) can be explained by results of models with different salt geometries. S_H orientations observed in Field A (margin-normal in supra-salt layers and margin-parallel in sub-salt layers) can be induced by the basal drag effect, which are the predominant stress pattern in the supra-salt region of the Nile Delta. S_H orientations observed in Field B (margin-parallel in supra-salt layers and margin-normal in sub-salt layers) are likely to be localized stress rotations associated to the mechanical property contrasts.

7. BIBLIOGRAPHY

Aal, A., Barkooky, A., Gerrites, M., Meyer, H., Schwander, M., Zaki, H., 2000. Tectonic evolution of the Eastern Mediterranean Basin and its significance for hydrocarbon prospectively in the ultradeepwater of the Nile Delta. *The Leading Edge*, Oct 2000.

Altmann, J.B., Müller, B.I.R., Müller, T.M., Heidbach, O., Tingay, M.R.P., and Weißhardt, A., 2014. Pore pressure stress coupling in 3D and consequences for reservoir stress states and fault reactivation. *Geothermic*, 52, 195-205.

Altmann, J.B., Müller, B.I.R., Müller, T.M., Heidbach, O., Tingay M.R.P., 2010. Poroelastic contribution to the reservoir stress path. *International Journal of Rock Mechanics and Mining Sciences,* 47(7), 1104-13.

Badawy, A., 2004. Present-day seismicity, stress field and crustal deformation of Egypt. *Journal of Seismology* (2005) 9: 267-276.

Badawy, A., Mohamed, G., Omar, K., Farid, W., 2014. The northern Egyptian continental margin. *Journal of African Earth Sciences*, 101 (2005) 177-185.

Barker, J.W., and Meeks, W.R., 2003. Estimating Fracture Gradient in Gulf of Mexico Deepwater, Shallow, Massive Salt Sections. SPE 84552.

Bosworth, W., 2006. North Africa-Mediterranean Present-day Stress Field Transition and Implications for Fractured Reservoir Production in the Eastern Libyan Basins. *Geology of East Libya*, 4, pp. 123-138.

Buchmann, T. J., and P. T. Connolly., 2007. Contemporary kinematics of the Upper Rhine Graben: A 3D finite element approach, *Global Planet. Change*, 58(1), 287-309, doi: 10.1016/j.gloplacha.2007.02.012.

Byerlee, J.D., 1978. Friction of rocks. *Geophysics*. 116, 615-26.

Coulomb, C.A., 1773. Application of the rules of maxima and minima to some problems of statics related to architecture. *Acad. Roy. Sci. Mem. Math. Phys.*, 7, 343-82.

Cristescu, N.D., 1993. A General Constitutive Equation for Transient and Stationary Creep of Rock Salt. *International Journal of Rock Mechanics Mining Science & Geomechanics*. 30(2), pp. 125-140.

Davis, G., Reynolds, S., Kluth, C., 2011. Structural geology of rocks and regions 3rd ed. Wiley, Hoboken, NJ.

Eckert A., and Liu, X., 2014. An improved method for numerically modeling the minimum horizontal stress magnitude in extensional stress regimes. *Int. Journal of Rock Mechanics and Mining Sciences*, 70, 581-592.

Eckert, A., Connolly, P., Liu, X., 2014. Large-scale mechanical buckle fold development and the initiation of tensile fractures. *Geochemistry, Geophysics, Geosystems*, 15, 4570–87.

Eni, 2015. Eni discovers a supergiant gas field I the Egyptian offshore, the largest ever found in the Mediterranean Sea. [online] Available at: <http://www.eni.com/en_IT/media/press-releases/2015/08/Eni_discovers_supergiant_gas_field_in_Egyptian_offshore_the_largest_ever_found_in_Mediterranean_Sea.shtml>.

Farmer, P., Miller, D., Pieprzak, A., Woods, R., 1996. Exploring the Subsalt. *Oilfield Review* 8, no.5 (1999): 22-35.

Fjaer, E., Holt, P., Horsrud, A.M., Raaen & R. Risnes., 2008. Petroleum Related Rock Mechanics 2nd edition, first edition 1992. Elsevier, Radarweg, Netherlands.

Fredrich et al., 2003, Stress Perturbations Adjacent to Salt Bodies in the Deepwater Gulf of Mexico, SPE 84554,P1-14.

Gabrielsen, R.H., Fort, X., Martinsen, O., 2008. Recent Advances in Geoscience: Salt: Deformation, Trapping. GEO ExPro May 2008.

Gampala, R., Elzey, D.M., Wadley, N.G., 1995. Power-Law Creep Blunting of Contacts and Its Implications for Consolidation Modeling. *Acta Metallurgica*. Vol. 44, No. 4, pp. 1479-1495.

Goodman, R.E., 1993. *Introduction to Rock Mechanics*, 2nd ed. John Wiley & Sons, New York and Chichester.

Hantschel, T., Kauerauf, A.I., 2009. *Fundamentals of Basin and Petroleum Systems Modeling*. Springer-Verlag Berlin Heidelberg Doi 10.1007/978-3-5-340-72318-9 2.

Healy, D., Butler, R.W.H., Shipton, Z.K., and Sibson, R.H., 2012, Stress, faulting, fracturing and seismicity: the legacy of Ernest Masson Anderson, In: Healy, D., Butler, R.W.H., Shipton, Z.K., and Sibson, R.H. (eds) 2012. *Faulting, Fracturing and Igneous Intrusion in the Earth's Crust.* Geological Society, London, Special Publications, 367, p.155-170, doi: 10.1144/SP367.11.

Hibbitt, D., Karlsson, B., Sorensen, P., 2001. *Abaqus/ Standard User's Manual*, vol. 1 and 2, version 6.12. Hibbitt Karlsson and Sorensen Inc., Pawtucket, Rhode Island.

Hillis, R. R., and Williams, A. F., 1993. The stress field of the North West Shelf and wellbore stability. *Australian Petroleum Exploration Association Journal*, v. 33, p. 373-385.

Hoek, P.J., Kooijman, A.P., Bree, P., Kenter, C.J., Zheng, Z., Khodaverdian, M., 2000. Horizontal-Wellbore Stability and Sand Production in Weakly Consolidated Sandstones. SPE-65755, *SPE Drill & Completion* 15(4).

Hoskins, E.R., Jaeger, J.C., and Rosengren, K.J., 1968. A Mediem Scale Direction Friction Experiment. *International Journal of Rock Mechanics*, 5, 143-54.

Jackson, M.P.A., Vendeville, B.C., and Schulz-Ela, D.D., 1994. Salt-related structures in the Gulf of Mexico: A field guide for geophysicists. *The Leading Edge*, v.13 no.8, pp. 837-842.

Jackson, M.P.A., Vendeville, B.C., and Schulz-Ela, D.D., 2003. Structural Dynamics of Salt Systems. *Annual Review of Earth and Planetary Sciences*, Nov 2013,DOI: 10.1146/annurev. ea.22.050194.000521.

Jaeger, J.C., Cook, N.G.W., Zimmerman, R.W., 2007. *Fundamentals of Rock Mechanics*. 4th ed. John Wiley & Sons.

Jone, R.M., Dewhurst, D.N., Hillis, R.R., Mildren, S.D., 2002. Geomechanical Fault Characterization: Impact on Quantitative Fault Seal Risking. SPE 78213.

Keken, P.E., Spiers, C.J., Berg, A.P., Muyzert, E.J., 1993. The effective viscosity of rocksalt: implementation of steady-state creep laws in numerical models of salt diapirism. *Tectonophysics*, 225 (1993) 457-476.

King, R.C., Backé, G., Tingay, M., Hillis, R., and Mildren, S., 2012, Stress deflections around salt diapirs in the Gulf of Mexico, In: Healy, D., Butler, R.W.H., Shipton, Z.K., and Sibson, R.H. (eds) 2012. *Faulting, Fracturing and Igneous Intrusion in the Earth's Crust*. Geological Society, London, Special Publications, 367, p.155-170, doi: 10.1144/SP367.11.

Loncke, L., Gaullier, V., Bellaiche, G., Mascle, J., 2002. Recent depositional pattern of the NDSF from echo-character mapping. Interactions between turbidity currents, mass-wasting processes and tectonics. *AAPG Bulletin* 86,1165–1186.

Loncke, L., Gaullier, V., Mascle, J., Vendeville, B., and Camera, L., 2006, The Nile deep-sea fan: An example of interacting sedimentation, salt tectonics, and inherited subsalt paleotopographic features. *Marine and Petroleum Geology*, v. 23, p. 297–315, doi: 10.1016/j.marpetgeo.2006.01.001.

Loncke, L., Gaullier, V., Droz, L., 2009, Multi-scale slope instabilities along the Nile deep-sea fan, Egyptian margin: A general overview. *Marine and Petroleum Geology* 26 (2009) 633-646.

Luo, G., and M. Liu., 2009. How does trench coupling lead to mountain building in the Subandes? A viscoelastoplastic finite element model, *Journal of Geophysics Research*., 114, B03409, doi:10.1029/2008JB005861.

Luo, G., Nikolinakou, M.A., Flemings, P.B., and Hudec, M.R., 2010. Geomechanical modeling of stresses adjacent to salt bodies: Part 1 – Uncoupled models, *AAPG Bulletin*, v.96, no. 1, p. 43-64.

Marten, R., Shann, M., Mika, J., Rothe, S., and Quist, Y., 2004. Seismic challenges of developing the pre-Pliocene Akhen Field offshore Nile Delta: *The Leading Edge*, v. 23, p. 314–320, doi:10.1190/1.1729228.

Mascle, J., Zitter, T., Bellaiche, G., Droz, L., Gaullier, V., Loncke, L., 2001. The Nile Deep Sea Fan: Preliminary Results from a Swath Bathymetry Survey. *Marine and Petroleum Geology* 18 (2001) 471-477.

Morita, N. and McLeod, H. 1995. Oriented Perforation to Prevent Casing Collapse for Highly Inclined Wells. SPE Drilling and Completion 10(3): 139-145. SPE-28556-PA.

Nikolinakou, M.A., Luo, G., Hudec, M.R., and Flemings, P.B., 2012. Geomechanical modeling of stresses adjacent to salt bodies: Part 2 – Poroelastoplasticity and coupled overpressures, *AAPG Bulletin*, v.96, no. 1, p. 65-85.

Perez, M.A., Clyde, R., D'Ambrosio, P., Israel, R., Leavitt, T., Nutt, L., Johnson, C., 2005. Meeting the Subsalt Challenge. *Oilfield Review* 17, no.1 (Spring 2005): 4-17.

Rae, D., 1963. The measurement of coefficient of friction of some rocks during continuous rubbing. *J. Sci. Instr*. 40, 438-40.

Reis, A.T., Gorini, C., Weibull, W., Perovano, R., Mepen, M., Ferreira, E., 2008. Radial Gravitational Gliding Indicated by Subsalt Relief and Salt-Related Structures: the Example of the Gulf of Lions, Western Mediterranean. *Brazilian Journal of Geophysics* (2008) 26(3): 347-365.

Senseny, P.E., Hansen, F.D., Russell, J.E., Carter, N.L., Handin, J.W., 1992. Mechanical Behavior of Rock Salt: Phenomenology and Micro-mechanisms. *International Journal of Rock Mechanics Science and Geomechanics*. 29 (4) pp. 363-378.

Shaker, S., and Smith, M., 2002. Pore Pressure Predictions in the Challenging Supra/Sub-Salt Exploration Plays in Deep Water, Gulf of Mexico. *AAPG Annual Meeting*, Houston, 2002.

Shaker, S., 2007. The Double Edge Sword: The Impact of the Interaction between Salt and Sediment on Sub-salt Exploration Risk in Deep Water. *CSEG RECORDER* October 2007.

Tingay, M., Bentham, P., De Freyter, A., and Kellner, A., 2011. Present-day stress-field rotations associated with evaporites in the offshore Nile Delta: *AAPG Bulletin*, v. 123, no.5/6, p. 1171-1180, doi: 10.1130/B30185.1

Tingay, M., Bentham, P., De Freyter, A., and Kellner, A., 2012. Evidence for non-Andersonian faulting above evaporites in the Nile Delta, In Healy, D., Butler, R.W.H., Shipton, Z.K., and Sibson, R.H. (eds) 2012. *Faulting, Fracturing and Igneous Intrusion in the Earth's Crust*. Geological Society, London, Special Publications, 367, p.155-170, doi: 10.1144/SP367.11.

Tingay, M., Tuitt,A., King, R., Hergert, T., Hillis, R., 2014. Modelling of sediment wedge movement along low-angle detachments using ABAQUS™. *Geological Society*, London, Special Publications, 367, 171–183.

Tronvoll, J., Eek, A., Larsen, I., and Sanfilippo, F., 2004. The effect of oriented perforations as a sand control method: A field case study from the Varg Field, North Sea. In SPE International Symposium and Exhibition on Formation Damage Control. Society of Petroleum Engineers.

Turcotte, L., Schubert, G., 2001. Geodynamics -2nd ed. Rev ed of: *Geodynamics applications of continuum physics to geological problems*, 1982. Cambridge University Press, New York, USA.

Venkitaraman, A., Behrmann, L.A., Noordermeer, A.H., 2000. Perforating Requirements for Sand Prevention. SPE 58788.

Warren, J, 1999. *Evaporites: their evolution and economics*. Oxford: Blackwell Science.

Yielding, G., Freeman, B., Needham, D.T., 1997. Quantitative Fault Seal Prediction. *AAPG Bulletin*, v.81 no.6 p.897-917.

Yassir, N.A., and Zerwer, A., 1997, Stress regimes in the Gulf Coast, offshore Louisiana: Data from well-bore breakout analysis: *American Association of Petroleum Geologists Bulletin*, v. 81, p. 293–307.

Zienkiewicz, O.C., Taylor, R.L., Zhu, J.Z., 2005. *The Finite-Element Method, Its Basis and Fundamentals*, 6th ed, first edition 1991. Elsevier, Radarweg, Netherlands.

8. VITA

Weicheng Zhang was born in Kaifeng, China and grew up in Zhuozhou, China. He earned his Bachelor of Science degree in Petroleum Engineering from China University of Petroleum (Beijing) in 2013.

After graduation, in August 2013, he attended Missouri University of Science and Technology in Rolla, Missouri, for his graduate studies in Petroleum Engineering. He served as the graduate teaching assistant for the Well Logging course during the Spring 2014 and 2015 semesters and for the Mechanical Earth Modeling course during the Fall 2014 and 2015 Semesters. In May 2016, he received his Master of Science degree in Petroleum Engineering from Missouri University of Science and Technology.